N73-16244

NASA CR-2182

A BOUNDARY LAYER APPROACH TO THE ANALYSIS OF ATMOSPHERIC MOTION OVER A SURFACE OBSTRUCTION

by Walter Frost, J. R. Maus, and W. R. Simpson

Prepared by
THE UNIVERSITY OF TENNESSEE SPACE INSTITUTE
Tullahoma, Tenn. 37388
for George C. Marshall Space Flight Center

1. REPORT NO. NASA CR-2182	2. GOVERNMENT ACCESSION NO.	3. RECIPIENT'S CATALOG NO.
4. TITLE AND SUBTITLE A Boundary Layer Approach to the Analysis of Atmospheric Motion Over a Surface Obstruction		5 REPORT DATE January 1973
		6. PERFORMING ORGANIZATION CODE M109
7. AUTHOR(S) Walter Frost, J. R. Maus and W. R. Simpson		8. PERFORMING ORGANIZATION REPORT #
9. PERFORMING ORGANIZATION NAME AND ADDRESS The University of Tennessee Space Institute Tullahoma, Tennessee 37388		10. WORK UNIT NO.
		11. CONTRACT OR GRANT NO. NAS8-27387
12. SPONSORING AGENCY NAME AND ADDRESS National Aeronautics and Space Administration Washington, D. C. 20546		13. TYPE OF REPORT & PERIOD COVERED Contract Report June 3, 1971–Sept. 2, 1972
		14. SPONSORING AGENCY CODE

15. SUPPLEMENTARY NOTES

16. ABSTRACT

A boundary layer approach for the solution of the flow field induced over a two-dimensional surface obstruction, such as a building or other man-made structure, is proposed. Adopting a specific geometry in the form of a semi-elliptical cylinder, the characteristics of atmospheric shear flow over a rough terrain are coupled with the well-known boundary layer equations.

Two approaches are presented to incorporate the pressure field and boundary conditions which exist within the large viscous region over the obstruction. The first considers a region in the immediate vicinity of the body in which the pressure distribution and outer boundary condition on the velocity are computed from potential theory for flow over the elliptical cylinder. The second approach considers a much larger region of influence, extending from the surface to the undisturbed flow at large heights above the obstruction. Methods which appear to provide an improved theoretical model of the flow over the ellipse, such as a technique for simulating the effect of the separation regions upstream and downstream of the body, are also presented.

17. KEY WORDS Boundary Layer, Reynold's Number, Surface Roughness, Wind Profile	18. DISTRIBUTION STATEMENT

19. SECURITY CLASSIF. (of this report) Unclassified	20. SECURITY CLASSIF. (of this page) Unclassified	21. NO. OF PAGES 153	22. PRICE $3.00

MSFC - Form 3292

TABLE OF CONTENTS

LIST OF FIGURES

NOMENCLATURE

a	Length of semi-major axis of the elliptical cylinder measured parallel to the ground
b	Height of the elliptical cylinder
f	Coriolis parameter
g	Gravitational acceleration constant
k	Elliptical aspect ratio, a/b
ℓ	Prandtl mixing length
L	Characteristic length used to nondimensionalize equations defined as the ellipse height
$\bar{p}$	Mean pressure term
$\bar{p}_{act}$	Mean atmospheric pressure
q	Pressure damping function
Re	Reynolds' number, $(U_\infty L)/\nu$
t	Time
u_*	Friction velocity, $\sqrt{\tau_0/\rho}$
U_∞	Characteristic velocity defined by Equation 3 at a height $z = b$
U_e	Potential velocity defined along an inviscid streamline
$\bar{u}$	Mean velocity in the x-direction
$\bar{v}$	Mean velocity in the y-direction
$\vec{V}$	Total velocity vector
$\bar{w}$	Mean velocity in the z-direction

x	Coordinate measured in the direction of mean flow along the inviscid streamlines
X	Coordinate measured in flow direction along the surface of the ground
Δx	Numerical step size in the x-direction
y	Coordinate normal to the x-direction, parallel to the ground
Y	Coordinate normal to the X-direction along the ground
Δy	Numerical step size in the y-direction
z	Coordinate in the vertical direction normal to the inviscid streamlines
Z	Coordinate in the vertical direction
Δz	Numerical step size in the z-direction
z_o	Surface roughness length
δ_*	Boundary layer displacement thickness, $\int_0^\infty \left(1 - \dfrac{\overline{u}}{U_e}\right) dz$
ϵ	Eddy viscosity
ζ	Stretched coordinate transformed from the vertical coordinate, z
$\Delta\zeta$	Numerical step size in the ζ direction
η	Elliptical coordinate
κ	Von Karman universal constant = 0.40
λ	Length of forward separation region
μ	Dynamic viscosity
ν	Kinematic viscosity
ξ	Elliptical coordinate
ρ	Fluid density

τ	Shear stress
τ_o	Shear stress at the surface
ϕ	Velocity potential function
Φ	Derivative of the stretching function
ψ	Stream function
Ω	Rotational angular velocity of the earth
ω	Fluid vorticity

Subscripts

∞	Condition in the undisturbed flow
ℓ	Laminar flow quantity
m,n	Numerical indices in the x and ζ directions, respectively
n.s.	Conditions calculated along nonseparating streamline
s	Slip condition at the surface
t	Turbulent flow quantity

Superscripts

T	Indicates trail value in iteration procedure
*	Dimensionless quantity
'	Turbulent fluctuation of mean flow quantities

CHAPTER 1

INTRODUCTION AND STATEMENT OF PROBLEM

The localized flow fields induced around buildings
and other manmade obstructions by the surface winds have
long been of interest in structural design, but more
recently, atmospheric motion influenced by such obstacles
has become important in the design of airports, launch pads
and other landing facilities for aircraft and spacecraft.
Of particular interest, in view of the rapidly increasing
needs in commercial air transportation, is the development
of helicopter and V/STOL service in large metropolitan areas.
Because of the possibility of operating these aircraft from
the tops of buildings, the problem of analyzing building-
induced flow fields attains a new importance.

Many difficulties are involved in operating low speed
aircraft near buildings such as severe crosswinds, induced
vortex fields, regions of separated flow, and other unsteady
flow phenomena which make takeoff and landing extremely
hazardous. There are two possible approaches to minimizing
the dangers of these problems: the first is related to
improvements in the design of the aircraft and operating
procedures during takeoff and landing; and the second
attacks the source of the flow disturbances by modifying
airport design in an effort to reduce operational problems

created by the wind (1).[1] However, each of these approaches requires a detailed knowledge of the flow field and turbulence imposed on buildings and other structures near the ground.

One method for satisfying this need for quantitative descriptions of localized flow fields surrounding aircraft landing sites, is to make extensive measurements around existing facilities, but the problems of locating sensors in the most advantageous locations to measure critical flow parameters and the vast amount of data required for such a description, make this method highly impractical. Furthermore, such detailed measurements around existing airports are of little value in the design of new structures without additional theoretical work to establish similarity relationships between these flow fields.

In considering elevated V/STOL ports, interest is primarily concerned with the flow around buildings; however, at present, investigations are limited to qualitative descriptions of the effects of isolated structures and groups of buildings on atmospheric motions. A number of these descriptions are given in References (1), (2), (3) and (4) discussing such difficulties as three-dimensional effects, separated and wake flows, induced vortices, the effects of shear and interaction of turbulence with steady

---

[1]Numbers in parentheses refer to similarly numbered references in the bibliography.

flow phenomena, and other complexities which further empha-
size the necessity for theoretical approaches to the prob-
lems of atmospheric motion over surface obstructions.

In view of the above considerations and the importance
of such flows to aerodynamic design, the need for an analyt-
ical method for predicting local atmospheric motions
influenced by buildings and other surrounding topographical
features is obvious.

In formulating a model to completely describe this
complicated flow situation, the complete equations of motion
for turbulent flow must be considered. However, practical
methods for carrying out a solution of such equations are
limited to numerical approaches which are at present in the
very early developmental stages (5), (6) and (7). Further-
more, the extremely high financial costs in computing time
and the restriction of these solutions to specific problems
limit the use of this method.

An alternative approach for approximating atmospheric
motions over surface obstructions is to extend the concepts
of boundary layer theory, which have been very successful in
describing aerodynamic flow over surfaces of small curvature
where viscous regions are thin. In meteorlogical work, the
boundary layer concept has been applied to wind flow over
changes in terrain roughness (8), (9) and (10) and wind
screens (11) and (12), by introducing the idea of the dis-
turbed boundary layer.

Consider a fully developed turbulent shear flow

approaching a discontinuity in surface condition such as a change in surface roughness, as shown in Figure 1. Because the disturbance is convected downstream and diffuses vertically, it is assumed that at great distances upstream and large heights downstream of this discontinuity, the flow is unaffected by the change in surface roughness. The Ekman layer may experience an adjustment in height through the scaling relationship $h \sim u_*/f$, where u_* is influenced by z_o, however, this is not expected to affect the flow appreciably in the region of interest. This assumption leads to a region of influence surrounding the downstream roughness, outside of which the flow is characteristic of approach conditions. Very near the ground, however, the boundary layer is governed by local surface conditions with the outer flow exerting an influence only through the boundary conditions between the two regions (13).

Although the disturbed boundary layer concept holds a great deal of promise, there is little evidence that this approach has been applied to flow over buildings and other surface obstructions. Therefore, the purpose of this study is to investigate the use of this boundary layer concept in approximating the localized flow field induced around a surface obstruction by the impinging wind. Although the method developed within this study can, in general, be applied to flow over any two-dimensional body, the solutions given will be limited to semi-elliptical cylinders.

4
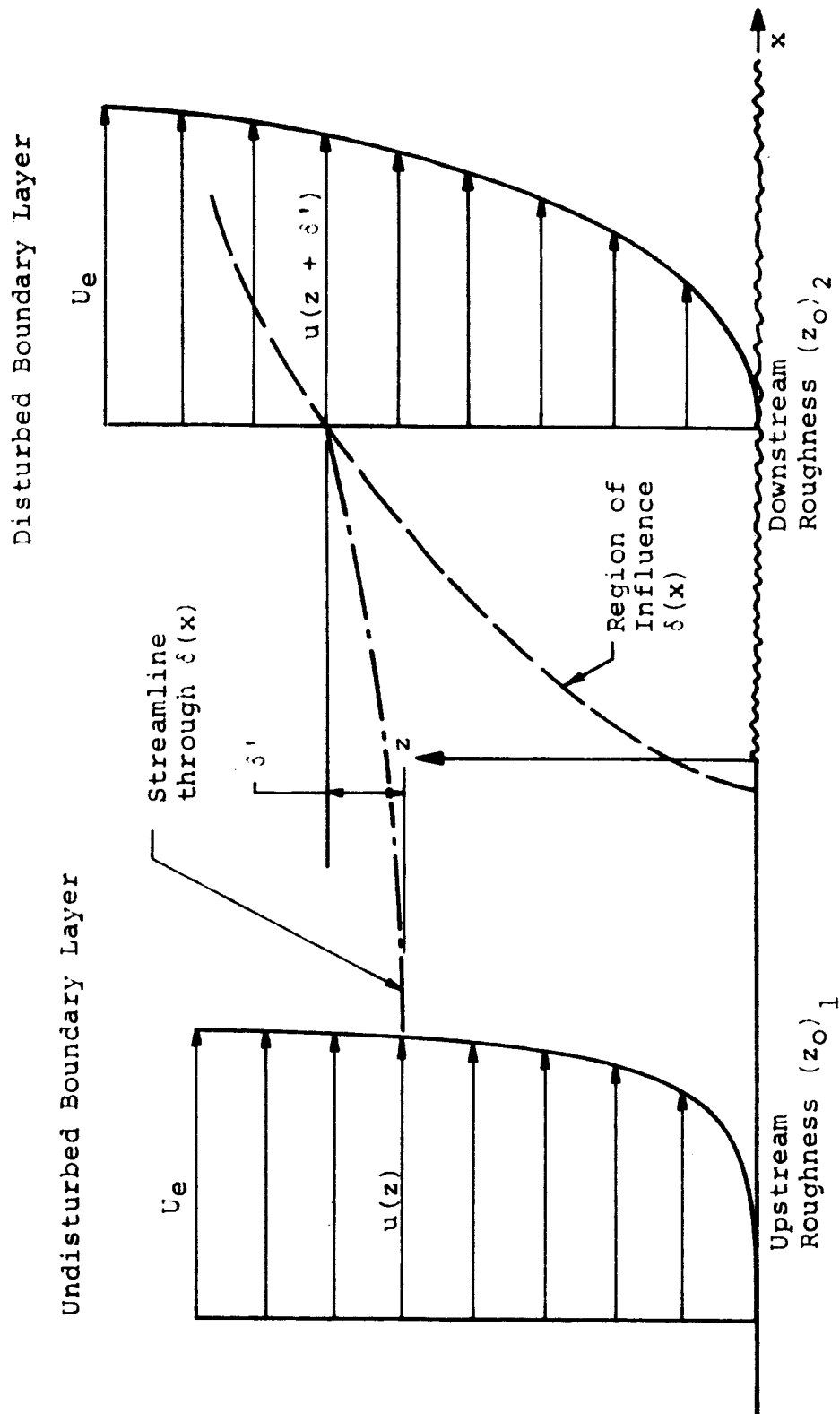
Figure 1. Concept of the disturbed boundary layer: $\delta(x)$ is the thickness of the internal boundary layer; δ' is the displacement of the outer flow field required by continuity.

5

CHAPTER II

ANALYSIS OF ATMOSPHERIC FLOW OVER SURFACE

OBSTRUCTIONS BY THE TURBULENT

BOUNDARY LAYER APPROACH

In applying the concepts of boundary layer theory to
atmospheric motions over surface obstructions, the following
two-dimensional model will be assumed. Consider a uniform
terrain of infinite extent on which a surface obstruction is
located in the form of a semi-elliptical cylinder as shown
in Figure 2. The elliptical contour is chosen primarily
because its geometry simulates low buildings or hills and
permits parametric variations of the aspect ratio. In
addition, the inviscid flow field around such an obstruction,
required for later analysis, is well established in potential
flow theory.

The Nature of the Approaching Wind

Assuming that the homogeneous terrain extends far
upstream from the elliptical obstruction, the viscous nature
of the atmospheric motion over the ground produces gradients
in the mean wind velocity. For conditions of neutral
stability experimental evidence (29) and (30) confirms that
the mean wind velocity in the region of the atmosphere
near the ground is described by a logarithmic expression
analogous to aerodynamic measurements of turbulent boundary
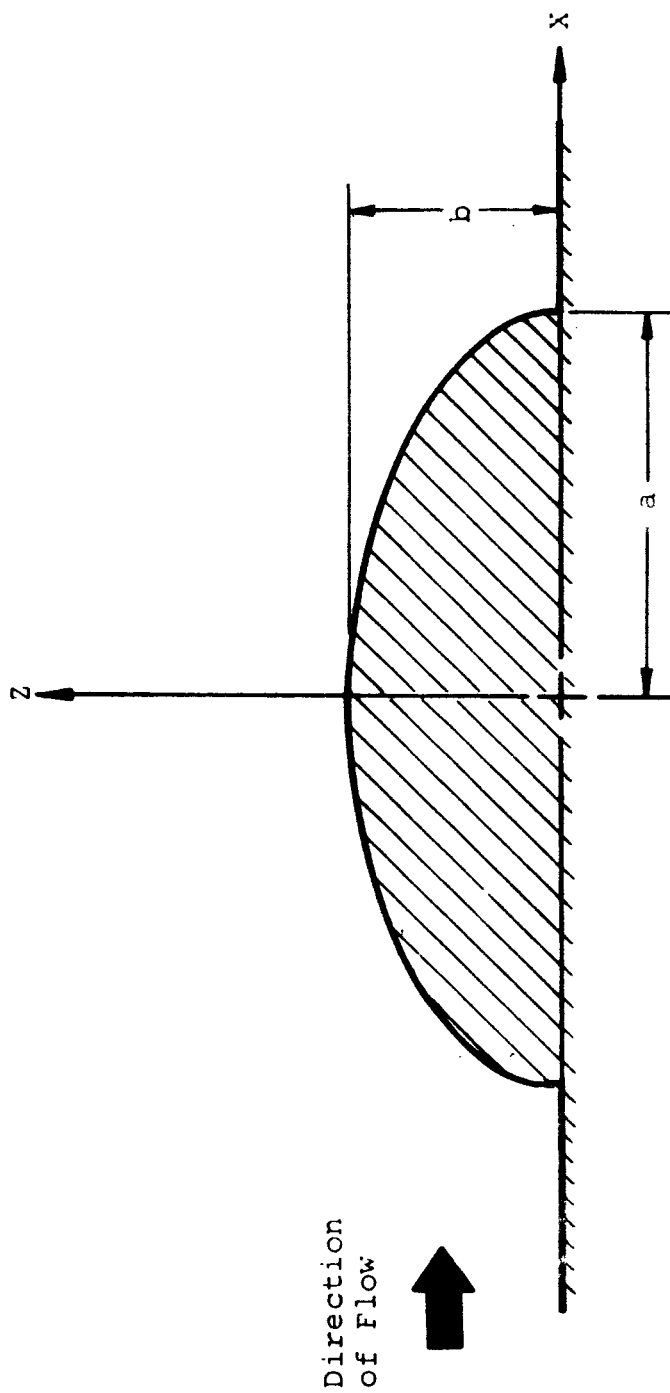
Figure 2. Basic geometry of the flow over a two-dimensional elliptical cylinder of major axis 2a and minor axis 2b.

layers. For smooth surfaces this logarithmic distribution
is given by the well known "law of the wall" (14),

$$\frac{u}{u_*} = \frac{1}{\kappa} \ln\left(\frac{zu_*}{\nu}\right) + C \qquad (1)$$

where κ is the universal von Karman constant, C is another
empirical constant, and u_* is the friction velocity defined
in terms of the surface shear stress as

$$u_* = \sqrt{\tau_0/\rho}$$

This universal velocity distribution was first
obtained by Prandtl as a consequence of his classical con-
cept of the mixing length for turbulent shear flows. The
validity of Equation 1 implies a region of constant shear
near the wall in which the mixing length is assumed propor-
tional to the normal distance from the surface approaching
zero at the smooth surface. (A discussion of the mixing
length theory will be given in a later section of this
investigation.)

In considering the more general case of a rough sur-
face, the logarithmic velocity distribution given above, must
be altered to incorporate roughness into the flow near the
surface. Roughness is a characteristic of most natural
terrains which is generally described in terms of a vertical
length scale, z_o. This length scale is related to the
height of the individual roughness elements, but is also
strongly dependent on the geometry and distribution of the

8

roughness over the surface. Typical values of z_O are given in Table I for different types of surface terrain.

The surface roughness causes an increase in the dissipation of momentum near the ground by larger viscous losses and more intense turbulent action. However, these effects become important only for surfaces on which the characteristic length, z_O, exceeds ν/u_*. In this case, the mixing length does not vanish near the wall but approaches the size of the roughness (15), and is given by the following expression:

$$\ell = \kappa(z + z_O) \tag{2}$$

Assuming that the surface roughness is uniformly distributed over the ground in a random manner, this relation for the mixing length leads to a logarithmic velocity of the following form:

$$\frac{\overline{u}}{u_*} = \frac{1}{\kappa} \ell n \left(\frac{z + z_O}{z_O} \right) \tag{3}$$

Therefore, far upstream from the elliptical obstruction, the flow field is described by the above equilibrium equation, valid for flow over a uniform, rough surface.

Governing Equations for Atmospheric Flow

The governing equations for steady, mean incompressible flow within the atmospheric boundary layer are well established in meteorlogical literature (16) and are stated in the following relationships:

9

TABLE I

ROUGHNESS LENGTHS FOR VARIOUS TYPES OF TERRAIN

Terrain Type	Surface Roughness Length (z_o) in Meters
Ice and snow	$10^{-7} - 7 \times 10^{-4}$
Smooth mud flats	10^{-5}
Sand flats	4×10^{-5}
Bare soils	5×10^{-4}
Thick grass ≤ 0.10 meters	0.02
Thin grass ≤ 0.50 meters	0.05
Thick grass ≤ 0.50 meters	0.09
Field crops, tall grass ≈ 1 meter	0.10 - 0.14
Forests, houses	1.00 - 2.00
Cities	1.00 - 3.00

Source: G. H. Fichtl, "Can Turbulent Drag Force Expansions Apart?" Paper presented at ASCE National Water Resource Conference Engineering Meeting, Atlanta, Georgia, January 24-28, 1972.

Continuity equation

$$\frac{\partial \bar{u}}{\partial x} + \frac{\partial \bar{v}}{\partial y} + \frac{\partial \bar{w}}{\partial z} = 0 \qquad (4)$$

Momentum equations

$$\bar{u} \frac{\partial \bar{u}}{\partial x} + \bar{v} \frac{\partial \bar{u}}{\partial y} + \bar{w} \frac{\partial \bar{u}}{\partial z} = - \frac{1}{\rho_o} \frac{\partial \bar{p}}{\partial x} + \frac{\partial}{\partial z} \bar{\tau}_{xz} + f\bar{v} \qquad (5)$$

$$\bar{u} \frac{\partial \bar{v}}{\partial x} + \bar{v} \frac{\partial \bar{v}}{\partial y} + \bar{w} \frac{\partial \bar{v}}{\partial z} = - \frac{1}{\rho_o} \frac{\partial \bar{p}}{\partial y} + \frac{\partial}{\partial z} \bar{\tau}_{yz} - f\bar{u} \qquad (6)$$

$$\bar{u} \frac{\partial \bar{w}}{\partial x} + \bar{v} \frac{\partial \bar{w}}{\partial y} + \bar{w} \frac{\partial \bar{w}}{\partial z} = - \frac{1}{\rho_o} \frac{\partial \bar{p}}{\partial z} + \frac{\partial}{\partial z} \bar{\tau}_{zz} + g\left(\frac{\bar{T} - T_o}{T_o}\right) \qquad (7)$$

where f is the Coriolis parameter, $\bar{\tau}$ is a shear stress, ρ_o and T_o denote the density and temperature consistent with an adiabatic atmosphere. The stresses due to eddies lying in the horizontal plane (i.e., τ_{xy}, τ_{yx}) have been neglected in comparison with the stresses arising from eddies lying in the vertical plane (i.e., τ_{xz} and τ_{yz}). The bar over the dependent variables indicates an ensemble average. In considering flow in the lower regions of the atmosphere certain assumptions and simplifications can be made in these equations and will now be discussed in detail.

Coriolis Effects in Atmospheric Shear Flows

The terms in Equations 5 and 6 given by $f\bar{u}$ and $f\bar{v}$ represent the apparent forces produced by the Coriolis effect on atmospheric motions. Below 30-50 m the shear viscous forces predominate and the Coriolis forces are generally neglected. This is discussed by Tverskoi (15)

11

who argues that below a few tens of meters the integral term
in

$$\tau(z) - \tau(z = 0) = f \int_{o}^{3} (u - u_g)dz$$

obtained by integrating the equations of the geostrophic
wind, is less than 10 per cent of the shear. For atmo-
spheric flow which occurs over much larger distances, the
effects of the rotation of the earth must be considered
however. The coordinate system on the earth is constantly
accelerated in an inertial frame (fixed reference frame
relative to distance stars), hence, motions which are
actually in straight lines in the fixed coordinate system
appear from the ground to travel in a curved path. The
fictitious Coriolis force in the relative frame of reference
accounts for this apparent deflection. In magnitude the
Coriolis force is a function of the earth's angular velocity,
Ω, and the geographical latitude, ϕ, and is proportional to
the velocity of the motion considered. It deflects the
velocity in a horizontal plane to the right in the Northern
Hemisphere and in the opposite direction in the Southern
Hemisphere acting perpendicular to the velocity vector, as
shown by the following relation:

$$F_c \simeq [2\Omega \sin \phi] \, \vec{V} \times \vec{k} = f(\vec{V} \times \vec{k})$$

where $\vec{k}$ is the unit vector in the vertical direction and f
is the Coriolis parameter.

With the magnitude of the Coriolis force determined

12

primarily by the velocity of the wind, its relative impor-
tance in contributing to the momentum of the flow can be
examined by considering the other dominant forces which act
upon the atmosphere. Outside of the viscous region of the
atmosphere, which generally extends to a height of about one
kilometer, the motion of the wind is to a sufficient degree
of approximation determined by a balance of the Coriolis
force and the pressure gradient. However, as the effects of
friction become significant within the boundary layer, the
mean wind speed decreases causing the effects of the Coriolis
force to also decrease. The balance of forces which deter-
mines the momentum of the flow within the boundary layer
includes the pressure field opposed by a combination of the
viscous and Coriolis forces. Very near the surface, where
the velocity approaches zero, the Coriolis force becomes
negligible, and the atmospheric motion is determined by a
balance of the pressure gradient and the viscous forces. As
a result of this change in the relative magnitude of the
Coriolis and shear forces, two distinct regions can be
identified within the atmospheric boundary layer: an inner
layer extending from the ground to a height of about 50
meters, in which the surface exerts the predominate influence
on the flow; and an outer region whose structure is primarily
determined by the Coriolis, pressure and shear forces.

Therefore, in view of the physical situation which
exists in the lower region of the atmospheric boundary layer,
the Coriolis term in the governing equations for flow over a

surface obstruction can be neglected, permitting a simpli-
fication of the equations to the following two-dimensional
form:

$$\frac{\partial \overline{u}}{\partial x} + \frac{\partial \overline{w}}{\partial z} = 0 \tag{8}$$

$$\overline{u} \frac{\partial \overline{u}}{\partial x} + \overline{w} \frac{\partial \overline{u}}{\partial z} = - \frac{1}{\rho_o} \frac{d\overline{p}}{dx} + \frac{\partial \overline{\tau}_{xz}}{\partial z} \tag{9}$$

$$\overline{u} \frac{\partial \overline{w}}{\partial x} + \overline{w} \frac{\partial \overline{w}}{\partial z} = - \frac{1}{\rho_o} \frac{\partial \overline{p}}{\partial z} + \frac{\partial \overline{\tau}_{zz}}{\partial z} \tag{10}$$

Approximation of the Reynolds' Stress by Turbulent Viscosity

The turbulent boundary layer equations given by Equa-
tions 8, 9 and 10 are obtained from the Navier-Stokes equa-
tions by a method first proposed by Reynolds, in which he
considered the instantaneous turbulent motion as a sum of a
mean flow component and a randomly fluctuating component,
given by

$$u(t) = \overline{u} + u'(t), \text{ etc.}$$

Introducing the Reynolds' assumption into the Navier-Stokes
equations and statistically averaging the instantaneous
motion over the ensemble of realization,[*] the equations for
general turbulent motion are obtained in which certain com-
binations of the fluctuating component are contained as
shown in the following relationships:

$$\frac{\partial \overline{u}}{\partial x} + \frac{\partial \overline{w}}{\partial z} = 0$$

---

[*]In practice the ergodic hypothesis is used and
ensemble averages are estimated with time averages.

14

$$\rho_0 \left(\overline{u} \, \frac{\partial \overline{u}}{\partial x} + \overline{w} \, \frac{\partial \overline{u}}{\partial z} \right) = - \frac{\partial \overline{p}}{\partial x} + \mu \, \frac{\partial^2 \overline{u}}{\partial z^2} + \mu \, \frac{\partial^2 \overline{w}}{\partial z \, \partial x}$$

$$- \rho_0 \left(\frac{\partial \overline{u'^2}}{\partial x} + \frac{\partial \overline{u'w'}}{\partial z} \right)$$

$$\rho_0 \left(\overline{u} \, \frac{\partial \overline{w}}{\partial x} + \overline{w} \frac{\partial \overline{w}}{\partial z} \right) = - \frac{\partial \overline{p}}{\partial z} + 2u \frac{\partial^2 \overline{w}}{\partial z^2}$$

$$- \rho_0 \left(\frac{\partial \overline{u'w'}}{\partial x} + \frac{\partial \overline{w'^2}}{\partial z} \right) + g \left(\frac{\overline{T} - T_0}{T_0} \right)$$

These equations are known as the Reynolds' equations for
turbulent flow in which the last group of terms on the right
side can be interpreted as additional components of the
stress tensor, called the Reynolds' stresses. Simplifying
these equations, based on an order of magnitude analysis,
results in the boundary layer equations given by Equations
8, 9 and 10 in which the Reynolds' stresses are reduced to
one term, $\rho \overline{u'w'}$, which is associated with an increase in the
shear of the fluid.

However, in order to close this set of boundary layer
equations, it is necessary to relate this additional stress
to the mean flow. This is generally done by considering an
analogy between the viscous shear which exists on a molecular
scale and the turbulent shear resulting from the momentum
transfer of macroscopic fluid particles. Accordingly, the
Reynolds' stress is said to be the result of an eddy vis-
cosity, ϵ, which is related to the mean flow by an expres-
sion analogous to the Stokes hypothesis for laminar shear

15

stress,

$$\tau_{\ell} = \rho \nu \, \frac{d\bar{u}}{dz}$$

$$\tau_t = \rho \overline{u'w'} = \rho \varepsilon \, \frac{d\bar{u}}{dz}$$

This approach in relating the turbulent fluctuations to the mean flow through the concept of the eddy viscosity has been used extensively in describing many turbulent flows; however, it is limited in usefulness by dependence on empirical correlations of specific flow situations.

Empirical Models of Eddy Viscosity

The concept of the mixing length. The development of expressions for the eddy viscosity relating it to parameters of the flow, is generally based upon Prandtl's concept of the transport processes involved in turbulence by relating the turbulent fluctuations in velocity to the mean flow through the idea of a mixing length.

Prandtl visualized turbulent flow as a random motion of macroscopic "lumps" of fluid which continually form and move through the fluid certain distances before being dispersed into the surrounding fluid. The distance over which these fluid "lumps" retain their original properties before coming into equilibrium with their surroundings is termed the mixing length, ℓ. A transfer of momentum, for example, can occur during this exchange process, resulting in a variation of the mean velocity at a particular location.

Consider two adjacent layers of fluid moving at different velocities, as shown in Figure 3, in which the mean flow is in the x-direction. The mean velocity is specified as $\bar{u}$ at a distance z from a surface and can be approximated at the adjacent layer by the positive velocity gradient as $\bar{u} + \ell \cdot (d\bar{u})/(dz)$. Consider the motion of a fluid particle from the position z to $z + \ell$ under the influence of a positive fluctuation of velocity, w', in the transverse direction. Since the momentum exchanged during this transfer of fluid results in a decrease in the velocity at $z + \ell$, Prandtl assumed that the momentum of the fluid particle remained constant so that the turbulent fluctuation in the horizonal velocity was given by the difference in velocity of the two layers as

$$u' = \left[(\bar{u} + \ell \frac{d\bar{u}}{dz}) - (\bar{u}) \right] = \ell \frac{d\bar{u}}{dz}$$

Further assuming that the transverse fluctuation, w', is the same order of magnitude as u', it is given by

$$w' = C \cdot u' = C\ell \frac{d\bar{u}}{dz}$$

Absorbing the constant C into the unknown mixing length, the Reynolds' stress is given by

$$\tau_t = \rho\overline{u'w'} = \rho\ell^2 \left(\frac{d\bar{u}}{dz}\right)^2 = \rho\ell^2 \left|\frac{d\bar{u}}{dz}\right| \frac{d\bar{u}}{dz} \tag{11}$$

with the eddy viscosity as

17
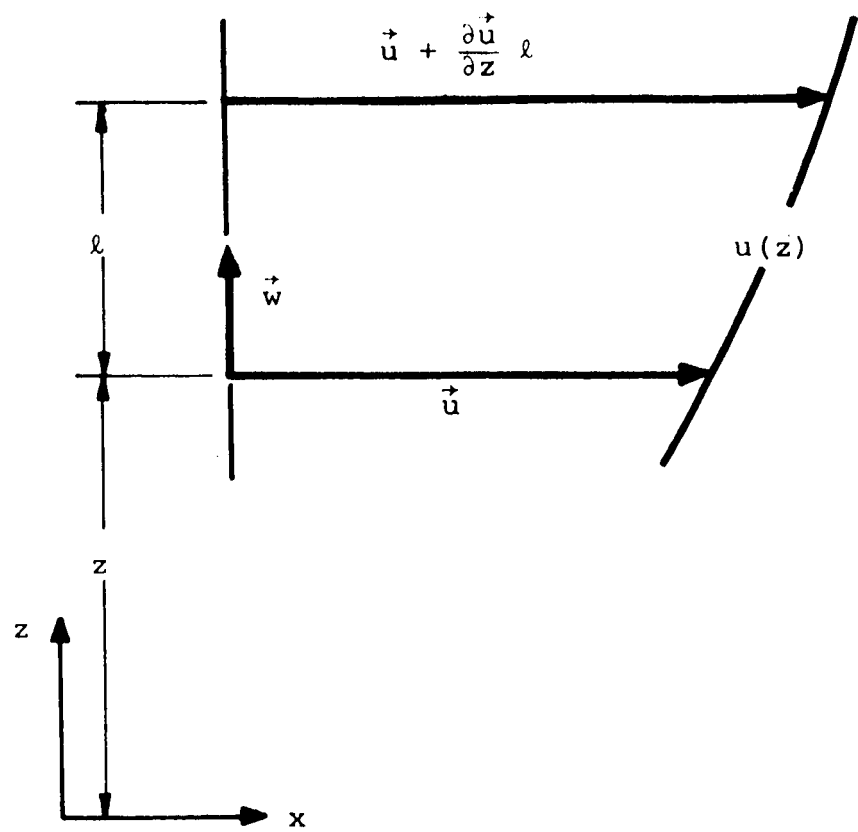
Figure 3. Turbulent mixing length concept.

$$\epsilon = \ell^2 \left| \frac{d\bar{u}}{dz} \right|$$

In the neighborhood of a wall, the mixing length is generally assumed to be linearly related to the normal distance from the surface

$$\ell = \kappa z$$

yielding the following expression for the eddy viscosity

$$\epsilon = \ell^2 \left| \frac{du}{dz} \right| = \kappa^2 z^2 \left| \frac{du}{dz} \right| \tag{12}$$

where κ is the universal von Karman constant generally assumed as 0.4. Applying this approximation of the mixing length to the turbulent shear stress near the wall, gives

$$\tau_t = \rho \kappa^2 z^2 \left| \frac{d\bar{u}}{dz} \right| \frac{d\bar{u}}{dz} \tag{13}$$

Assuming this shear stress is constant in a region next to the wall, Equation 13 can be integrated for the mean velocity profile

$$\bar{u} = \frac{u_*}{\kappa} \ell n \, z + C \tag{14}$$

The above logarithmic expression, as previously mentioned, is valid for turbulent flow over smooth surfaces, in which the mixing length approaches zero at the wall. However, for very rough surfaces the mixing length does not decay to zero near the ground, but approaches a size on the

order of the roughness length, z_o, and is given by the following relation

$$\ell = \kappa (z + z_o)$$

Therefore, the eddy viscosity over rough surfaces becomes

$$\epsilon = \kappa^2 (z + z_o)^2 \left| \frac{d\bar{u}}{dz} \right| \qquad (15)$$

leading to a logarithmic velocity distribution of the following form, previously introduced in Equation 3:

$$\bar{u} = \frac{u_*}{\kappa} \ell n \frac{z + z_o}{z_o}$$

Since rough surfaces are characteristic of most natural terrain the eddy viscosity model used in the calculations carried out in this study is given by Equation 15.

However, in verifying the numerical solution for turbulent boundary layer calculations, it is necessary to consider aerodynamic data of which a majority is obtained for flow over smooth surfaces requiring more sophisticated models of the eddy viscosity. Therefore, returning to Equation 14, it is evident that very near the wall the predicted logarithmic velocity is not valid because it does not approach zero at the surface. This is a result of the fact that the dampening effect of the wall is not taken into account. In actuality there exists a very thin layer next to the surface in which turbulence is no longer a factor

20

and the shear stress is predominately determined by molecular viscosity. In this region, known as the laminar sublayer, the eddy viscosity can be assumed zero. The thickness of the sublayer is generally obtained from empirical relations (14) as approximately

$$z_{s\ell} = 5 \cdot \frac{\nu}{u_*} \tag{16}$$

Van Driest eddy viscosity model. The condition that the eddy viscosity abruptly becomes zero at a height above the surface given by Equation 16 is an oversimplification of the physical situation. To overcome the arbitrary nature of this assumption, Van Driest (17) proposed that the turbulent viscosity approach zero exponentially near the surface, by modifying the Prandtl mixing length as follows:

$$\ell = \kappa z [1 - \exp(-z/A)]$$

where

$$A = \frac{26\nu}{\sqrt{\tau_o/\rho}}$$

The Van Driest mixing length, valid for flow over a flat plate, was extended by Cebeci and Smith (18) to include the effects of a pressure gradient on the eddy viscosity. From the momentum equation, they approximate the shear stress close to the wall by

$$\tau = \tau_o + \left(\frac{dp}{dx}\right) z$$

21

Defining A as $(26\nu)/(\sqrt{\tau/\rho})$, the mixing length can be expressed as

$$\ell = \kappa z \left\{ 1 - \exp\left(\frac{z}{26\nu}\sqrt{\frac{\tau_0}{\rho} + \frac{dp}{dx}\frac{z}{\rho}} \right) \right\}$$

and the modified Van Driest model for eddy viscosity becomes

$$\varepsilon' = \kappa^2 z^2 \left\{ 1 - \exp\left(- \frac{z}{26\nu}\left(\frac{\tau_0}{\rho} + \frac{dp}{dx}\frac{z}{\rho}\right)^{1/2} \right) \right\}^2 \cdot \left| \frac{du}{dz} \right| \qquad (17)$$

Although the above expression for the eddy viscosity is physically more realistic near the wall, in the outer regions of the boundary layer the surface no longer exerts the predominant influence on the flow. It is well documented by experimental evidence (14) and (18) that at certain distances from the boundary, the velocity profile deviates from the logarithmic form given by the mixing length theory. This is a result primarily of a decrease in the influence of the wall on the characteristics of the turbulence, causing the outer region of the boundary layer to approach a free turbulent flow, in which the eddy viscosity becomes constant. Therefore, Clauser (19) assumed that in the outer region of the viscous flow the eddy viscosity is related to the overall parameters of the boundary layer by

$$\varepsilon_0 = \kappa_0 U_e \delta^* \qquad (18)$$

where δ^* is the displacement thickness.

However, due to the highly fluctuating nature of the region separating the fully turbulent boundary layer from the relatively turbulent-free external flow, the constant viscosity given by Equation 18 should be modified by a damping factor experimentally determined from the intermittency factor of Klebanoff [20] as

$$\gamma = \left[1 + 5.5 \left(\frac{y}{\delta} \right)^6 \right]^{-1}$$

Separation of the inner and outer regions of the boundary layer is established by continuity of the eddy viscosity so that

$$\epsilon = \begin{cases} \epsilon_i & \text{if } \epsilon_i < \epsilon_o \\ \epsilon_o & \text{if } \epsilon_i \geq \epsilon_o \end{cases}$$

There are numerous other empirical models for eddy viscosity, but those considered in developing the turbulent boundary layer solution presented in this study are as follows:

1. Prandtl mixing length model.
2. Van Driest mixing length model.
3. Van Driest model with the outer layer of Clauser.

Conservation of eddy viscosity. A more recent theory for determining the eddy viscosity from mean flow parameters was advanced by Nee and Kovasznay [21] in which they consider the viscosity as a quantity which is conserved during

23

the turbulent exchange processes. This method has been out-
lined in Appendix C together with a numerical technique for
incorporating it into the present boundary layer program.
Preliminary investigation of this method has shown some
promise; however, further work is necessary to determine its
usefulness over the simpler mixing length models.

Consideration of the Pressure Force in the Boundary Layer Equations

Incorporating the assumptions introduced in the pre-
vious sections concerning the Coriolis effect and the eddy
viscosity, and applying the classical boundary layer order
of magnitude analysis the equations become

$$\frac{\partial \overline{u}}{\partial x} + \frac{\partial \overline{w}}{\partial z} = 0 \tag{19}$$

$$\overline{u} \frac{\partial \overline{u}}{\partial x} + \overline{w} \frac{\partial \overline{u}}{\partial z} = - \frac{1}{\rho} \frac{\partial \overline{p}}{\partial x} + \frac{\partial}{\partial z}\left[(\nu + \varepsilon) \frac{\partial \overline{u}}{\partial z} \right] \tag{20}$$

$$\frac{\partial \overline{p}}{\partial z} = 0 \tag{21}$$

These equations have been very successful in
describing flow fields over aerodynamic surfaces, for which
the viscous regions are very thin relative to the character-
istic dimensions of the body. In fact, the derivation of
the boundary layer equations from the Navier-Stokes rela-
tions from an order of magnitude analysis requires the
viscous region to be thin. However, despite the condition
of a thin viscous region, boundary layer analyses have been
applied to cases in which the boundary layer thickness was

24

on the order of the dimensions of the body but yielded good agreement with experiment, as shown in Reference (22). This tends to indicate that the application of boundary layer theory is not limited to confined regions of a flow field near a body.

One of the most significant results of the thin boundary layer assumption, as shown by Equation 21, is that the pressure field within the viscous region becomes independent of the coordinate normal to the flow. This result is important in establishing a solution of the thin boundary layer equations, because the pressure imposed on the flow can be obtained from the potential pressure distribution along the surface of the body and is a known quantity in the boundary layer equations.

However, in considering atmospheric flow over a surface obstruction, the thickness of the boundary layer is generally many times greater than the height of the obstacle. Thus, the pressure disturbance produced by the body is contained within the viscous flow and no well defined outer inviscid flow field exists as in aerodynamic problems. This difficulty can be resolved, however, by considering the concept of the disturbed boundary layer introduced in Chapter I. Assuming that the region of influence which surrounds the body is contained within the atmospheric boundary layer, the equations which describe the motion over the obstruction are no longer dependent on the flow field which exists outside the viscous region, but become a function of the boundary

conditions and pressure field which are given within the shear flow.

Therefore, to adapt the boundary layer equations to very thick viscous regions containing variations in pressure normal to the flow, the streamwise pressure gradient of Equation 20 can be interpreted as some average pressure force which is representative of the distribution of this gradient through the boundary layer. In order to determine how the horizontal pressure field over the obstruction varies in the vertical direction and to examine the effects of this term on the equations, the potential pressure distribution along the streamlines over the elliptical cylinder will now be considered.

Applying the potential flow theory outlined in Appendix A, the pressure and inviscid streamlines can be calculated as given in Figure 4 for the 2/1 aspect ratio ellipse. First, consider the pressure variation along the surface or zero streamline. Approaching from upstream, the pressure increases from the free stream value to a maximum along the leading edge and then rapidly decreases below ambient conditions to a minimum at the top of the ellipse. Since the potential flow is symmetric about the minor axis of the ellipse, the identical pressure distribution exists on the downstream side of the cylinder. However, the gradient of the pressure is not symmetric about this axis but is an odd function of the streamwise coordinate, x. This will become important in later discussions in

26
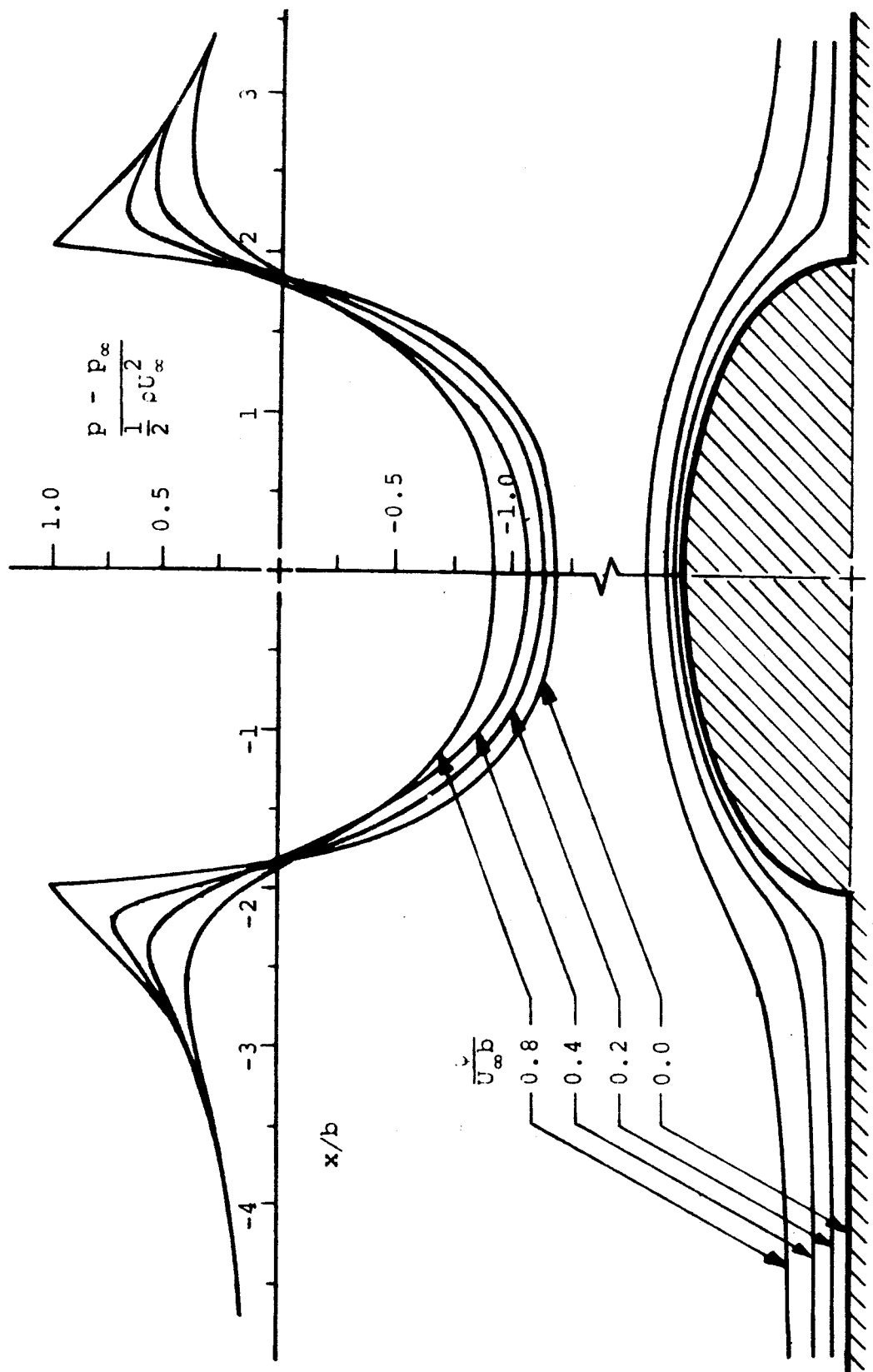
Figure 4. Potential pressure distribution over the elliptical cylinder.

considering the magnitude of the adverse pressure fields up-
stream of the ellipse approaching the forward stagnation
point and on the downstream face of the cylinder from the
top of the ellipse to the trailing edge. It is obvious from
Figure 4 that the latter pressure gradient is much more
severe and will have a significant effect on the viscous
flow.

Applying the potential pressure along the surface to
the boundary layer developed far upstream on the horizontal
terrain, a qualitative picture of the viscous flow field
over the body can be obtained. Approaching the obstruction
from upstream, as illustrated in Figure 5, the large increase
in pressure causes deceleration of the flow and thickening
of the internal boundary layer. As the pressure gradient
becomes increasingly more severe, the momentum of the fluid
becomes very small until the boundary layer is no longer able
to remain attached to the surface, (point A). Further down-
stream, the flow is accelerated by the decrease in pressure
over the front face of the ellipse causing the boundary
layer to reattach to the body at point B. From this point
the flow continues to accelerate to the top of the cylinder
where the adverse pressure field on the rear side again
forces the boundary layer to separate at point C. Much
further downstream the pressure field begins to recover from
the severe gradients discussed above and returns to ambient
conditions causing the flow to reattach once more (point D)
and readjust to the conditions along the horizontal surface.
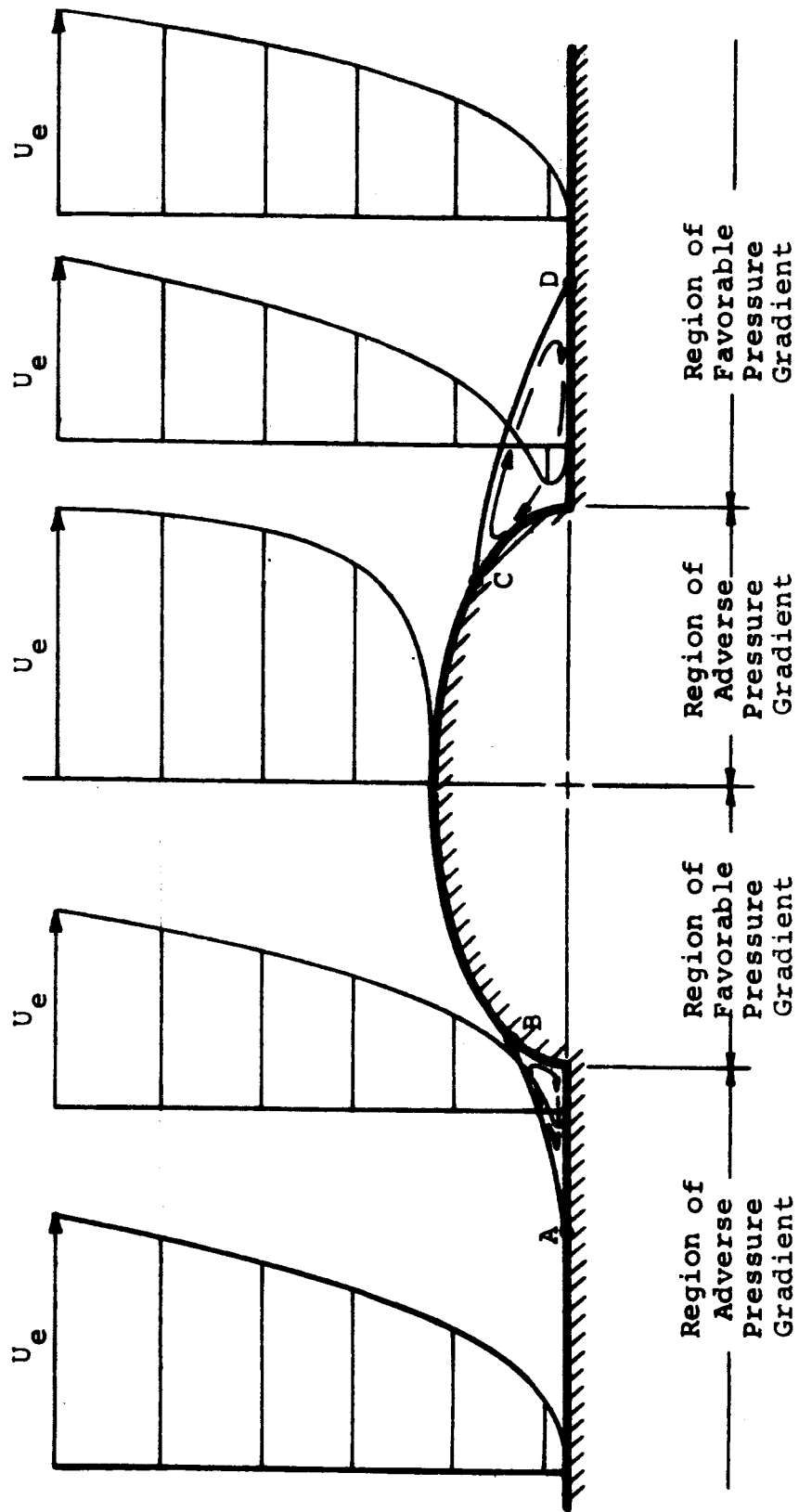
Figure 5. Qualitative description of the flow field over the elliptical cylinder.

The areas of the flow field enclosed by streamlines AB up-
stream of the ellipse and CD on the downstream side are

separation regions in which the flow is recirculated,

tending to become stagnant with the velocity near the sur-

face in the opposite direction to that in the outer flow as

illustrated by the profiles in Figure 5. This separated

flow region is an extremely complicated motion which cannot

be predicted by a boundary layer analysis. Therefore,

additional assumptions must be made about the adverse pres-

sure field which produces this separated flow to enable the

boundary layer solutions to be computed over this region to

the top of the ellipse.

Comparing the variation of the streamwise pressure

distribution along different streamlines above the surface,

as shown in Figure 4, page 27, it can be observed that as

the distance from the body increases, the severity of the

pressure gradient decays until outside a certain streamline,

the adverse pressure upstream of the body no longer causes

separation of the flow. Since the pressure field near the

surface primarily determines the flow within the separation

region, it is reasonable to assume that the pressure gradient

given along this nonseparating streamline is more character-

istic of the overall flow which actually negotiates the

obstruction. With this in mind, the boundary layer analysis

proposed in this study was carried out with the assumption

that the flow outside the separation region is governed by

an average pressure field given by :) at calculated along the

first nonseparating streamline over the elliptical body.

Improved Approximation of the Vertical Pressure Field

The assumption of an average pressure gradient which
is constant in the direction normal to the flow is expected
to be a good approximation of the conditions which exist in
a region near the body, as will be substantiated in later
discussions concerning the results of calculations carried
out over the elliptical cylinder using this mean pressure
distribution. However, if interest lies in flow fields much
further removed from the surface obstruction, a more physi-
cally realistic pressure field is suggested by the fact that
the pressure gradient approaches zero far from the body.
Therefore, for boundary layers which extend well above the
obstruction, an improved pressure field would be one which
decays in the vertical direction from the initial value
determined along the nonseparating streamline to zero as the
distance from the body approaches infinity. This type of
pressure variation will permit a matching of the flow within
the region of influence of the body to the outer undisturbed
logarithmic profile. Under this assumption, the form of the
pressure distribution introduced into the boundary layer
equations is given by

$$\frac{dp(x,z)}{dx} = \left(\frac{dp(x)}{dx}\right)_{ns} \cdot q(z)$$

where $[(dp)/(dx)]_{ns}$ is the pressure gradient given along the
nonseparating streamline, and $q(z)$ is the vertical decay

function, which will be discussed in more detail in a later section.

Boundary Conditions

The governing equations described in the preceding sections are complete only when the proper boundary conditions along the surface and matching conditions with the outer flow are specified.

Lower boundary conditions.

Along the lower boundary the no-slip condition will generally apply, and thus the mean velocities and turbulent fluctuations approach zero near the ground. However, the roughness associated with the surface also has an influence upon the flow in the vicinity of the lower boundary. One effect is to increase the turbulent motion, as noted previously, by assuming a larger mixing length at the surface. An additional effect of the rough surface is caused by the separation of the flow on a very small scale from the individual roughness elements which increases the dissipation of momentum due to larger form drag over the surface. Since neither of these effects are accounted for by the simple no-slip condition, it is assumed that the logarithmic velocity distribution given by Equation 3 applies in a very thin layer next to the surface in which the shear stress is assumed constant, as shown in Figure 6. With this boundary condition the influence of the surface roughness on the velocity can be incorporated into the solution of the boundary layer equations.
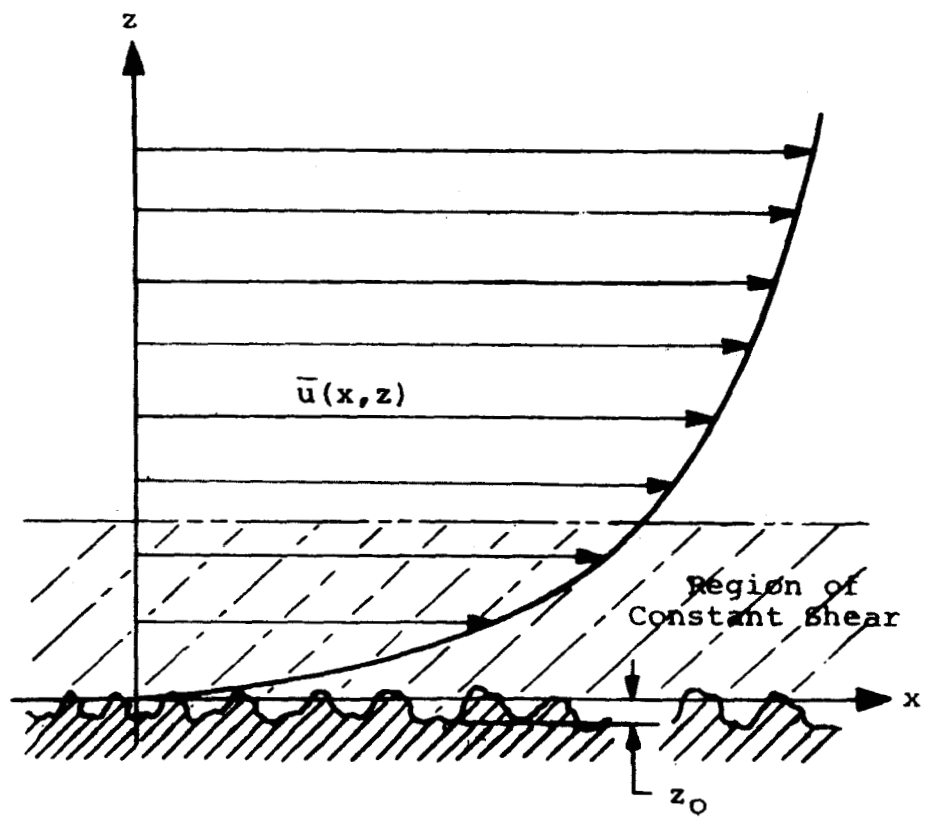
Figure 6. Flow over a rough surface.

Outer boundary conditions. The outer boundary condition usually imposed on classical boundary layers is the potential velocity along the surface streamline of the body. This assumption is based on the fact that the boundary layer is extremely thin and the surface curvature is not large.

For the problem at hand, however, the pressure distribution over the body is not assumed to be that corresponding to the potential flow along the surface streamline but that corresponding to the first streamline for which separation at the front of the ellipse does not occur. The outer boundary condition is therefore taken as the potential velocity, U_e, along this first non-separating streamline. Physically one defends this assumption by arguing that the flow which negotiates the body avoiding the separation region is driven by some average pressure characterized by $\left(U_e \frac{dU_e}{dx}\right)_{ns}$ and the velocity scale for the disturbed shear region or internal boundary layer is $U_{e_{ns}}$. Although it is known that far from the body the velocity must return to the logarithmic profile of the undisturbed flow it is expected that $U_{e_{ns}}$ may represent the peak in the velocity profile and the solution corresponding to this boundary condition might be valid very near to the wall. Later refined calculation shows this region extends to a height on the order of $z/b = 0.5$. A number of solutions were carried out utilizing this boundary condition and pressure distribution and are expected to be representative of the flow very near the body.

However, once again considering flow fields at larger heights, the outer boundary condition must be

34

reconsidered in light of the rapid decay of the pressure field which exists in the greater region of influence above the surface obstruction. Since the flow tends to return to the logarithmic form as the effects of the obstacle become negligible, a more realistic outer boundary condition matching the outer undisturbed flow with the boundary layer developed over the body would be given by the logarithmic velocity distribution. Therefore, in considering the flow field in a larger region above the elliptical cylinder, the outer boundary condition used in connection with the decaying pressure field is given by the logarithmic velocity characteristic of the undisturbed flow at an arbitrarily selected elevation.

The Effect of Separation Regions on the Boundary Layer

The separation regions which exist upstream and downstream of the elliptical cylinder, as shown in Figure 5, page 29, are due to the strong adverse pressure gradients near the surface which have been neglected in the initial solutions to be presented because the pressure field is approximated along the nonseparating streamline. For this reason the boundary layer equations can be integrated over the forward separation region without regarding the effects it produces on the flow. However, this method cannot be extended over the rear separation bubble because the adverse pressure gradient along the same streamline becomes much more severe on the downstream side of the body and prevents

the computational scheme from negotiating this region. As discussed previously in comparing the magnitude of the positive pressure gradients shown in Figure 4, page 27, the much larger pressure forces occurring downstream significantly affect the boundary layer flow, so that in order to apply the present integration technique over the rear separation region, the pressure field must be obtained from an inviscid streamline very far from the body. Since the pressure gradients downstream will be greatly reduced, the solutions are no longer believed to give a meaningful description of the disturbed flow field created by the surface obstruction. Therefore, the solutions given in this study for flow over the elliptical body are carried out only to the top of the cylinder.

To incorporate some of the influence of the separation regions on the pressure field near the surface and to obtain a more realistic boundary condition on the velocity over these regions, some preliminary solutions have been computed with the recirculating flow of the separation bubbles simulated by stationary, inviscid vortices calculated from potential flow theory (23). Although not dealing directly with the flow within these regions, this technique, outlined in Appendix B, gives an improved approximation of the pressure field imposed on the flow by the elliptical cylinder. A typical result of this calculation is given in Figure 7, showing the inviscid streamlines over a 2/1 aspect ratio ellipse with attached vortices together with the
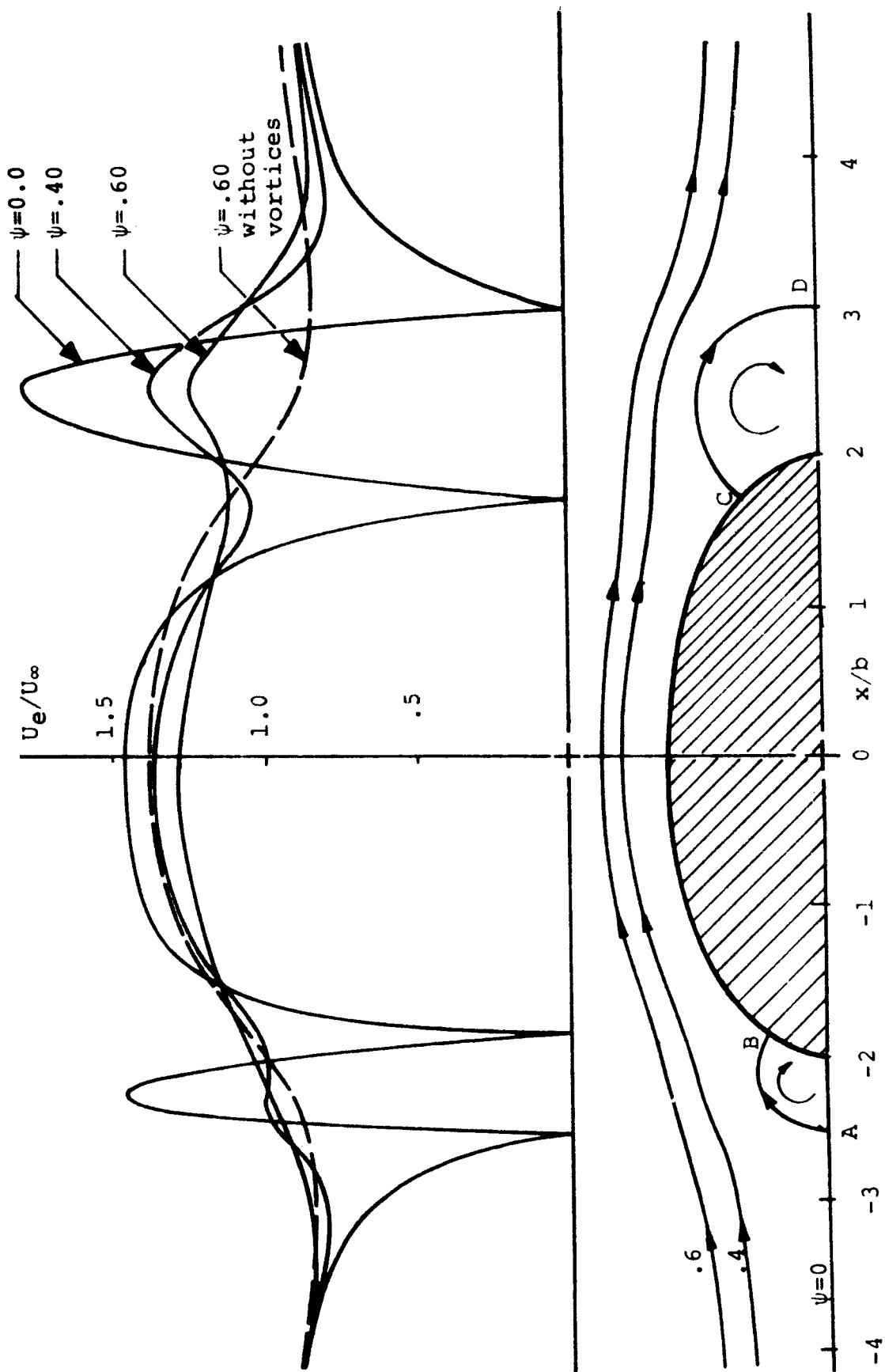
Figure 7. Potential velocity distribution over elliptical cylinders with fixed vortices.

37

potential velocity distribution along these streamlines. In addition, the potential velocity along the nonseparating streamline over the same body without vortices is also shown for comparison purposes.

Despite the improved approximation of the pressure field obtained with this model which includes the effects of the separation regions, the adverse pressure gradients associated with the flow approaching the stagnation points A and B are still sufficiently severe near the body to prevent the boundary layer calculation from negotiating these regions. Therefore, the applicable pressure distribution is again assumed to be given along an outer streamline over the vortices for which the pressure gradient does not produce a condition of separation in the boundary layer solution. Although this pressure field still does not simulate that given along the surface, it does include a part of the significant influence of the separation regions on the boundary layer which is neglected by the initial approximation of the pressure gradient over the elliptical cylinder.

In addition to the effect of the vortices on the pressure field, the potential velocity along the streamline dividing the separation region from the outer boundary layer can be incorporated into the flow field developed over this region as a lower boundary condition. Since the velocity which physically exists in the vicinity of the dividing streamline does not approach zero, the slip-velocity provided by this potential solution is a more realistic measure of

38

the lower boundary condition affecting the equations than

that previously introduced for the calculations made over

this region. However, the potential velocity calculated

over the vortices, as shown in Figure 7, page 37, approaches

free stream values at its maximum between the stagnation

points on the dividing streamline. Since this characteristic

of the potential solution is a result of the effect of the

vortex on an inviscid fluid, the viscous dissipation which

actually occurs in this region decreases the potential

velocity, and therefore, the lower boundary condition

assumed from this model will be a fraction of the inviscid

velocity, which has been chosen for the calculations made

with this method as 0.25.

Curvilinear Effects of the Streamline-Oriented Coordinate System

Since the pressure gradient imposed on the boundary

layer is given along the inviscid streamlines over the

elliptical cylinder, the coordinate system used must also be

oriented along these streamlines resulting in a curvilinear,

orthogonal system, as shown in Figure 8a. The curvature of

this coordinate system is small throughout the region sur-

rounding the ellipse, except in the vicinity of the upstream

and downstream stagnation points where the slope of the sur-

face is discontinuous. This is important in view of the

fact that the boundary layer concept is generally assumed to

be a first order approximation of viscous flow and neglects

(a) Physical Coordinates

(b) Assumed Numerical Coordinates
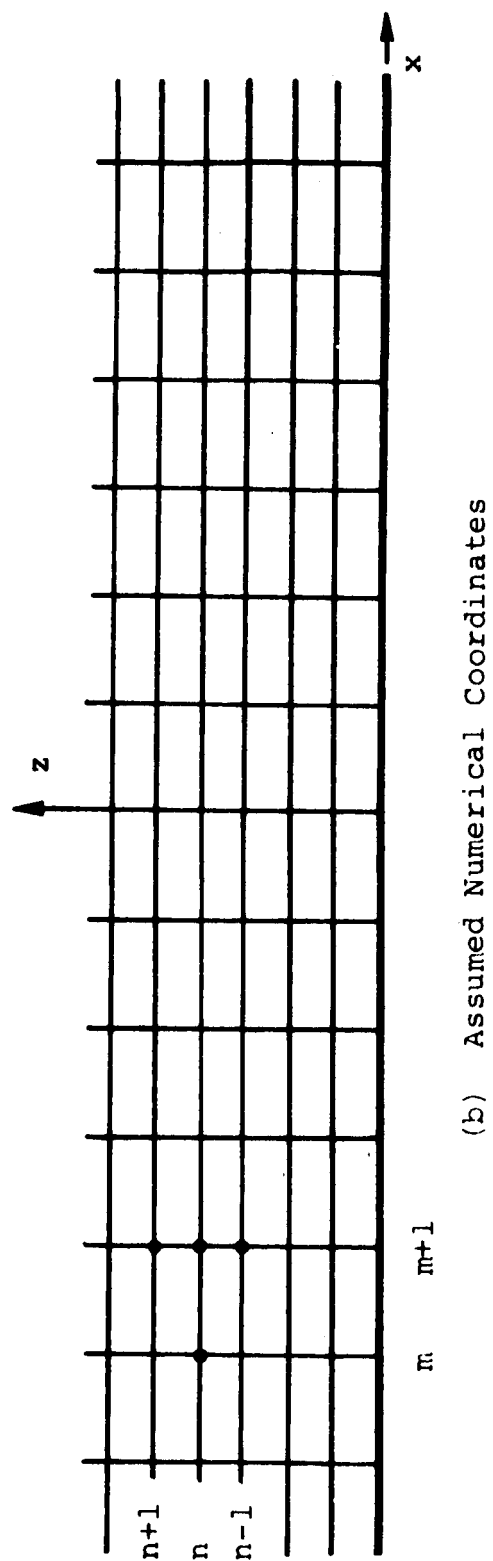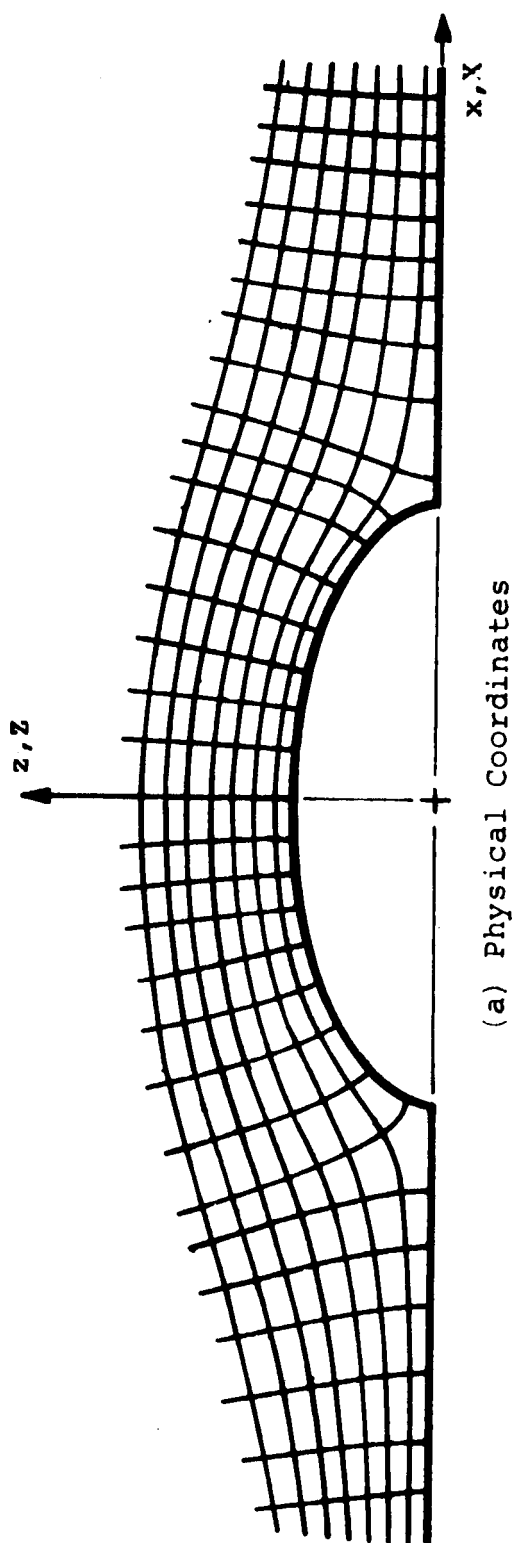
Figure 8. Coordinate system over the elliptical cylinder.

40

the higher order effects produced by body curvature. There-
fore, the accuracy of the present boundary layer analysis is
expected to deteriorate in the vicinity of the stagnation
regions but be relatively good upstream of these regions and
on top of the ellipse.

Moreover, since the flow field within these stagna-
tion regions has been neglected by the assumption, pre-
viously discussed in Chapter II, of a pressure distribution
imposed on the flow as given by that along the nonseparating
streamline, there is little value in modifying the boundary
layer equations with the additional complications of a
curvilinear coordinate system. Consequently, the calcula-
tions have been carried out in Cartesian coordinates (x,y)
as shown in Figure 8b. The x-direction is measured along
the inviscid streamline with the y-axis extending perpen-
dicularly to it at each x-point. The velocity profiles
calculated in this coordinate system are then assumed to
exist physically on the surface, which is a reasonable
assumption because the geometrical effects of the body on
the flow enter the equations only through the pressure
gradient. However, because of the assumptions made about
the pressure distribution and curvature effects over the
stagnation regions, the interpretation of the velocity pro-
files calculated in these areas of the flow field is diffi-
cult to apply physically. Consequently, the profiles
presented within this investigation are those in the regions
of flow upstream and on top of the ellipse where the

41

solutions are considered to be the most meaningful,
neglecting the profiles calculated over the separation
regions.

CHAPTER III

NUMERICAL SOLUTION OF THE TURBULENT

BOUNDARY LAYER EQUATIONS

The turbulent boundary layer equations together with the boundary and initial conditions and the assumption of an eddy viscosity model to relate the turbulent motion to the mean flow variables, form a closed set of nonlinear, parabolic, partial differential equations given by Equations 19 and 20. This set of equations must be solved by numerical methods which will now be introduced. Approximating the pressure gradient term by the inviscid pressure distribution along the nonseparating streamline, the Bernoulli equation can be used to relate this term to the potential velocity as follows:

$$- \frac{1}{\rho} \frac{d\bar{p}}{dx} = U_e \frac{dU_e}{dx} \tag{22}$$

Adopting some characteristic length, L, and velocity, U_∞, from the flow field over the surface obstruction, these equations can be nondimensionalized into the following form:

$$\frac{\partial \overline{u^*}}{\partial x^*} + \frac{\partial \overline{w^*}}{\partial z^*} = 0 \tag{23}$$

$$\overline{u^*} \frac{\partial \overline{u^*}}{\partial x^*} + \overline{w^*} \frac{\partial \overline{u^*}}{\partial z^*} = U_e^* \frac{dU_e^*}{dx^*} + \frac{1}{Re^*} \frac{\partial}{\partial z^*} \left[(1 + \epsilon^*) \frac{\partial \overline{u^*}}{\partial z^*} \right] \tag{24}$$

43

where the dimensionless quantities are indicated by stars as

$$\bar{u}^* = \frac{\bar{u}}{U_\infty} \qquad x^* = \frac{x}{L}$$

$$\bar{w}^* = \frac{\bar{w}}{U_\infty} \qquad z^* = \frac{z}{L}$$

$$U_e^* = \frac{U_e}{U_\infty} \qquad \epsilon^* = \frac{\epsilon}{\nu}$$

and Re denotes the dimensionless parameter defined as the Reynolds' number by

$$Re = \frac{U_\infty L}{\nu}$$

Dropping the dimensionless notation and expanding, the equations to be solved are given by

$$\frac{\partial \bar{u}}{\partial x} + \frac{\partial \bar{w}}{\partial z} = 0 \tag{25}$$

$$\bar{u} \frac{\partial \bar{u}}{\partial x} + \bar{w} \frac{\partial \bar{u}}{\partial z} = U_e \frac{dU_e}{dx} + \frac{1}{Re}\left(\frac{\partial^2 \bar{u}}{\partial z^2}(1 + \epsilon) + \frac{\partial \bar{u}}{\partial z} \frac{\partial \epsilon}{\partial z}\right) \tag{26}$$

A transformation of the vertical coordinate, z, which will compress the vertical length scale near the wall where the velocity gradients are the most severe, is now introduced into the governing equations in the form of a stretching function $\zeta = f(z)$. Applying this coordinate transformation to the vertical derivatives results in the following relations:

$$\frac{\partial}{\partial z} = f'(z)\frac{\partial}{\partial \zeta}$$

$$\frac{\partial^2}{\partial z^2} = [f'(z)]^2 \frac{\partial^2}{\partial \zeta^2} + f''(z)\frac{\partial}{\partial \zeta}$$

Defining the functions

$$\phi_1(\zeta) = f'(z) = f'[g(\zeta)]; \quad \phi_2(\zeta) = f''[g(\zeta)]$$

the boundary layer equations become

$$\frac{\partial \overline{u}}{\partial x} + \phi_1 \frac{\partial \overline{w}}{\partial \zeta} = 0 \tag{27}$$

$$\overline{u} \frac{\partial \overline{u}}{\partial x} + \overline{w} \, \phi_1 \frac{\partial \overline{u}}{\partial \zeta} = U_e \frac{dU_e}{dx} + \frac{1}{Re}\left[(1 + \epsilon)\left(\phi_1^2 \frac{\partial^2 \overline{u}}{\partial \zeta^2} + \phi_2 \frac{\partial \overline{u}}{\partial \zeta} \right) \right.$$
$$\left. + \phi_1^2\left(\frac{\partial \overline{u}}{\partial \zeta} \cdot \frac{\partial \epsilon}{\partial \zeta} \right) \right] \tag{28}$$

The stretching function, $\zeta(z)$, used in the calculations presented in this investigation, is given by the following quadratic relation:

$$z = \ell \zeta^2 + m\zeta + n$$

in which the constants ℓ, m and n were adjusted to most efficiently space the calculation points through the boundary layer.

The Implicit, Finite Difference Technique for Solution of the Boundary Layer Equations

Assuming that the flow field over the elliptical cylinder is represented by the Cartesian grid given in Figure 8b, page 40, the equations of motion can be solved by

45

approximating derivatives by finite differences expressed in terms of the nodal points of this grid. This numerical approximation results in a set of finite difference equations involving the unknown velocities at nodal points along an x-station, m + 1, in terms of known values at the preceding station m. Specifically, the equations are written in finite difference form at each point of the unknown m + 1 station using the following expressions for the x- and z-derivatives:

$$\left.\frac{\partial u}{\partial x}\right)_{m+1,n} = \frac{u_{m+1,n} - u_{m,n}}{\Delta x}$$

$$\left.\frac{\partial u}{\partial \zeta}\right)_{m+1,n} = \frac{u_{m+1,n+1} - u_{m+1,n-1}}{2\Delta \zeta}$$

$$\left.\frac{\partial^2 u}{\partial \zeta^2}\right)_{m+1,n} = \frac{u_{m+1,n+1} - 2u_{m+1,n} + u_{m+1,n-1}}{(\Delta \zeta)^2}$$

However, since the momentum equation of the boundary layer is nonlinear in the inertial terms, an iterative procedure must be introduced into the above numerical method. Initially, the values of the velocity at the known station m will be used to linearize the equations at m + 1. Numerically solving the system of equations at m + 1, this solution can then be used to linearize the momentum equation for a second iteration. Continuing this process by repeatedly linearizing the boundary layer equation with successive solutions for the velocity at m + 1 until convergence is achieved, results in the numerical solution of the flow

46

field at this x-station. Proceeding downstream to the next station, m + 2, this method can be repeated by using the converged solution at m + 1 to initially linearize the equations at m + 2 continuing the above iteration procedure until convergence of the solution at m + 2 is reached. In a similar manner this numerical procedure can be marched downstream over the entire flow field obtaining the turbulent boundary layer solution.

Returning to the details of the numerical solution, the iterative technique and the finite difference approximations can be introduced into Equation 28, resulting in the following algebraic expression of the boundary layer equations at a point (m + 1, n):

$$
u^T_{m+1,n} \cdot \frac{u_{m+1,n} - u_{m,n}}{\Delta x} + \phi_1 \cdot w^T_{m+1,n} \cdot \frac{u_{m+1,n+1} - u_{m+1,n-1}}{2\Delta\zeta}
$$

$$
= \left(U_e \frac{dU_e}{dx} \right)_{m+1} + \frac{1 + \varepsilon^T_{m+1,n}}{Re} \cdot \ell_1^2
$$

$$
\cdot \frac{u_{m+1,n+1} - 2u_{m+1,n} + u_{m+1,n-1}}{(\Delta\zeta)^2} + \frac{1 + \varepsilon^T_{m+1,n}}{Re} \cdot \phi_2
$$

$$
\cdot \frac{u_{m+1,n+1} - u_{m+1,n-1}}{2\Delta\zeta} + \frac{\ell_1^2}{Re} \cdot \left. \frac{\partial\varepsilon}{\partial\zeta} \right|^T_{m+1,n}
$$

$$
\cdot \frac{u_{m+1,n+1} - u_{m+1,n-1}}{2\Delta\zeta} \tag{29}
$$

where the superscript T indicates a trial value from the preceding iteration. Rearranging into the following general

47

form, Equation 29 becomes

$$A_n u_{n-1} + B_n u_n + C_n u_{n-1} = D_n, \quad 2 \leq n \leq N - 1 \tag{30}$$

where the expressions A_n, B_n, C_n and D_n are given by

$$A_n = w_{m+1,n}^{T} \cdot \phi_1 \cdot \frac{\Delta x}{2\Delta \zeta} - \frac{1 + \varepsilon_{m+1,n}^{T}}{Re}$$

$$\cdot \left(\phi_1^2 \; \frac{\Delta x}{\Delta \zeta^2} + \phi_2 \cdot \frac{\Delta x}{2\Delta \zeta} \right) - \frac{\phi_1^2}{Re} \cdot \left(\frac{\partial \varepsilon}{\partial \zeta} \right)_{m+1,n}^{T} \cdot \frac{\Delta x}{2\Delta \zeta}$$

$$B_n = u_{m+1,n}^{T} + \frac{1 + \varepsilon_{m+1,n}^{T}}{Re} \cdot \phi_1^2 \cdot \frac{2\Delta x}{\Delta \zeta^2}$$

$$C_n = -w_{m+1,n}^{T} \cdot \phi_1 \cdot \frac{\Delta x}{2\Delta \zeta} - \frac{1 + \varepsilon_{m+1,n}^{T}}{Re}$$

$$\cdot \left(\phi_1^2 \cdot \frac{\Delta x}{\Delta \zeta} - \phi_2 \cdot \frac{\Delta x}{2\Delta \zeta} \right) + \frac{\phi_1^2}{Re} \cdot \left(\frac{\partial \varepsilon}{\partial \zeta} \right)_{m+1,n}^{T} \cdot \frac{\Delta x}{2\Delta \zeta}$$

$$D_n = u_{m+1,n}^{T} \cdot u_{mn} + \left(U_e \frac{dU_e}{dx} \right)_{m+1} \cdot \Delta x$$

Applying these equations at each of the nodal points between the surface and outer boundary conditions, results in a system of $N - 2$ algebraic equations as mentioned above. This set of simultaneous equations yields a tridiagonal coefficient matrix which can be solved by an efficient matrix inversion technique involving the following recursion formula:

$$u_n = E_n u_{n+1} + F_n \quad \text{or} \quad u_{n-1} = E_{n-1} u_n + F_{n-1} \tag{31}$$

Substituting into Equation 30,

$$A_n u_{n+1} + B_n u_n + C_n [E_{n-1} u_n + F_{n-1}] = D_n$$

and solving for u_n

$$u_n = \frac{-A_n u_{n+1}}{B_n + C_n E_{n-1}} + \frac{D_n - C_n F_{n-1}}{B_n + C_n E_{n-1}}$$

the unknown coefficients E_n and F_n become

$$E_n = \frac{-A_n}{B_n + C_n E_{n-1}} \tag{32}$$

$$F_n = \frac{D_n - C_n F_{n-1}}{B_n + C_n E_{n-1}} \tag{33}$$

which with Equation 30 define the velocity profile at station m + 1, providing the proper boundary conditions are specified.

The lower boundary condition of a no-slip velocity at the wall is incorporated into Equation 31 to yield values of E_1 and F_1 of zero. Using these initial values E_n and F_n can be calculated through the boundary layer by Equations 32 and 33. The outer boundary condition is used in Equation 31 to initiate the calculation of the velocities toward the wall. However, in order to incorporate the conditions imposed on the velocity by the surface roughness, the above numerical procedure must be altered in calculating the velocities near the wall by applying the logarithmic velocity distribution

49

to the points closest to the lower boundary. Recalling that the logarithmic law implies a layer of constant shear, as shown in Figure 6, page 33, the friction velocity, u_*, will also be constant in this region. Therefore, assuming the value of u_* is given by

$$u_* = \frac{\kappa u(3)}{\ln \left(\frac{z(3) + z_o}{z_o} \right)}$$

the velocity at point 2 can be calculated by the logarithmic law as

$$u(2) = \frac{u_*}{\kappa} \ln \left(\frac{z(2) + z_o}{z_o} \right)$$

and $u(1)$ will remain zero at the wall.

In summary, the method for calculating the velocity profile at $m + 1$ is:

1. Calculate A_n, B_n, C_n and D_n from known values.

2. Calculate E_n and F_n by Equations 31 and 32 starting with $n = 1$ to $n = N - 1$, with $E_1 = 0$, $F_1 = 0$.

3. Calculate $u(n)$ inward from the outer boundary condition to $n = 3$ by Equation 30.

4. Calculate $u(2)$ by the logarithmic law.

The velocity profile in the vertical direction can be obtained by integrating the continuity equation given by Equation 27 using the velocity profile calculated above.

50

$$\overline{w} = -\int_0^z \frac{\partial \overline{u}}{\partial x} \, dz$$

$$\overline{w}(\zeta) = -\int_0^\zeta \left(\frac{\partial \overline{u}}{\partial x}\right)_{m+1} (1/\Phi_1) \, d\zeta$$

Approximating this integral by the trapezoidal rule, the vertical velocity component can be calculated by successively solving the following equation from the wall to the outer edge,

$$w_{m+1}(\zeta_n) = w(\zeta_{n-1}) - \frac{1}{2}\left[\frac{1}{\Phi_1(\zeta_{n-1})} \cdot \left(\frac{u_{m+1,n-1} - u_{m,n-1}}{\Delta x}\right)\right.$$

$$\left. + \frac{1}{\Phi_1(\zeta_n)} \cdot \left(\frac{u_{m+1,n} - u_{m,n}}{\Delta x}\right)\right] \cdot \Delta z$$

The above equation together with Equations 30, 31 and 32 and the boundary conditions give the numerical solution of the boundary layer at station m + 1, after a suitable model of the eddy viscosity and pressure distribution have been introduced.

Comments on Convergence and Accuracy of the Numerical Solution

In developing the numerical solution of the turbulent boundary layer equations, outlined in the previous section a balance between the convergence and accuracy required in the solution and the amount of computing time necessary to meet

these conditions must be consider d. One of the most
important factors affecting this balance is the grid spac-
ing, Δx and Δz, employed in approximating the derivatives by
finite differences. Therefore, the following section will
discuss the effects of this numerical increment size on the
convergence, accuracy and computing time and outline some of
the developmental work done in optimizing the step size.

Convergence of the iterative procedure. The iterative
procedure, previously introduced to solve the numerical
equations, must converge in order to obtain a meaningful
solution of the boundary layer; that is, the difference
between successive approximations of the solution at a
particular x-station, m + 1, must continually decrease as
the number of iterations increases. However, the convergence
of the solution to the exact value, in which the difference
between successive calculations is zero, requires a very
large number of iterations increasing the costs in computing
time well beyond the value of the improvements made in the
solution. Therefore, it is necessary to introduce a small
degree of inaccuracy due to incomplete convergence as a
compromise for reasonable computing time. Thus the optimi-
zation of a numerical scheme involves reducing the number of
iterations (increasing the rate of convergence) required to
efficiently obtain a given level of accuracy.

In any iterative technique, the accuracy of the
initial guess made at the converged solution determines the

52

number of iterations required to reach that solution. In
the present method the initial guess, used in linearizing
the equations, is the calculated velocity profile at the
preceding x-station. Therefore, the strength of the veloc-
ity gradient in the x-direction significantly influences the
rate of convergence and determines the size of the finite
increment in the x-coordinate, as shown in the next section.

The effect of truncation error on accuracy. In addi-
tion, to the errors brought about by incomplete convergence,
the truncation error, or the difference between the solution
of the finite difference equations and that of the differ-
ential equations, is also a problem associated with a
numerical solution. Since the derivatives are approximated
by incomplete series expansions of differences made over
finite distances, the truncation error is a function of the
grid spacing, and ffects not only the rate of convergence
but also the accuracy of the solution, becoming most critical
in regions where the gradients of velocity are the largest.
With this in mind, the initial investigation of the turbulent
solution indicates that the maximum horizontal gradient
occurs in regions where changes in pressure are the most
severe, that is, near the separation regions upstream and
downstream of the obstruction, and that the maximum velocity
gradients in the vertical direction occur near the wall.

Optimization of the numerical scheme in approximating
horizontal gradients in regions of large pressure variation

has been achieved by allowing the horizontal increment spacing, Δx, to vary as a function of the number of iterations required for convergence at a particular x-station. As the iterations increase, Δx is decreased so that the number of iterations is kept below an upper limit. However, for large magnitudes of the adverse pressure gradients, which occur near the separation regions, the iterative procedure will not converge, so that control on Δx will continue to decrease the step size, effectively determining a separation point of the boundary layer.

The truncation errors associated with the approximation of the vertical velocity gradients are also controlled by a variable grid spacing in the vertical coordinate, introduced previously by the stretching function, $\zeta(z)$. Since the velocity gradients are largest at the wall, the most important factor in determining the magnitude of the truncation errors is the physical grid size at the wall, denoted by $(\Delta z)_{z\,=\,0}$. In the present numerical scheme this value is constant throughout the calculation field and is determined as a fraction of the boundary layer thickness of the velocity profile used as an initial condition on the equations.

The following section presents a portion of the work carried out to optimize the numerical technique through an efficient choice of step sizes. Toward this end numerical solutions are compared with experimental data for turbulent flow over a flat plate.

54

Comparison of Numerical Solutions with Known Turbulent Flows

Comparison of the turbulent boundary layer solution with the measured mean velocity profiles of Wieghardt (25) for flow over a smooth flat plate without imposed pressure gradients is given in Figure 9, showing several calculated velocity distributions at one x-location for different values of the vertical increment size $\Delta\zeta$. All calculations were started at an initial station, x_i, well upstream, using a profile interpolated from the data at this point, and were extended downstream using a constant Δx step size of one centimeter, utilizing the Van Driest-Clauser eddy viscosity model, previously discussed.

From earlier discussions, the critical factor in limiting the truncation errors associated with the vertical velocity gradient was determined to be the physical step size at the wall, $(\Delta z)_{z=0}$, which in all calculations is set by the stretching function as 10 per cent of $\Delta\zeta$. The importance of this factor in determining the accuracy of the solution is dramatically illustrated in Figure 9 by the obviously erroneous velocity profile obtained in the calculation employing $(\Delta z)_{z=0}$ of 0.2 millimeters, which represents approximately 2.0 per cent of the initial boundary layer thickness. The other two profiles in this figure, calculated with smaller values of $(\Delta z)_{z=0}$ of 0.5 per cent and 1.0 per cent of the initial boundary layer thickness, respectively, are well behaved with the smallest value giving a slightly better approximation of the data. Figure 10
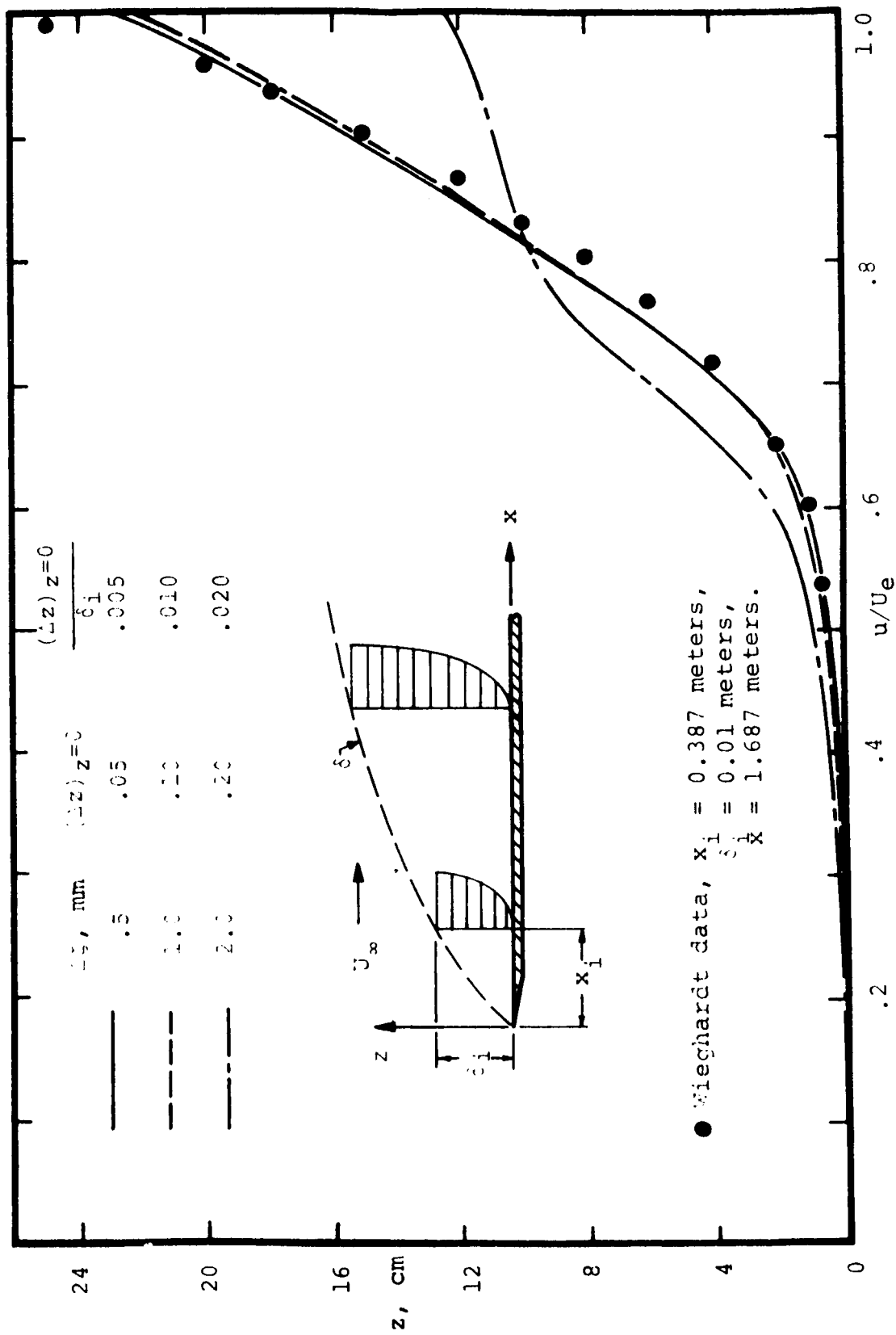
Figure 9. Effect of the variation of numerical increment size
on the velocity profile.
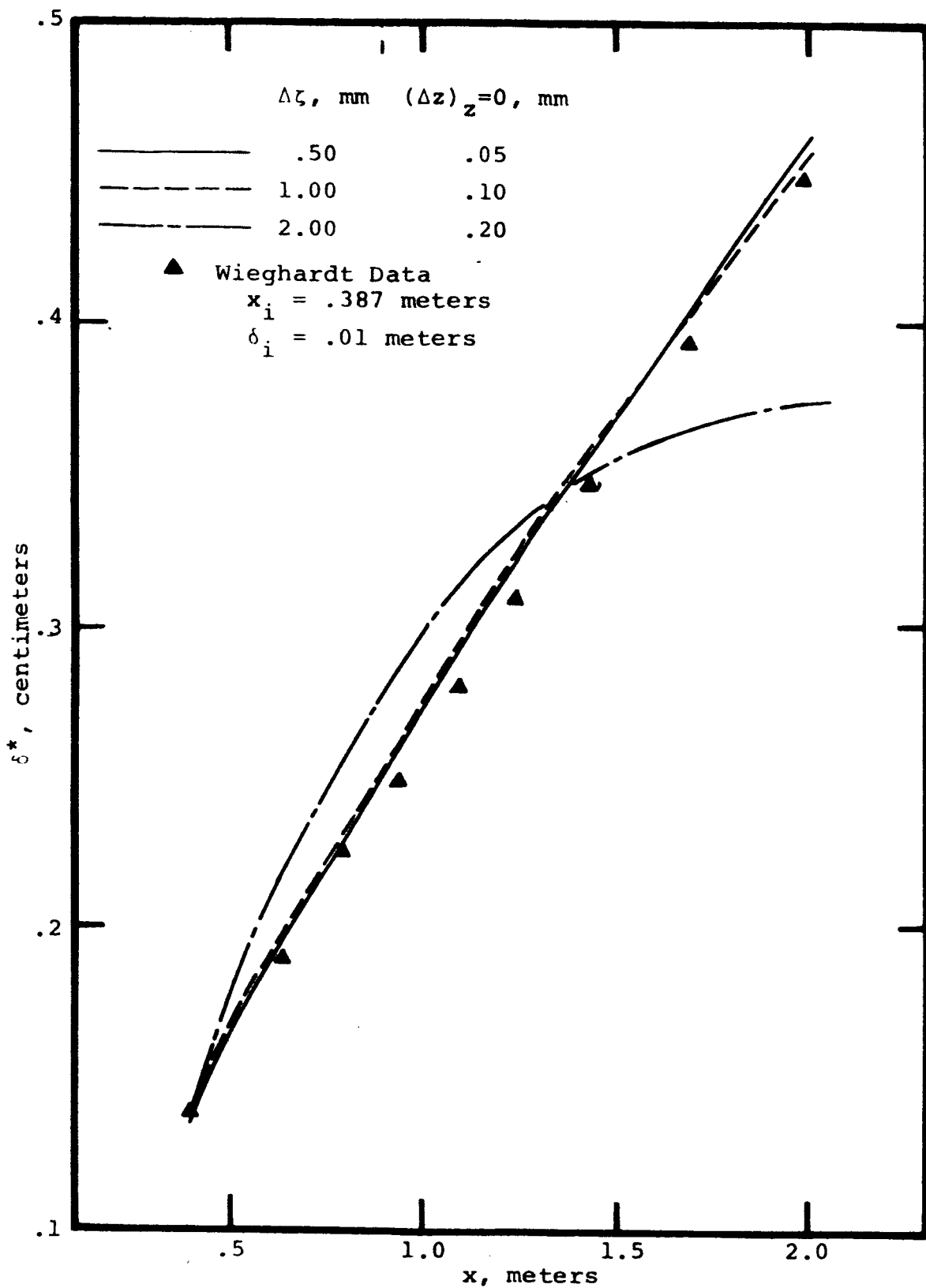
Figure 10. Effect of increment size on δ^*.

illustrates the same influence of $(\Delta z)_{z=0}$ on the calculations of the displacement thickness over the plate.

Based on the above discussion, it was decided to limit the maximum value of $(\Delta z)_{z=0}$ to 1.0 per cent of the initial boundary layer thickness, implying an upper limit on the numerical step size, $\Delta \zeta$, of 10 times this value.

Optimizing the rate of convergence, as previously discussed, by controlling the number of iterations through variation of Δx, basically determines the size of this increment. However, Δx was not allowed to grow to a magnitude of larger than 10 times $\Delta \zeta$ in order to control the truncation error introduced by the approximation of the horizontal gradients.

CHAPTER IV

DISCUSSION OF RESULTS FOR THE FLOW FIELD

NEAR ELLIPTICAL OBSTRUCTIONS

Numerical solutions of the turbulent boundary layer
equations have been carried out for a number of different
cases involving atmospheric flow over elliptical cylinders
of various aspect ratios and surface roughnesses. The
results of these calculations are divided into two types:
the first, presented in this chapter, involves the analysis
of the flow field in a region above the obstruction on the
order of one ellipse height in which the pressure gradient
and outer boundary condition are specified along the non-
separating streamline; and the second, to be presented in
Chapter V, in which the analysis is extended to include the
flow field in a larger region of influence above the
elliptical cylinder, incorporates the decaying pressure
distribution and outer boundary conditions dictated by the
logarithmic velocity.

Considering the flow field close to the body, the
following solutions are obtained from a region of calcula-
tion shown in Figure 11. The calculation procedure,
described in Chapter III, is initiated with the logarithmic
velocity profile, characteristic of the approaching wind, at
a position upstream of the body of 20 times the height of
the ellipse. This location is chosen because it represents
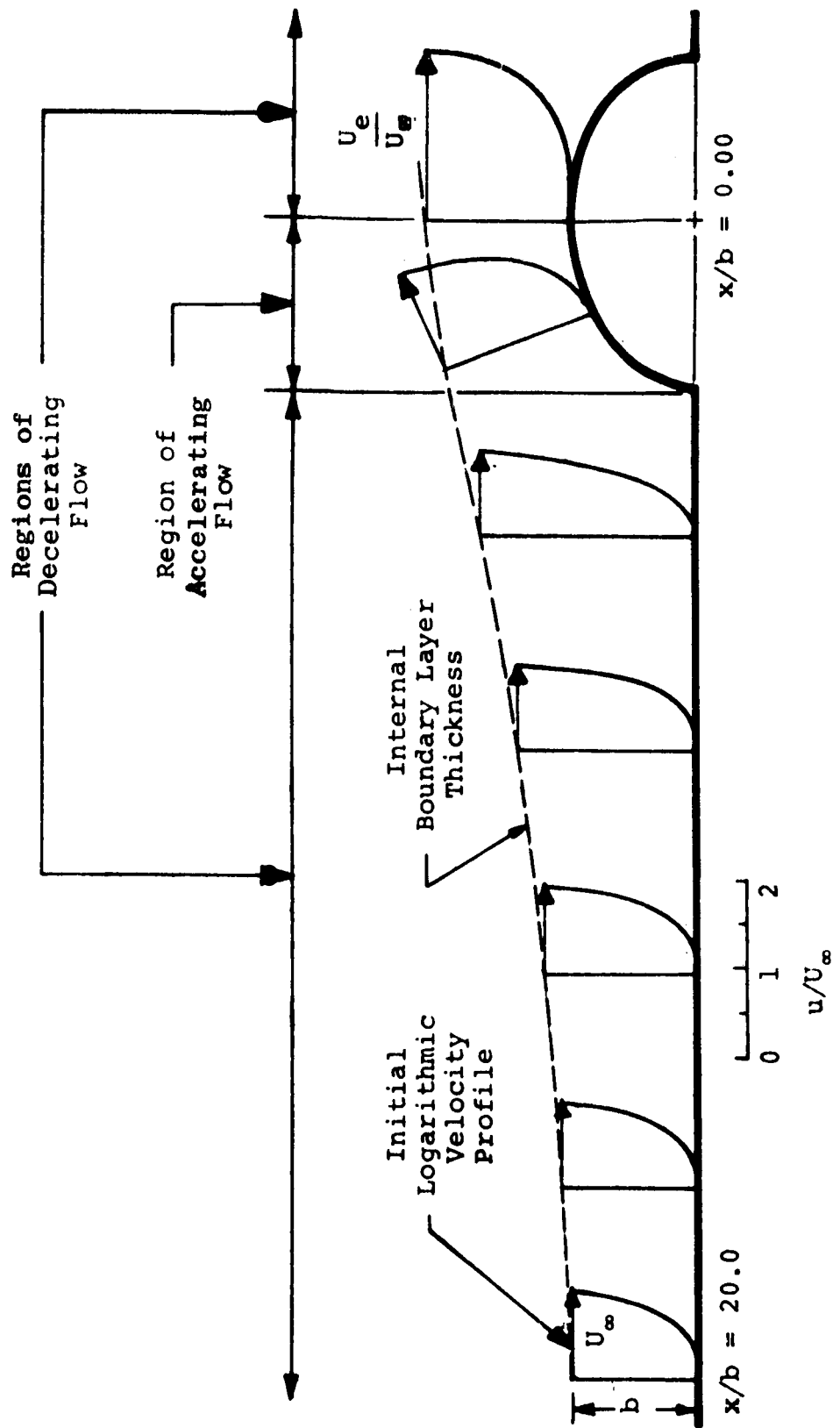
Figure 11. Region of solution for flow over an elliptical cylinder.

a distance outside of which the pressure disturbance created by the obstruction is less than one per cent of the free stream pressure. Proceeding downstream, the velocity profiles are calculated as shown, using the potential velocity, U_e, as an outer boundary condition, passing through the region of adverse pressure where the velocities decrease and the boundary layer grows to the favorable pressure on top of the ellipse where the flow is accelerated.

The results of this calculation of the boundary layer over the elliptical obstruction can be conveniently discussed in terms of three relevant parameters which evolve from the dimensionless governing equations. Inspection of the boundary layer Equations 25 and 26 and the assumptions concerning the pressure field and boundary conditions which apply, identifies these parameters as: first, the aspect ratio, k, of the elliptical cylinder, defined as the ratio of the length major axis which is parallel to the ground, to the height of the ellipse which has been fixed in all cases considered to a value of one meter; second, the surface roughness characterized by a vertical length scale, z_o; and third, the Reynolds number, expressed in terms of the height of the elliptical cylinder, b, and a characteristic velocity, U_{xo}, defined at this same height by the logarithmic velocity law.

The Effect of Elliptical Aspect Ratio on the Boundary Layer

The effects of a parametric variation of the aspect

61

ratio on the velocity profiles at the top of the ellipse are shown in Figures 12 and 13 for two different surface roughnesses. The apparent unusual behavior of the curves at the coordinate position (1, 1) can be explained both by the nature of the boundary condition chosen and by the smoothing effect of the numerical integration. In the former case u/U_e becomes unity at an elevation slightly greater than $z/b = 1$ due to the displacement of the potential solution streamlines along which U_e is evaluated. The forcing of the solution by the boundary conditions makes the solution in this region less reliable than the remaining portion of the velocity profile. In both cases, the effect of increasing the aspect ratio is a decrease in the mean wind velocity at the top of the ellipse. It is also of interest to compare the changes produced by the different ellipses in the initial logarithmic velocity profile existing far upstream. For the low aspect ratios, the velocity profiles show wind speeds at the top which are greater than the approaching wind, but the larger aspect ratio produces velocities which are very close to the initial logarithmic distribution, characteristic of the undisturbed flow, deviating significantly only in the outer portion of the profile where the boundary layer growth causes a decrease in velocity from the initial values.

The effect of the elliptical aspect ratio on the velocity profiles can be explained in terms of the pressure field assumed to exist over the cylinders as shown in Figure 14.
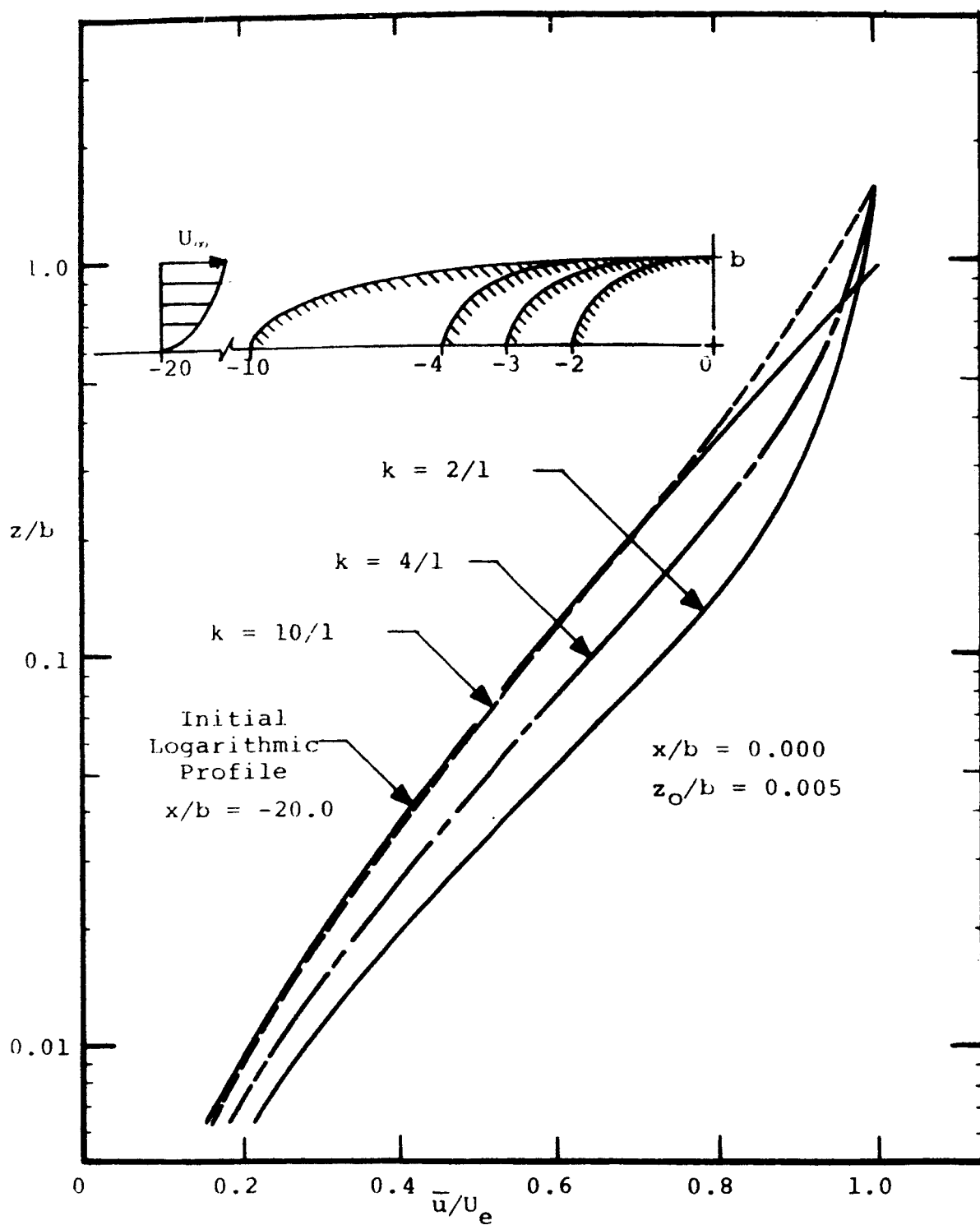
Figure 12. Effect of elliptical aspect ratio on velocity profile at the top of the ellipse for $z_0/b = 0.005$.
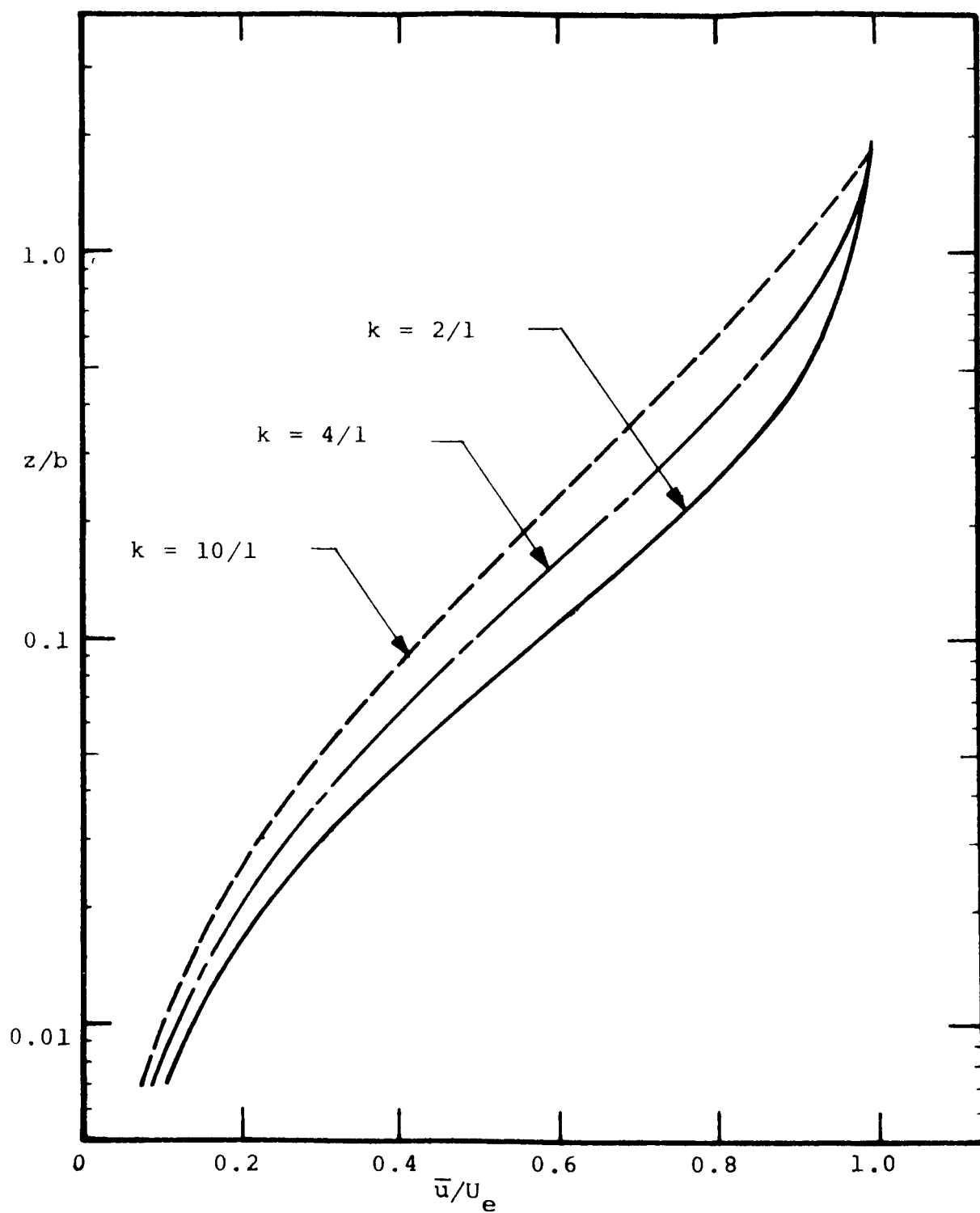
Figure 13. Effect of elliptical aspect ratio on velocity
profile at the top of the ellipse for z_o/b = 0.020.

64

$\dfrac{p - p_\infty}{\rho U_\infty^2}$

.40

.20

-.20

-.40

-.60

-.80

x/b

-16 -14 -12 -10 -8 -6 -4 -2

k = 10/1, δ = .55
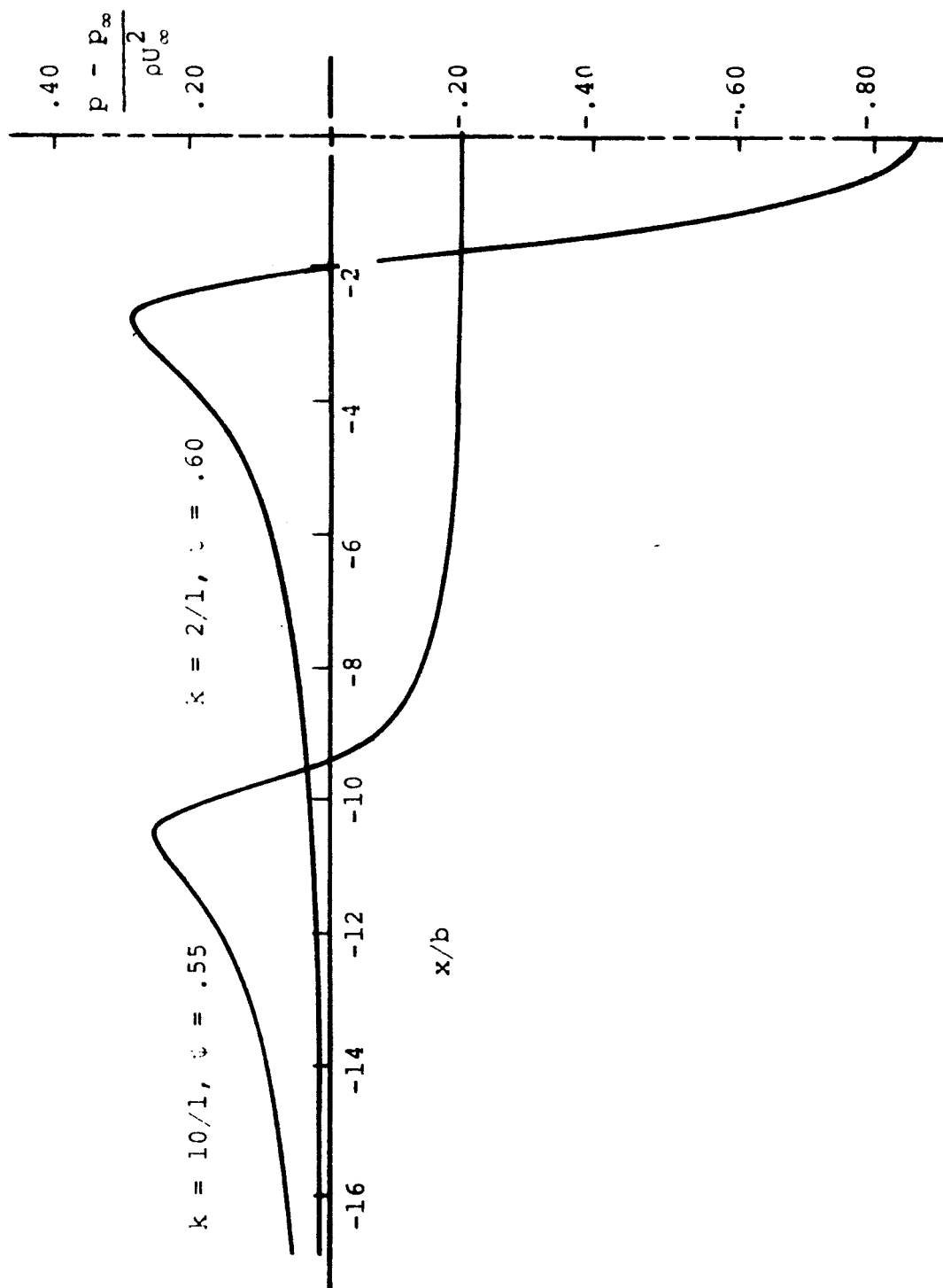
k = 2/1, δ = .60

Figure 14. Comparison of the pressure distribution over a 10/1 and 2/1 elliptical cylinder.

Comparing the adverse pressure gradient given along the nonseparating streamlines for the large and small aspect ratio, it is apparent that the pressure distributions are very similar with the 2/1 ellipse having only a slightly larger gradient. On the other hand, the favorable pressure gradient is obviously quite different for the two cases. For the 10/1 ellipse the gradient is large only for a short distance near the leading edge then rapidly decreases to a very small value over a significant portion near the top of the ellipse. For the 2/1 ellipse the favorable gradient is much larger approaching zero only in a very small region at the top of the cylinder. The additional acceleration given to the flow by this larger pressure force is the primary cause of the higher wind speeds shown in Figures 12 and 13 at top of the smaller aspect ratio ellipses. In addition, the fact that the velocity tends to return to the logarithmic distribution at the top of the longer ellipse can also be explained by considering the region of a favorable pressure gradient. Recalling that the logarithmic velocity is characteristic of zero pressure gradient flow, it is not surprising that the boundary layer at the top of the 10/1 ellipse approaches the logarithmic form of the upstream, undisturbed wind profile.

The Effect of Surface Roughness on the Boundary Layer

The effects of variation in surface roughness on the velocity of the wind at the top of the 2/1 and 10/1 ellipses are shown in Figures 15 and 16, respectively, for several
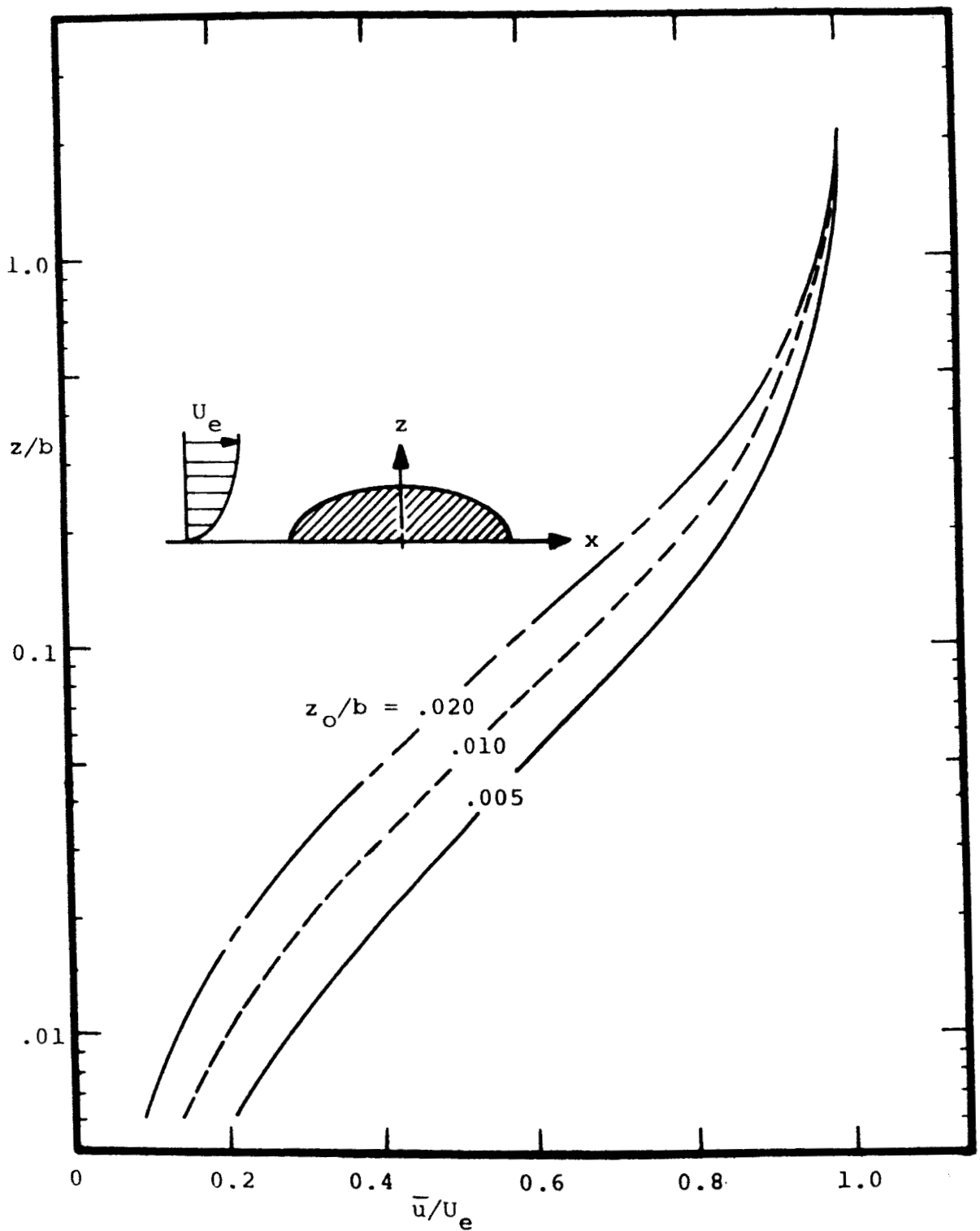
66

Figure 15. Effect of surface roughness on the velocity
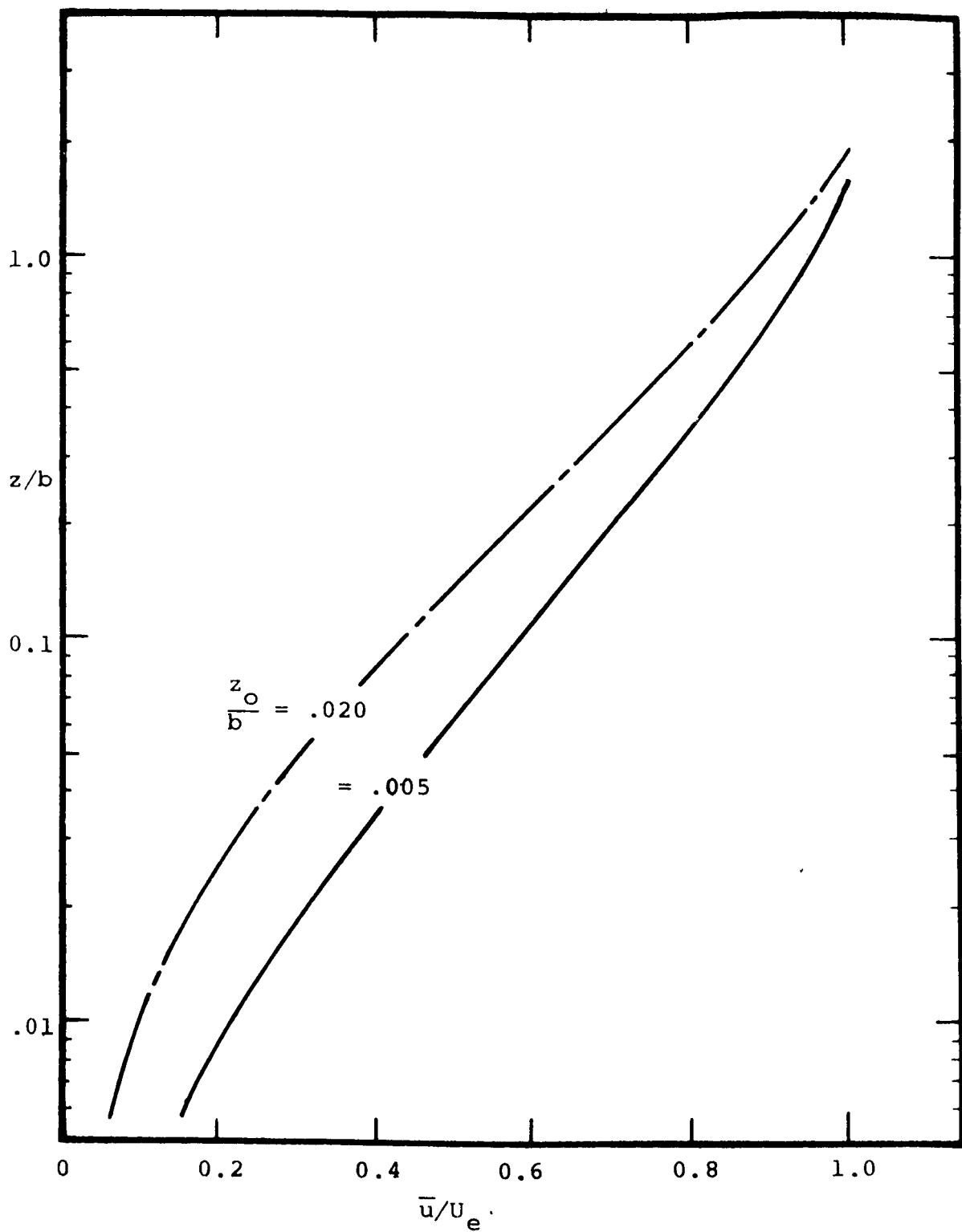profiles at the top of the 2/1 ellipse.

Figure 16. Effect of surface roughness on the velocity profiles at the top of 10/1 ellipse.

different roughness values, z_o/b, ranging from 0.005 to 0.020. The decrease in the velocity at the top of the two ellipses caused by increasing the roughness, can readily be explained by examining the influence of the individual roughness elements on the flow in the vicinity of the ground. As discussed previously, there are two effects produced by the protrusions of the surface into the flow: the first is the increased drag of the fluid on the surface caused by the separation of the boundary layer on a small scale; and the second is the larger shear brought about by the more turbulent eddying motion produced in the region close to the surface. Both of these effects are enhanced by larger roughness creating a greater dissipation of the momentum through the boundary layer.

Comparing the effects of an increase in roughness on the two different ellipses shown in Figures 15 and 16, it appears that the roughness change does not influence the flow fields for the two different aspect ratios to the same degree. This is more apparent in Figure 17 where the difference, Δu, in velocity calculated with roughness $z_o/b = 0.005$ and that for $z_o/b = .020$ is plotted as a function of height above the surface. From this figure it is obvious that increased roughness has more influence on the boundary layer near the surface of the 2/1 ellipse than the 10/1, but that this influence decays rapidly toward the outside of the surface layer causing roughness effects to become more influential in the outer region for the 10/1 ellipse.
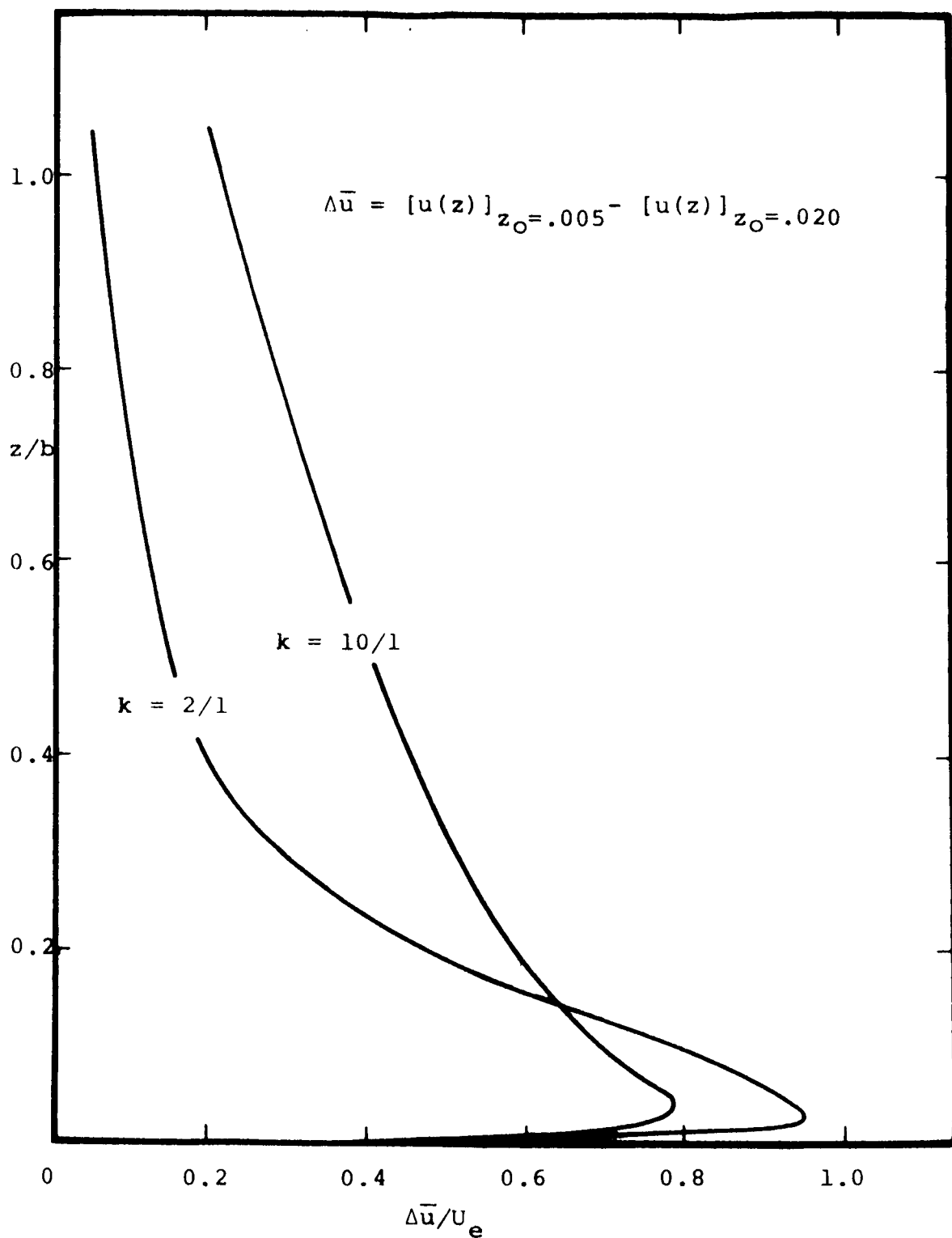
$$\Delta \bar{u} = [u(z)]_{z_O=.005} - [u(z)]_{z_O=.020}$$

k = 10/1

k = 2/1

$\Delta \bar{u}/U_e$

Figure 17. Comparison of the effects of changes in surface
roughness on velocity profile at the top of the 2/1
and 10/1 ellipse.

70

These results can be explained by again comparing the pressure field over the top of the 2/1 and 10/1 elliptical cylinders. As previously discussed the pressure gradients which exist along the top of the larger aspect ratio ellipse are extremely small, so that the force created by this gradient is negligible, and the momentum of the flow in regions near the top of the 10/1 ellipse is effectively determined by the viscous forces only. Therefore, the viscous effects produced by the surface roughness extend much further into the boundary layer for the 10/1 ellipse, explaining the larger values of Δu calculated in the outer region of the boundary layer as observed in Figure 17.

On the other hand, the much larger favorable pressure gradients which exist over the top of the 2/1 ellipse have an influence on the flow which can be used to explain the effects of a change in roughness observed near the surface. Because of the larger acceleration produced by these favorable pressure forces, the velocity gradient near the wall is greater for the 2/1 ellipse than for the 10/1 ellipse. Therefore, since the viscous shear is directly related to this gradient, the effects of roughness will also be larger in this region, leading to the results shown in Figure 17.

The Reynolds' Number as a Parameter

Nondimensionalizing the governing equations by a characteristic length and velocity produces the Reynolds' number as a parameter of the boundary layer. However, by defining the Reynolds' number in terms of the logarithmic

71

wind profile which exists far upstream, it is no longer an independent parameter of the equations but becomes a function of the surface roughness, as shown in the following equation:

$$Re = \frac{U_\infty b}{\nu} = \frac{b}{\nu} \frac{u_{*_O}}{\kappa} \ln\left(\frac{b + z_O}{z_O}\right) \tag{34}$$

On the other hand, this definition of the Reynolds' number introduces a new variable into the problem as the initial friction velocity of the undisturbed flow, u_{*_O}, which has been chosen as the independent parameter, entering the equations through the Reynolds' number.

The influence of the initial friction velocity on the overall flow field is illustrated in Figure 18 by the distribution of the displacement thickness over the 2/1 aspect ratio ellipse. Two curves are shown, one for a value of $u_{*_O} = 0.40$ meters/second and the other for $u_{*_O} = 1.00$ meters/second which correspond to Reynolds' numbers of 3.8×10^5 and 9.5×10^5, respectively. For the values of friction velocity used in these two calculations, the maximum change occurring in the displacement thickness for an increase in u_{*_O} by a factor of 2.5 is only 0.87 per cent. Thus, it is suggested that the Reynolds' number, on the order of the magnitudes given above, has little effect on the boundary layer. This conclusion can also be verified by examining the nondimensional boundary layer equation (Equation 24). Expressing the eddy viscosity derived from
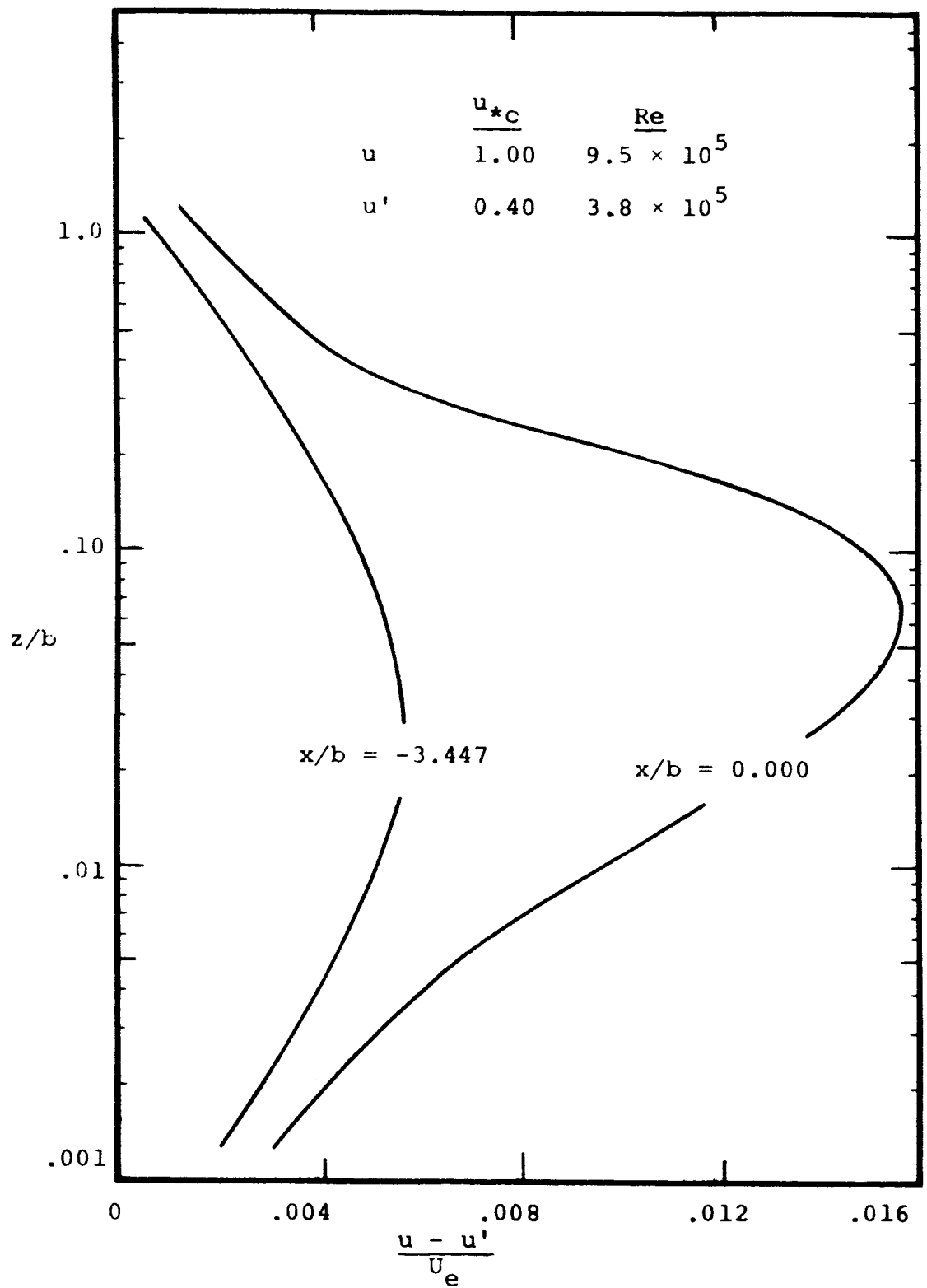
Figure 18. Effect of Reynolds' number on the velocity profile at the top of the ellipse for $z_o/b = .005$.

the mixing length concept as given in Equation 15 in non-dimensional terms,

$$\varepsilon^* = \frac{\varepsilon}{\nu} = \frac{U_\infty b}{\nu} \left[\kappa\ z/b\right]^2 \frac{\partial(\bar{u}/U_\infty)}{\partial(z/b)}$$

$$\varepsilon^* = Re\ \kappa^2 z^{*2} \frac{\partial \bar{u}^*}{\partial z^*}$$

and substituting into Equation 24 results in the following expression for the boundary layer equation:

$$\bar{u}^* \frac{\partial \bar{u}^*}{\partial x^*} + \bar{w}^* \frac{\partial \bar{u}^*}{\partial z^*} = U_e^* \frac{dU_e^*}{dx^*} + \frac{\partial}{\partial z^*}\left[\left(\frac{1}{Re} + \kappa^2 z^{*2} \frac{\partial \bar{u}^*}{\partial z}\right)\frac{\partial \bar{u}^*}{\partial z^*}\right]$$

(35)

It can be seen from this equation that the effect of the Reynolds' number will be negligible through a majority of the boundary layer if the Reynolds' number is large as is characteristic of atmospheric flows.

Although the overall effect of the Reynolds' number is small, it is also evident from Equation 35 that very near the wall where the turbulent shear is decreased, the importance of the Reynolds' number is increased. This is clearly demonstrated in Figure 19 by comparing the changes in the velocity profiles produced by the Reynolds' numbers considered above. A velocity difference, u - u', is plotted as a function of height above the surface, where u is the wind velocity calculated with an initial friction velocity of 1.00 meters/second, and u' is the wind velocity for a
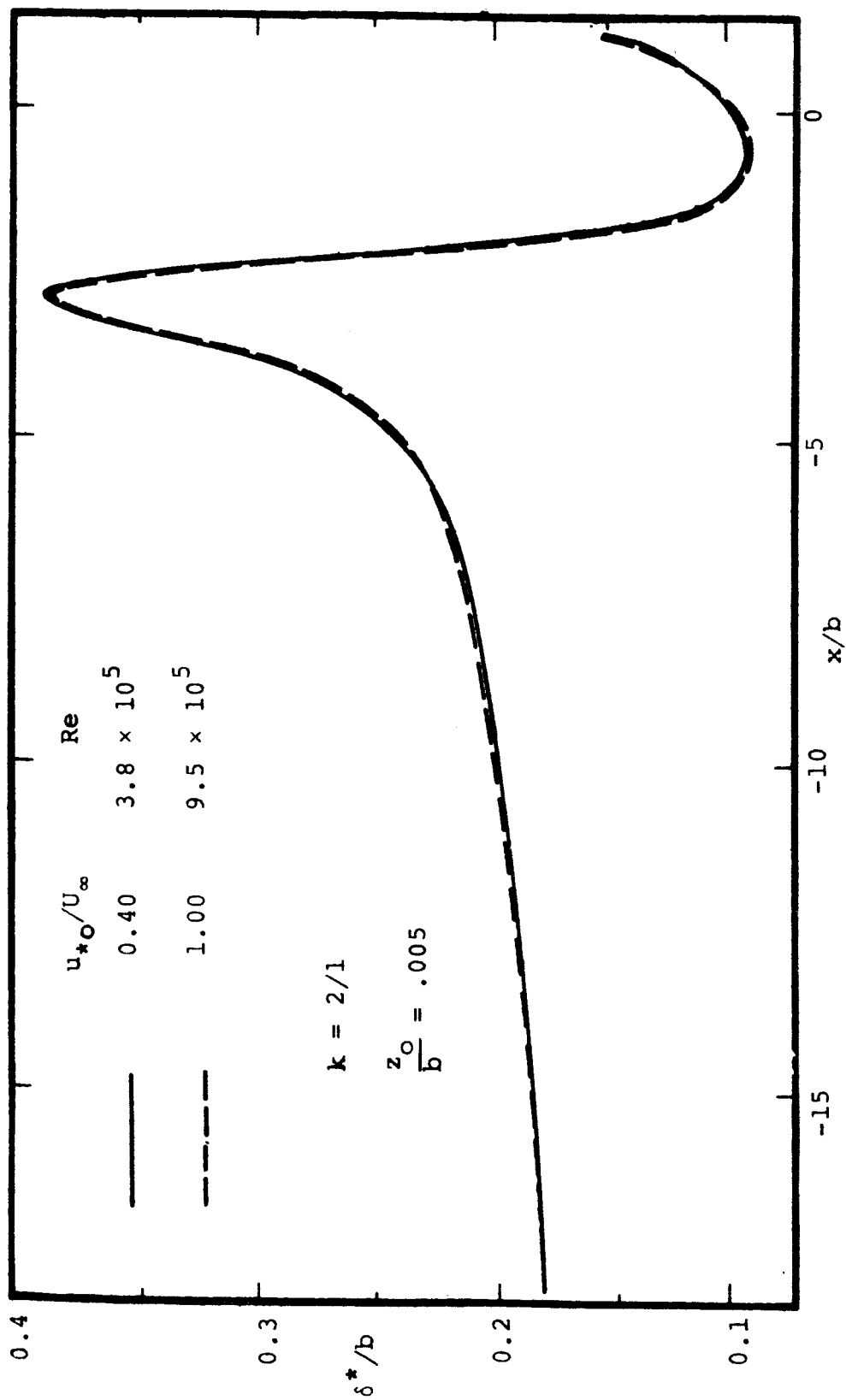
Figure 19. Effect of the initial friction velocity and Reynolds' number on the displacement thickness.

75

friction velocity of 0.40 meters/second. The corresponding mean wind speed, U_∞, for these two cases is 12 miles/hour and 30 miles/hour, respectively. Figure 19 confirms that the predominant influence of the change in Reynolds' number brought about by increasing the initial friction velocity, is confined to a region near the wall, with the effect being most significant at the top of the ellipse where the velocity gradients and shear stresses are large. The other profile is calculated at a position upstream near the forward separation region where the adverse pressure field causes the velocity gradients and stresses to be relatively smaller.

The Effect of Roughness and Ellipse Geometry on Separation

The severe adverse pressure gradients which exist upstream from the body cause separation of the boundary layer near the stagnation region. Since the numerical solution, as discussed in Chapter III, gives a reasonably accurate prediction of the point at which this separation occurs, a characteristic length of the forward separation bubble can be determined. This calculation has been carried out for a number of elliptical aspect ratios and surface roughnesses and is given in Figure 20. Examining the effect of roughness on the length, λ, of the separation region, it is apparent that a decrease in z_o produces smaller separation regions tending to approach some asymptotic value for a smooth surface. This is expected since roughness reduces the velocity near the surface decreasing the momentum available to overcome the adverse pressure forces.
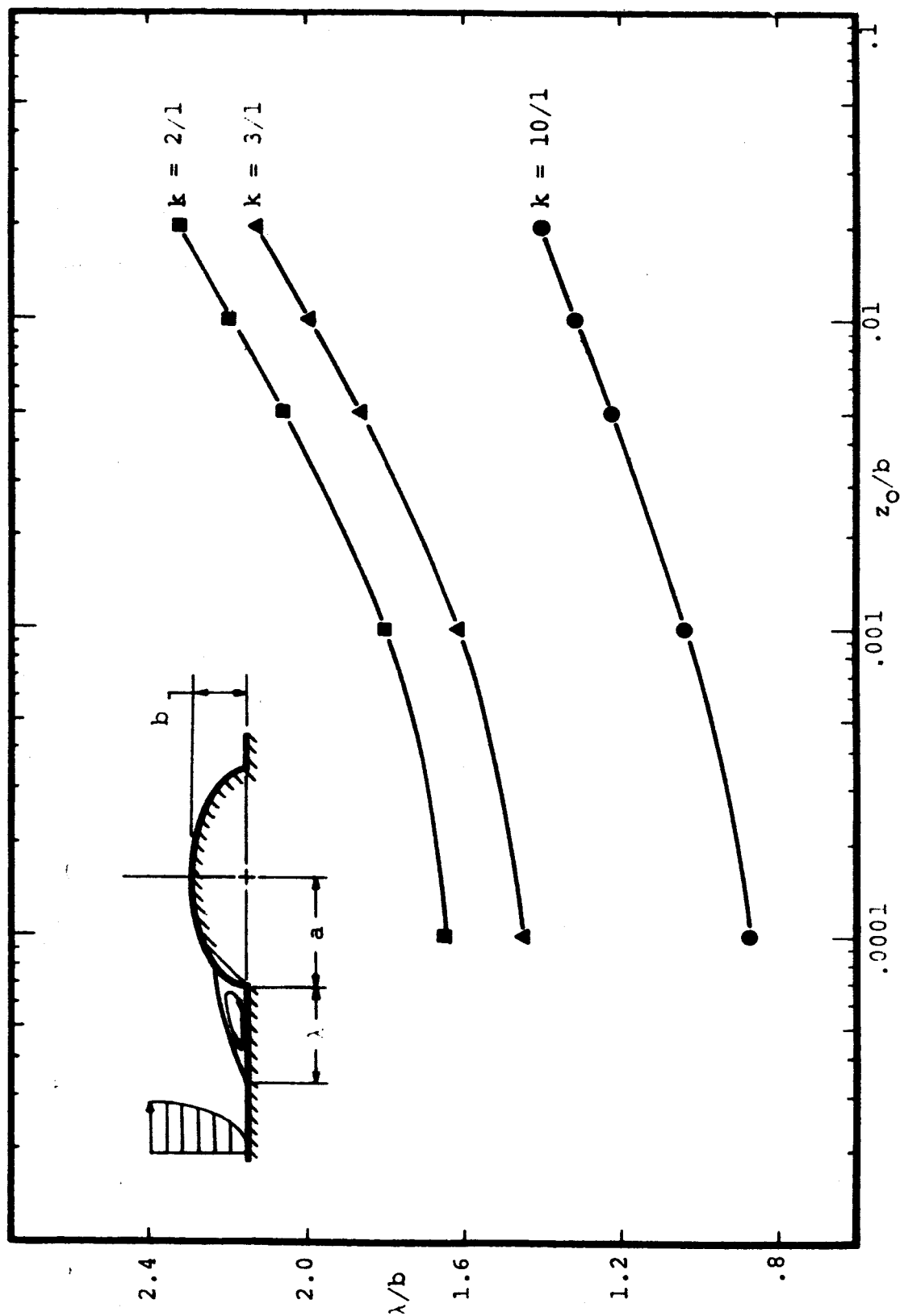
76

Figure 20. Elliptical geometry and surface roughness effects on the length of the separation regions.

The effect of the aspect ratio on the length of the
separation is similar to that of the roughness, with the
longer ellipses producing smaller separation bubbles. This
fact can be explained by examining the pressure distribution
over the cylinders as shown in Figure 14, page 65. As
pointed out in the discussion of that figure, the adverse
pressure gradient upstream from the body is more severe for
the smaller aspect ratio ellipse, leading to the conclusion
that separation occurs further upstream for the shorter
ellipses.

Geometrical Effects on the Turbulent Viscosity

It is not only important to determine the effects of
the elliptical geometry on the mean velocity field, but it
is also desirable to examine the influence of the obstruc-
tion on the turbulent characteristics of the flow.

This has been done in Figure 21 showing the develop-
ment of the eddy viscosity profiles over the 10/1 ellipse.
Starting far upstream the eddy viscosity profile, given by
curve A, is calculated by Equation 15 from the initial
logarithmic velocity distribution. Proceeding downstream
under the influence of a mild adverse pressure gradient,
the next profile, given in Figure 21 by curve B, is at a
position upstream of the forward stagnation point of about
twice the ellipse height. It can be seen in comparison with
curve A, that the viscosity has decreased slightly in the
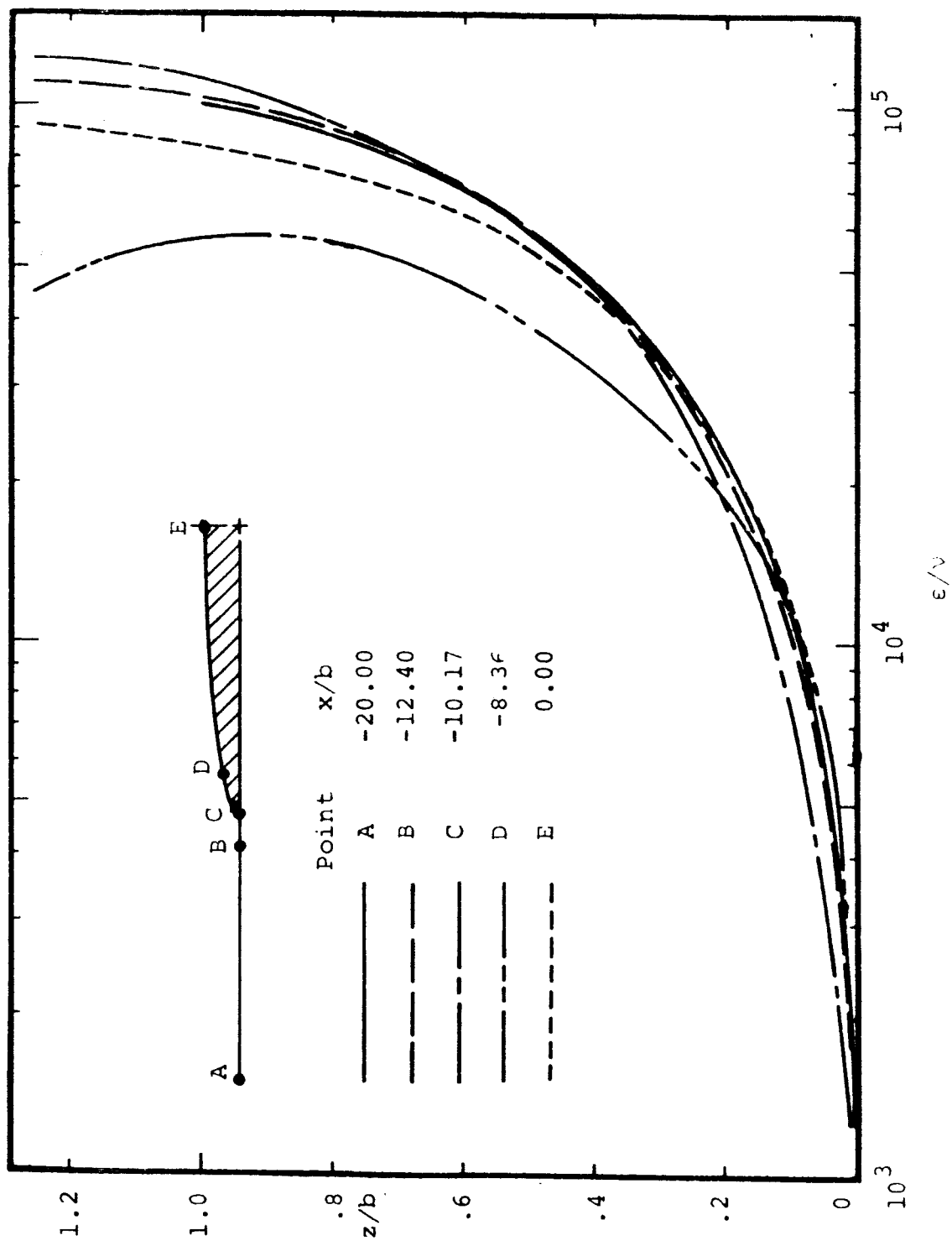lower region of the boundary layer becoming larger near the

78

Figure 21. Development of the eddy viscosity profiles over a 10/1 ellipse with $z_o/b = .005$.

outer edge. Curve C is calculated over the stagnation point where the imposed mean pressure gradient first becomes favorable. This profile continues the trend discussed above with the viscosity reaching a maximum near the outer edge. The profile given at point D, is calculated at a position downstream of the maximum favorable pressure gradient and exhibits a drastic change from the pattern established by the first three curves, with the eddy values increasing to local maximum values near the wall and decreasing rapidly to minimum values in the outer boundary layer. And, finally, the last profile, calculated at the top of the ellipse (point E), well downstream from D, shows the effect of the very small pressure gradient existing over a large portion of the cylinder. The response of the eddy viscosity to the influence of this negligible pressure field is similar to that of the velocity, tending to return to the form of the undisturbed flow upstream. This fact is not surprising, however, because the eddy viscosity, calculated by the Prandtl mixing length model, is directly related to the vertical gradient of the velocity.

Therefore, the results given in Figure 21 can be explained by examining the effect of the pressure forces on the velocity. Since adverse pressure decelerates the flow reducing the gradient in velocity near the wall while increasing it in the outer flow, the turbulent shear will show a similar effect as illustrated in comparing curves A, B and C of Figure 21. On the other hand, the favorable

pressure gradients over the front of the ellipse will have
the opposite effect, as shown by curve D with the large
increase in eddy viscosity occurring near the wall decreas-
ing rapidly in the outer boundary layer.

Calculation of Flow Over a Fence with Comparison to Data

In addition to the results previously discussed for
atmospheric flow over the elliptical cylinders, several
calculations have been carried out for flow over a fence, or
two-dimensional vertical flat plate, which represents the
limiting case of the elliptical cylinder with zero aspect
ratio. This particular flow situation has a number of
practical applications as a wind-sheltering device and has,
therefore, been the subject of a number of experimental
studies (4), (11) and (12).

Applying the concepts developed within this study to
flow over the fence, approximations of some representative
data (12) can be made. Results of this calculation are
given in Figure 22 and are compared with measured velocities
upstream and on top of the fence. All calculations are
carried out over a smooth surface using the Van Driest-
Clauser eddy viscosity model with pressure distribution and
outer boundary conditions given by the potential flow values
along the first nonseparating streamline. The particular
potential solution used in these calculations is obtained
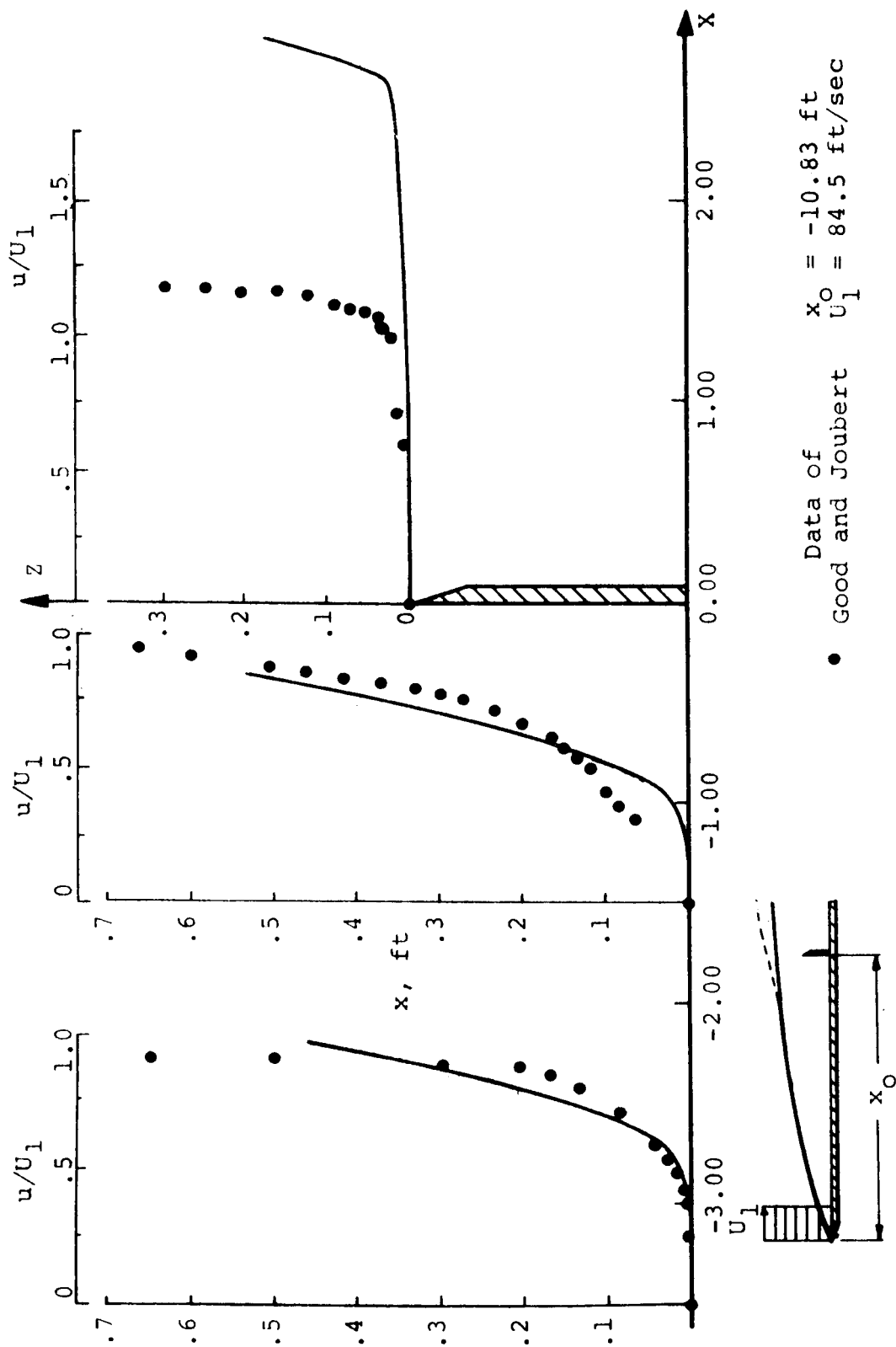from Reference (23) assuming a symmetric flow over the
fence.

Figure 22. Comparison of numerical calculation with data for flow over a fence.

Data of
Good and Joubert

x_o = -10.83 ft
U_1^o = 84.5 ft/sec

Examining the two profiles upstream of the fence it appears that the numerical solution overpredicts the velocity near the wall with smaller predicted values in the outer edge of the flow. This is probably due to the large pressure gradient physically existing in the vertical direction which decelerates the flow near the surface to a much greater extent than the assumed mean pressure gradient along the nonseparating streamline. The calculated profile at the top of the fence, while exhibiting a similar form to the measured profile, predicts much larger velocities in the boundary layer. This effect is due to the outer boundary conditions obtained from potential theory which do not take into account the very large separation regions both upstream and downstream of the plate. Because of the large decelerations produced by these regions, a potential solution which includes these effects would be a better approximation of the actual flow conditions, and more accurately predict the magnitude of the velocity.

Both of the above effects produced by the large separation regions which exist in a major part of the flow field surrounding the fence, can be taken into account to some extent by the methods introduced in Chapter II. Since the pressure gradient imposed on the boundary layer by reversed flow regions is much larger for the case of the fence than for the elliptical cylinder, the former flow situation provides a severe test for the methods proposed in this investigation. However, with improved approximations

of the pressure field and boundary con   .ions, it is

believed that the boundary layer approach can make reason-

able predictions of the flow field over the fence.

CHAPTER V

DISCUSSION OF RESULTS FOR AN IMPROVED BOUNDARY

LAYER ANALYSIS OF FLOW OVER

ELLIPTICAL OBSTRUCTIONS

Analysis of Enlarged Flow Fields

The consideration of flow fields in a larger region
above the elliptical obstruction than that discussed in the
preceding chapter requires approximations of the outer
boundary condition on the mean wind and the pressure dis-
tribution over the obstacle which are more characteristic
of atmospheric flow in this enlarged region than conditions
prescribed along the nonseparating streamline. As discussed
in Chapter II, the outer boundary condition which is a
realistic approximation of the flow far from the surface is
given by an asymptotic matching of the velocity within the
boundary layer to the logarithmic velocity associated with
the undisturbed flow. In conjunction with this boundary
condition it was also pointed out that the pressure gradients
associated with the obstruction must decay to zero from the
value given along the nonseparating streamline. Therefore,
the initial approximation of the pressure field existing
within the region of influence of the elliptical cylinder,
is given by the following second order quadratic decay
function:

$$q(z) = \begin{cases} 1 & \dfrac{z}{b} < .50 \\[2ex] \left(\dfrac{0.5}{z}\right)^2 & \dfrac{z}{b} \quad .50 \end{cases}$$

$$\frac{dp(x,z)}{dx} = \left(\frac{dp(x)}{dx}\right)_{ns} \cdot q(z)$$

where $\left(\dfrac{dp(x)}{dx}\right)_{ns}$ is the pressure gradient determined along

the nonseparating streamline over the obstruction.

Preliminary calculations of the flow field in an enlarged region over the elliptical cylinder, using the above pressure distribution and logarithmic outer boundary condition, have been carried out for flow over the 2/1 and 4/1 aspect ratio ellipses with different roughnesses. The results of these calculations for the 2/1 ellipse are given in Figures 23 and 24 showing the development of the boundary layer from a position upstream of 10 times the ellipse height to the top of the cylinder. This initial location is chosen in order to reduce the computing time required for these preliminary calculations. The logarithmic boundary condition is applied at a constant height above the surface of five times the ellipse height, with the solutions non-dimensionalized by the logarithmic velocity defined for convenience at a position of three times the ellipse height. One observes from the curves that the flow is initially decelerated from the starting profile at $x/b = -10.0$ through the range of approximately $x/b = -3.0$ and then is accelerated to the top of the ellipse, $x/b = 00$. Similar results are

86

Figure 23. Development of the boundary layer over a 2/1 ellipse with variable pressure gradient in the vertical direction and logarithmic outer boundary condition for z_o/b = .005.

87
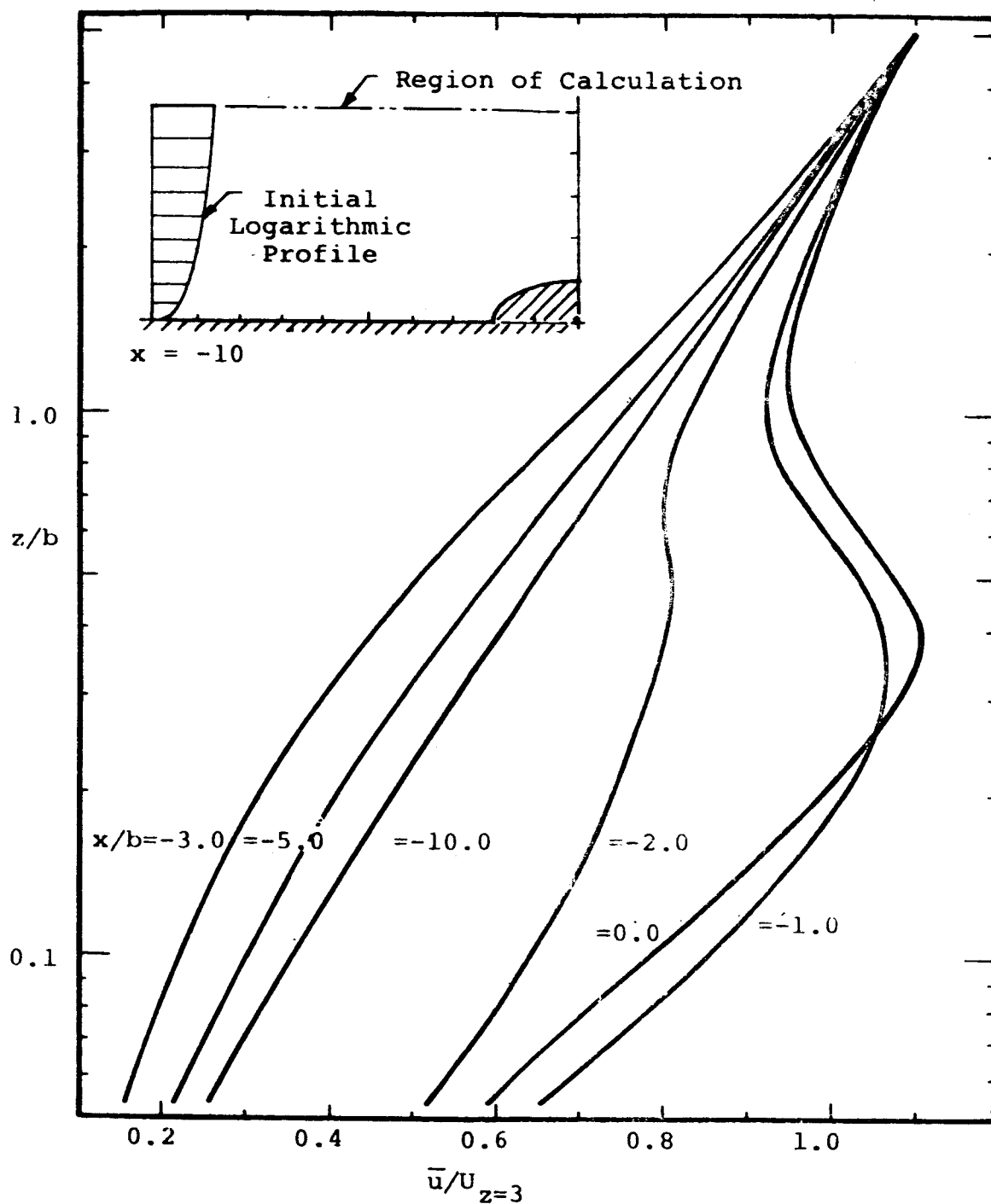
Figure 24. Development of the boundary layer over a 2/1 ellipse with variable pressure gradient in the vertical direction and logarithmic outer boundary condition for z_o/b = .020.

88

shown in Figures 25 and 26 for the 4/1 ellipse.

Comparing these results with the velocity profiles presented in the previous chapter, the most significant effect of the vertical variation of the pressure gradient is the pronounced maximum in the wind velocity produced locally near the surface for the calculations made over the top of the ellipse. This result is due to a combination of the large accelerations created by the favorable pressure gradients which exist in this region of the flow field, and the influence of the decaying pressure function imposed on these gradients which decreases the acceleration, allowing the flow to return to the logarithmic velocity at large heights above the surface.

The acceleration of the boundary layer occurs from a position $x/b = -3.0$ to the top of the ellipse where the maximum wind velocities are attained at an elevation of about 0.3 times the ellipse height. In magnitude the wind is accelerated to about twice its initial value. This compares to calculations discussed in the previous chapter in which the maximum velocity at the top of the 2/1 ellipse was only 35 per cent greater than the initial wind speed.

However, returning to the solutions given in Figures 23 through 26, consider the flow far upstream. Since the pressure disturbances created by the obstruction are small, the effect of the vertical decay of the pressure gradient is negligible, with the form of the velocity profiles decreasing only slightly from the initial logarithmic distribution.
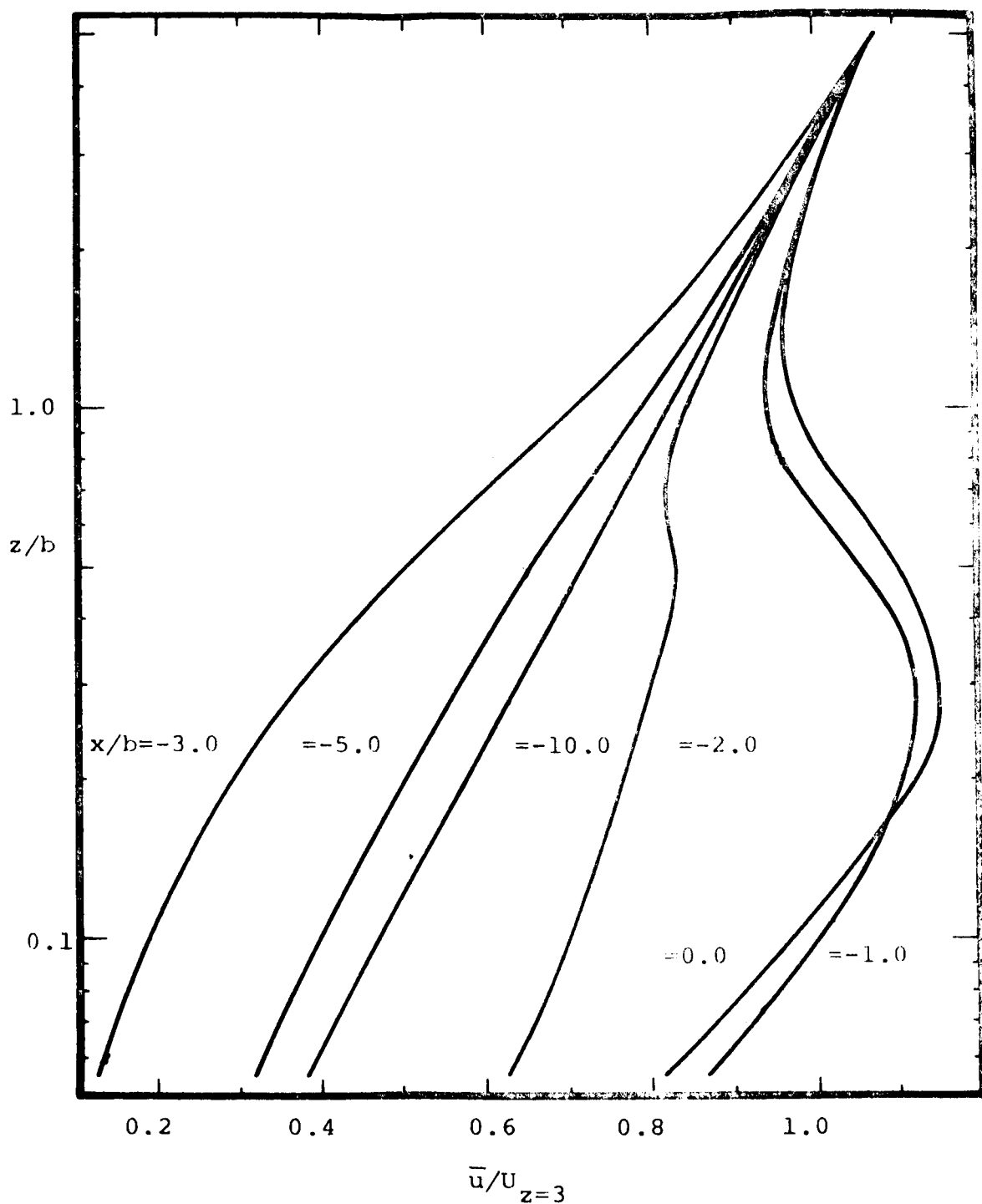
Figure 25. Development of the boundary layer over a 4/1
    ellipse with variable pressure gradient in the vertical
    direction and logarithmic outer boundary condition for
    z_o/b = .005.

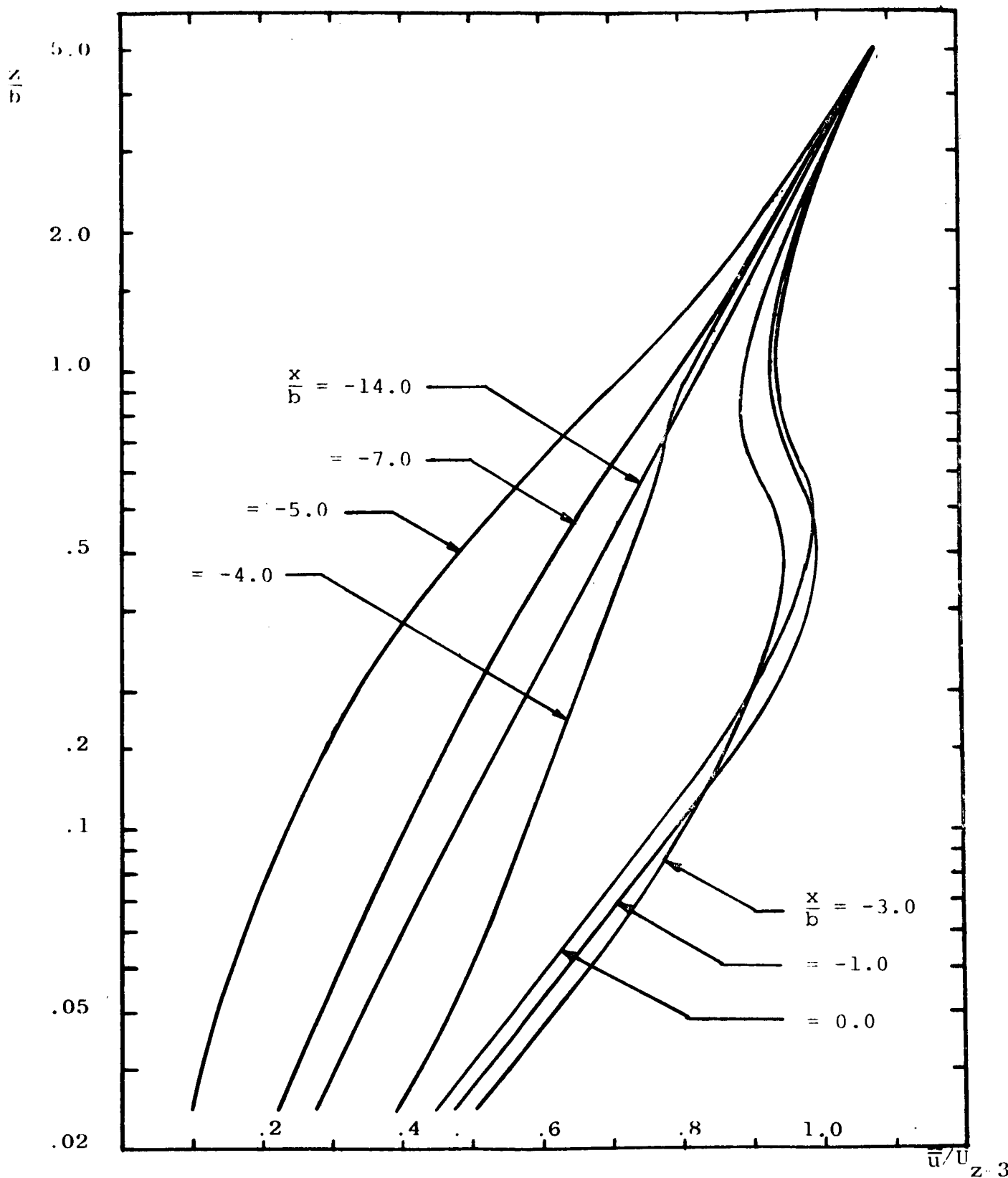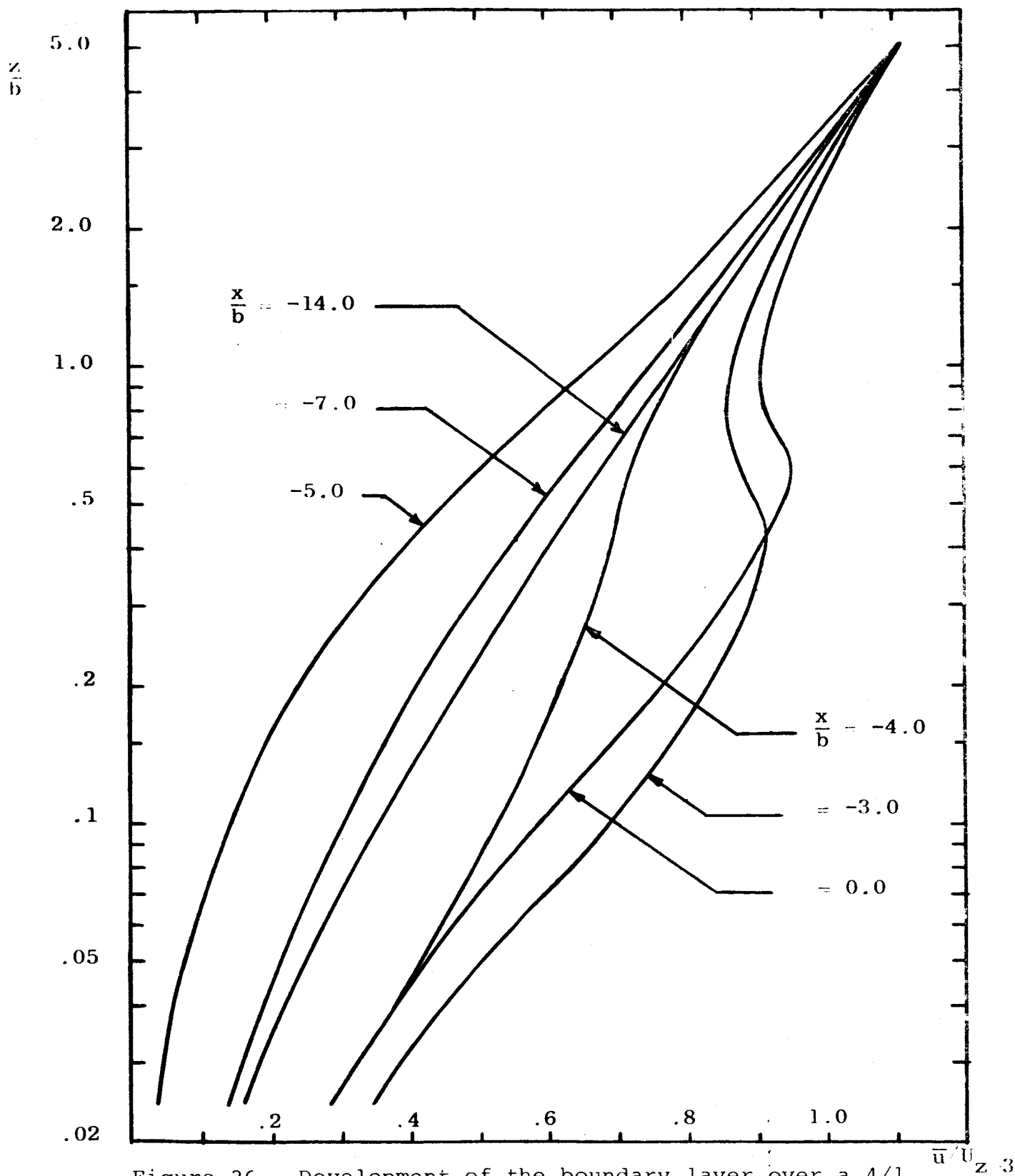90

Figure 26. Development of the boundary layer over a 4/1
ellipse with variable pressure gradient in the vertical
direction and logarithmic outer boundary condition for
z/b = 0.020.

91

Proceeding downstream, the adverse pressure increases, reaching a maximum at approximately x/b = -3.0, where the deceleration of the flow near the surface causes the velocity to significantly deviate from the logarithmic distribution extending the influence of the body to very large heights.

The results given in Figures 23 and 24, pages 87 and 88, and Figures 25 and 26 are, in general, consistent with the wind profiles given in qualitative discussions of flow over surface obstructions (2) and (4) and with some experimental measurements of boundary layers over fences (11) and (12), in that the velocity near the obstruction exceeds that of the undisturbed flow. Moreover, this result is predictable from the standpoint of the conservation of mass, which requires that the acceleration of the flow at the top of the body be a maximum close to the surface where the streamlines are the most severely compressed.

Therefore, based on the above considerations and intuitive reasoning about the distribution of the pressure disturbances above the body, it is believed that the method used in obtaining the results given in this section is a justifiable approach in approximating the flow fields over surface obstructions. However, additional experimental work is needed to further verify this concept and to more accurately determine the variation of the pressure field in the vertical direction.

Boundary Layer Effects Produced by Separation Regions

The improvements made in the boundary layer analysis
by simulating the effects of the separation regions with
stationary, inviscid vortices, discussed in Chapter II, have
been preliminarily investigated. The calculations, given in
Figures 27 and 28, have been carried out for flow over the
2/1 ellipse for several surface roughnesses with these
results compared to the solutions given in the preceding
chapter for flow over the same body without attached
vortices.

The effects of the simulated separation region on the
development of the boundary over the ellipse is illustrated
in Figure 24, page 88, by comparing the velocity profiles
calculated at different x-stations along the surface. The
influence of the vortices on the velocity is to increase the
thickness of the shear layer by decelerating the flow in the
boundary layer both upstream and downstream of the forward
separation region. For the calculation carried out over the
vortex, this same effect occurs in the upper portion of the
profile, but near the vortex, the additional momentum
imparted to the flow by the slip velocity, u_s, along the
dividing streamline increases the velocities in the lower
boundary layer. It is useful in examining the effect of the
separation regions on the flow to consider the potential
velocity field over the elliptical cylinder given in Figure
7, page 37. Comparing the distribution along the non-
separating streamlines ($\frac{\psi}{U_\infty b} = 0.60$) for the cases given with

93

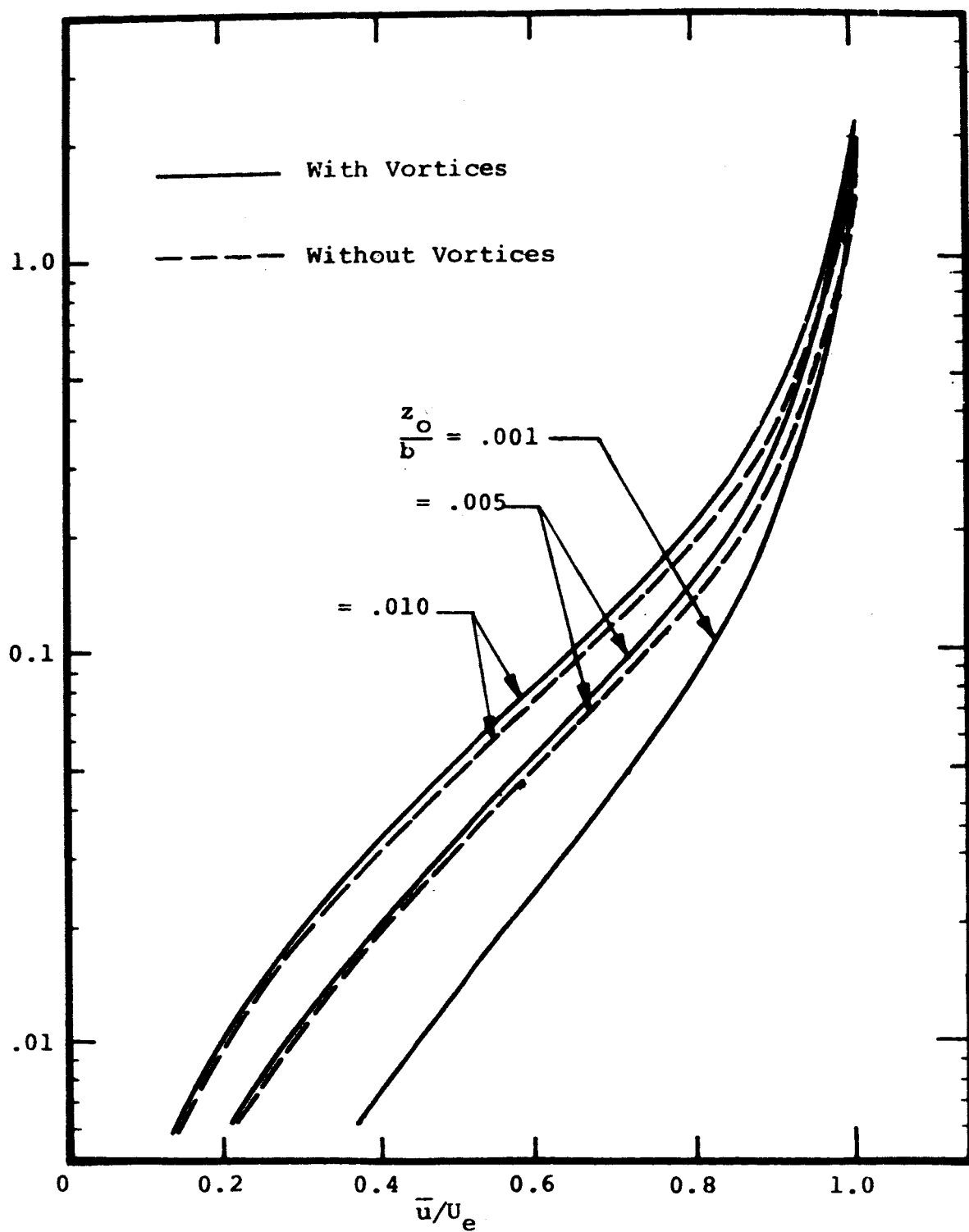Figure 27. Effect of vortices on development of velocity profiles over the 2/1 ellipse.

94
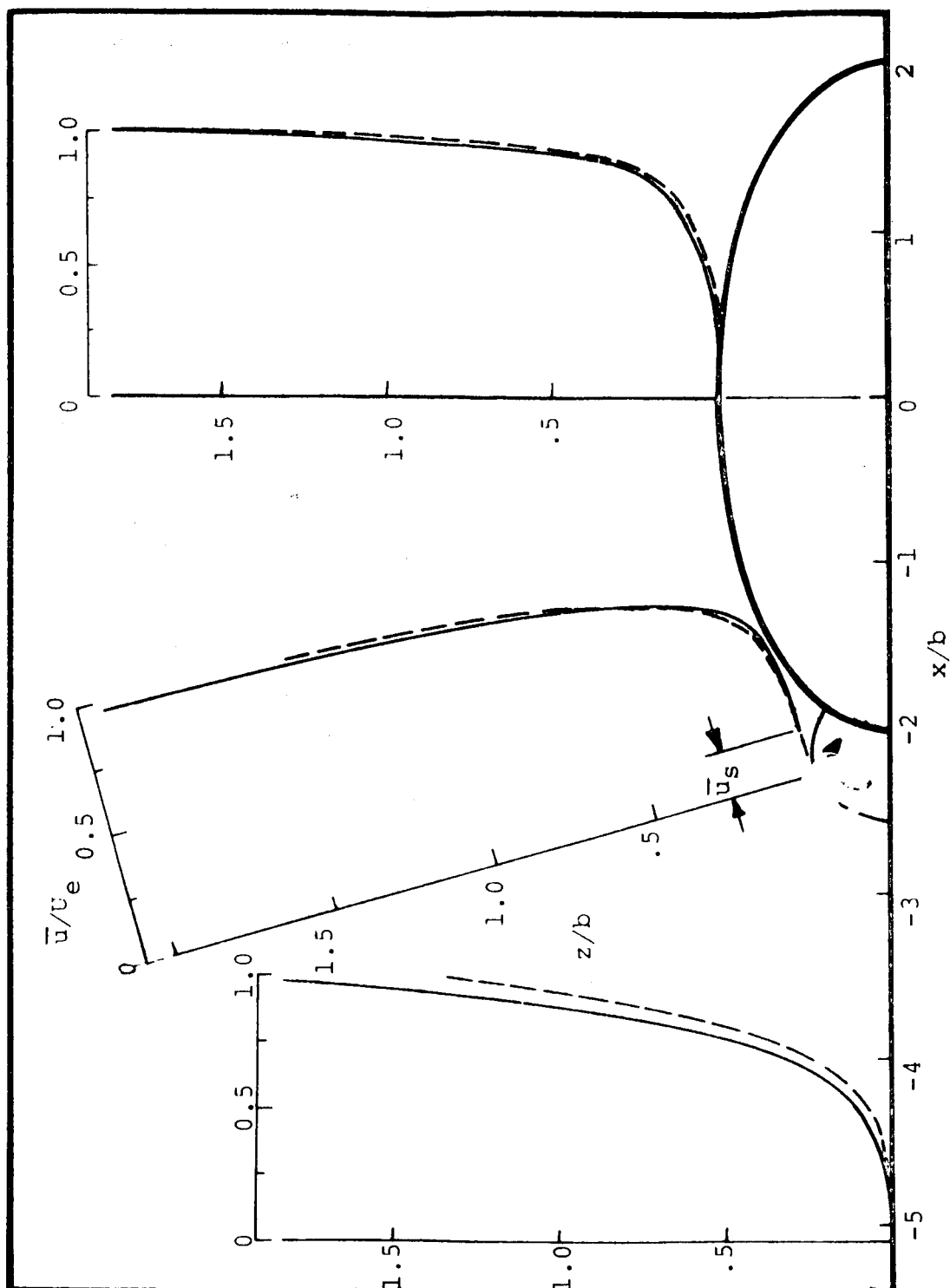
Figure 28. Effect of vortices on velocity profile at top of
    2/1 ellipse with different roughnesses.

and without the effects of the potential vortices, it can be observed that both upstream of the forward separation region and at the top of the ellipse, the vortex decreases the potential velocity. This effect can be interpreted through

the Bernoulli equation as an increase in the pressure gradient in these two regions of the flow. Since the pressure fields at these two positions are adverse, this fact leads to the conclusion that the velocity in the boundary layer will be less for calculations which include the influence of the separation regions. However, the velocity is affected to a greater extent upstream where the difference in the two potential solutions is greater than at the top of the ellipse.

This effect is further illustrated in Figure 28 for calculations made at the top of the obstruction, for different surface roughnesses, where the maximum decrease in velocity brought about by including the vortices in the potential solution, is only about two per cent. An additional observation from this figure is that the separation regions appear to have no effect on the difference in velocity brought about by changes in roughness, that is, the increase in velocity produced by the change roughness from z_o = .010 to .005 meters is very nearly the same as the solution obtained with the addition of the vortices.

From the above considerations it can be concluded that this method of simulating the additional effects of the separation regions with the inviscid vortices attacks the

most difficult area of the flow field to predict by boundary layer analysis and suggests that the effects of these regions on the overall flow field are small. In addition, steps have been taken to obtain a more realistic physical interpretation of the solutions over the separation bubble by including the slip velocity as a lower boundary condition on the equations.

It is believed that this initial attempt at incorporating the effect of the separated flow into the boundary layer approach will improve the approximation of the flow field near the separation regions, but preliminary investigation of this method indicates that further calculations and experimental work are needed to improve the assumptions made.

CHAPTER VI

DISCUSSION OF RESULTS RELATIVE TO

AERONAUTICAL APPLICATION

Winds and turbulence are significant factors influencing the safety, quality, and efficiency of air transportation. Loads due to extreme turbulence or unexpected gusts of wind can exceed the static strength of the aircraft or upset the handling qualities to the point where control is lost and accidents occur. The effects of moderate turbulence although generally not as catastrophic, can degrade the precision of flight and tax the fatigue strength of the structure.

Donely (31) reports that approximately 80 per cent of rough air experience occurs at altitudes below 25,000 ft. and is consequently prevalent to short haul or feeder line aircraft and to long haul aircraft during climb and descent. In the terminal areas where precision flight is most critical the air motion is frequently more severe due to wind disturbances from buildings and topological surface features.

The wind gradient or shear can either add or absorb energy from an ascending or descending aircraft. Since the aircraft is essentially a constant speed machine, a gradient wind can thus increase or decrease the rate of descent and the angle of descent as well as the margin for the stall safety. These problems tend to increase as the landing

speed decreases, and for V/STOL vehicles, the angular variation with altitude can be a significant factor in complicating the pilot's task of controlling the aircraft.

Automatic landing systems are also susceptable to the effects of turbulence. McManus (32) reports on early experience with the Trident automatic landing system: "When the Trident was first landed automatically in moderate turbulence, several instances of poor performance occurred. These were caused by significant single horizontal gusts." "These gusts were not predicted by the general turbulence models as they were special to the site." In one case, a moderate crosswind was blowing over a factory into the under-shoot area. Close inspection showed a long hanger with a double apex roof at approximately 45 degrees to the wind, directly in line with the undershoot area. This generates a stable wind pattern which a single stationary measuring station would not record as high turbulence, but an aircraft passing through the pattern would be subject to large air-speed variations.

The problems of an aircraft flying through a head wind that varies with elevation has been investigated in a paper by Etkin (33). The equations of motion were set up and solved for a flight at constant air speed. The effect of this wind gradient on the flight path during descent and climb is shown. It is seen that the deviation from the case with no wind gradient is quite considerable.

In the case of descending from a given height into a

positive wind gradient (increasing wind with height), an airplane overshoots the initial tangent by a distance s, as shown in Figure 29. For a linear wind variation, this distance is given as:

$$s = \frac{1}{2} \frac{\partial w}{\partial z} V_A t^2 \sin \phi$$

where

$\frac{\partial w}{\partial z}$ = head wind gradient

V_A = Airplane Air Speed

t = time

ϕ = path angle

The problem of the climbing aircraft differs from the glide in that the angle ϕ is negative and that there is an additional force, the thrust. The path is a parabolic as before, the convexity in the same sense, so that the horizontal distance to reach a given height is concentrated as compared with the case of zero wind gradient; see Figure 29. The effect of a negative wind gradient (decreasing wind with height) on glide and climb is shown in Figure 29.

Another effect arises, when the wind gradient is not coming directly from ahead, but is blowing at a certain angle β to the flight direction. It is shown in Figure 30 that a cross wind induces a lift addition on one side and a lift subtraction on the other side of the wing, thus producing a roll-moment. As w(z) or w sin β is a function of

100

Positive Wind Gradient

Negative Wind Gradient

Y_I

Over Shoot

s

s
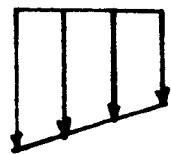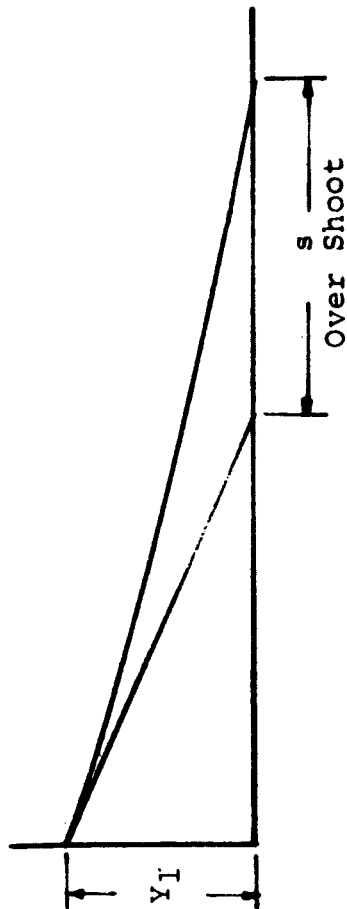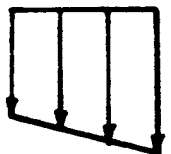
(a) Effect on Glide or Descent
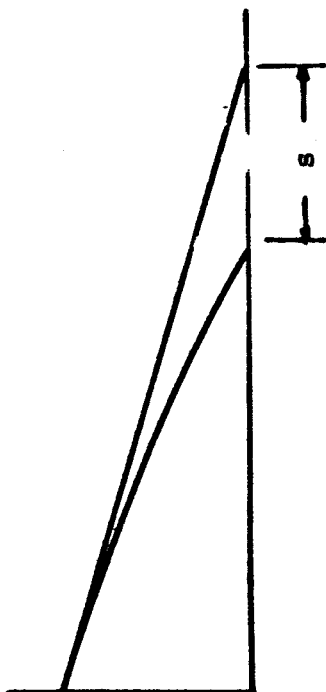
(c) Effect on Glide or Descent

h

h

(b) Effect on Climb

(d) Effect on Climb

Figure 29. Effect of wind gradient on climb and descent.

101

Vertical Wind w(z) β
Gradient

Upward
Component
    w sin β

Downward
Component
w sin β

$+\Delta F$

$-\Delta F$
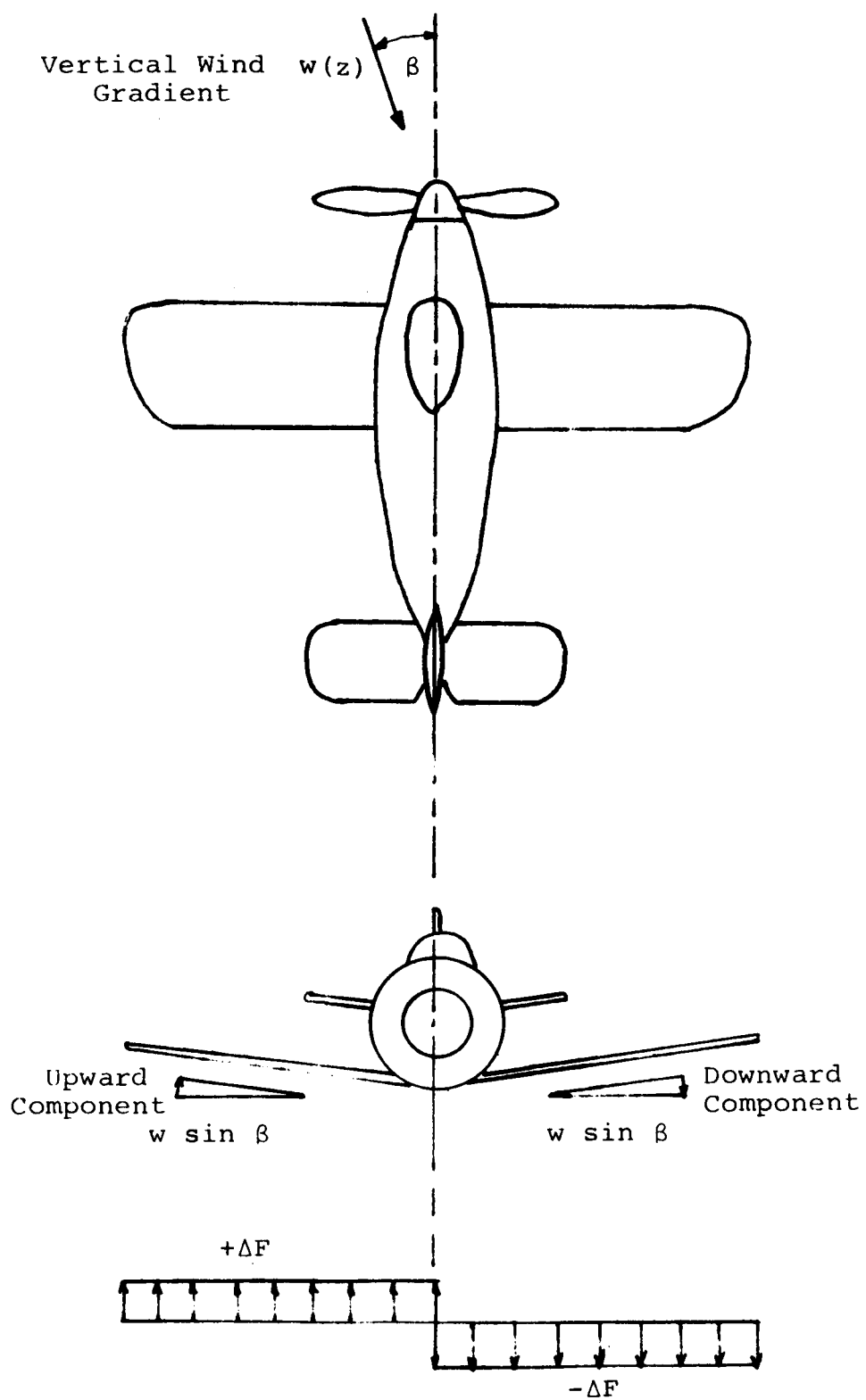
Figure 30. Roll moment induced by cross wind.

elevation, the roll-moment will also vary with height according to w(z). For strong gradients of w(z), correspondingly strong gradients in the roll-moment must be expected.

An approximate quantitative estimate of the influence of gusts occurring due to the presence of buildings is possible from the results of this study shown in Figures 23 through 26, pages 87, 88, 90, and 91. These figures show relatively large wind acceleration or gusts near the top of semi-elliptical surface protrusions. Taking the lift as a typical example, the following analysis for a 2:1 ellipse with the velocity profile shown in Figure 23 provides a quantitative feel for these effects.

Lift is given by the expression:

$$L = C_L \frac{\rho_\infty V^2 \ell}{2}$$

The ratio of the lift in the disturbance of the building, L_B, to that in the natural wind, L_N, all other parameters being constant, is:

$$\frac{L_B}{L_N} = \left(\frac{V_B + V_A}{V_N + V_A} \right)^2$$

A plot of the ratio L_B/L_N versus elevation at the x/b = 0 station for the 2:1 ellipse with z_o/b = 0.005 assuming $V_A/U_{(z=3)}$ = 1.0 is shown in Figure 31. The plot indicates that an aircraft flying into the wind over a long building

Figure 31. Vertical distribution of the ratio of lift over ellipse to lift in natural wind.

104

or surface obstruction of semi-elliptical configuration would experience an increase in lift exceeding 20 per cent of the value for wind over unifo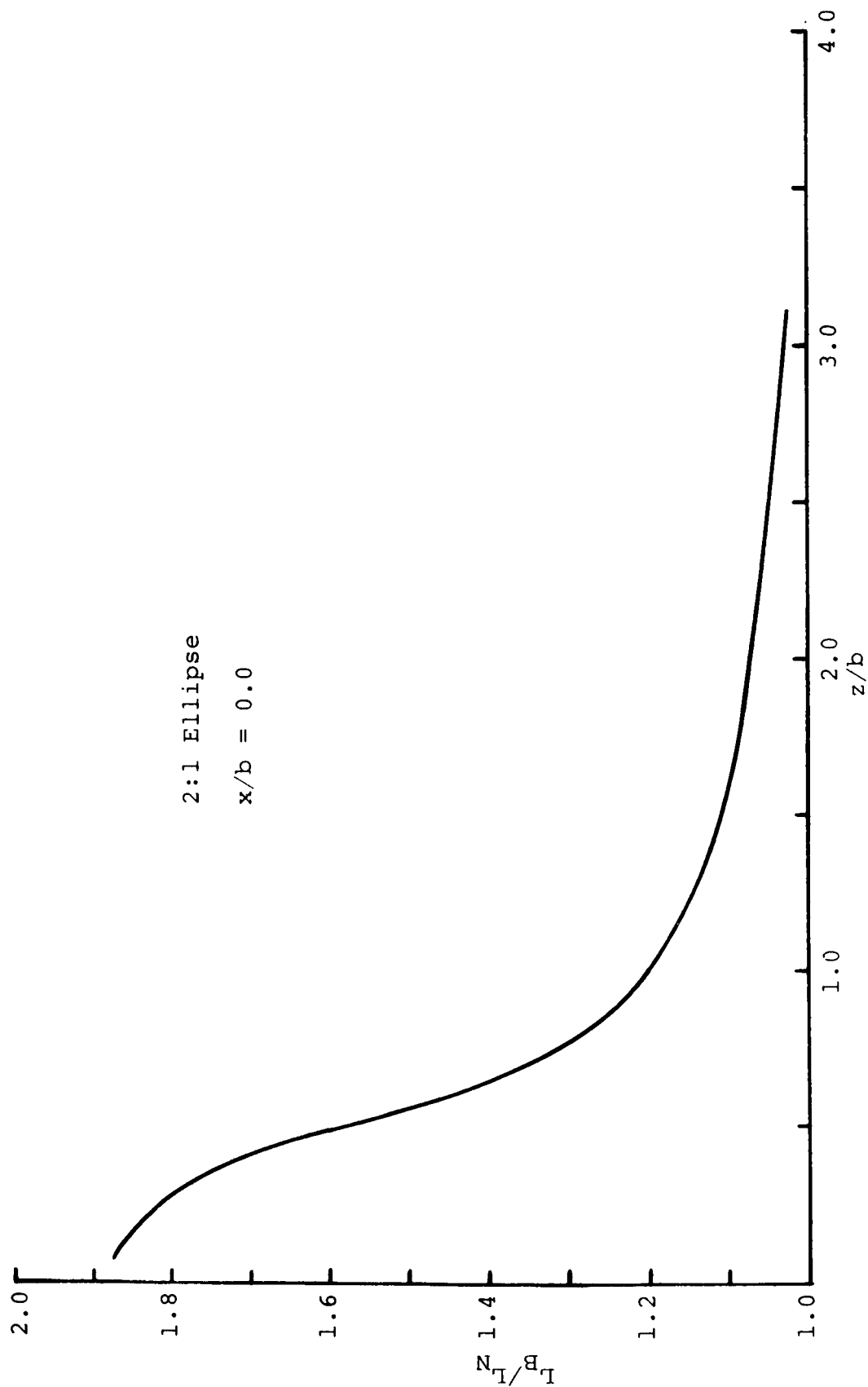rm terrain if passing below a distance equal to the obstruction height $z/b = 1.0$, (i.e., 40 feet above the ground for a 20 foot obstruction).

Figure 32 shows the variation in lift ratio L_B/L_N with longitudinal position from the top of the ellipse to a dimensionless distance $x/b = -10$ upstream of the approaching wind where the wind is logarithmic. Parametric variation with z/b is given in the curve.

An aircraft passing over the obstruction at a fixed height of $z/b = 1.0$ would experience an initial increase in lift of 20 per cent which would diminish and change to a 10 per cent decrease at $x/b = -3.0$. Thus, a simple 15 foot high quansit hut located on the order of 600 feet from the end of a landing strip can generate a 30 per cent variation in lift in a distance less than 150 feet. The pilot's correction time at 50 mph landing speed is on the order of two seconds illustrating the hazards of unexpected wind profiles due to surface projection.

It is apparent from the previous discussion that a model for predicting wind velocity profiles about surface obstructions is important to the design of airplane control systems and to the design of airports themselves. The wind model presented in this report is a step in that direction since it provides transportation designers with insight to:

1. Determining the safest distance for structures

105
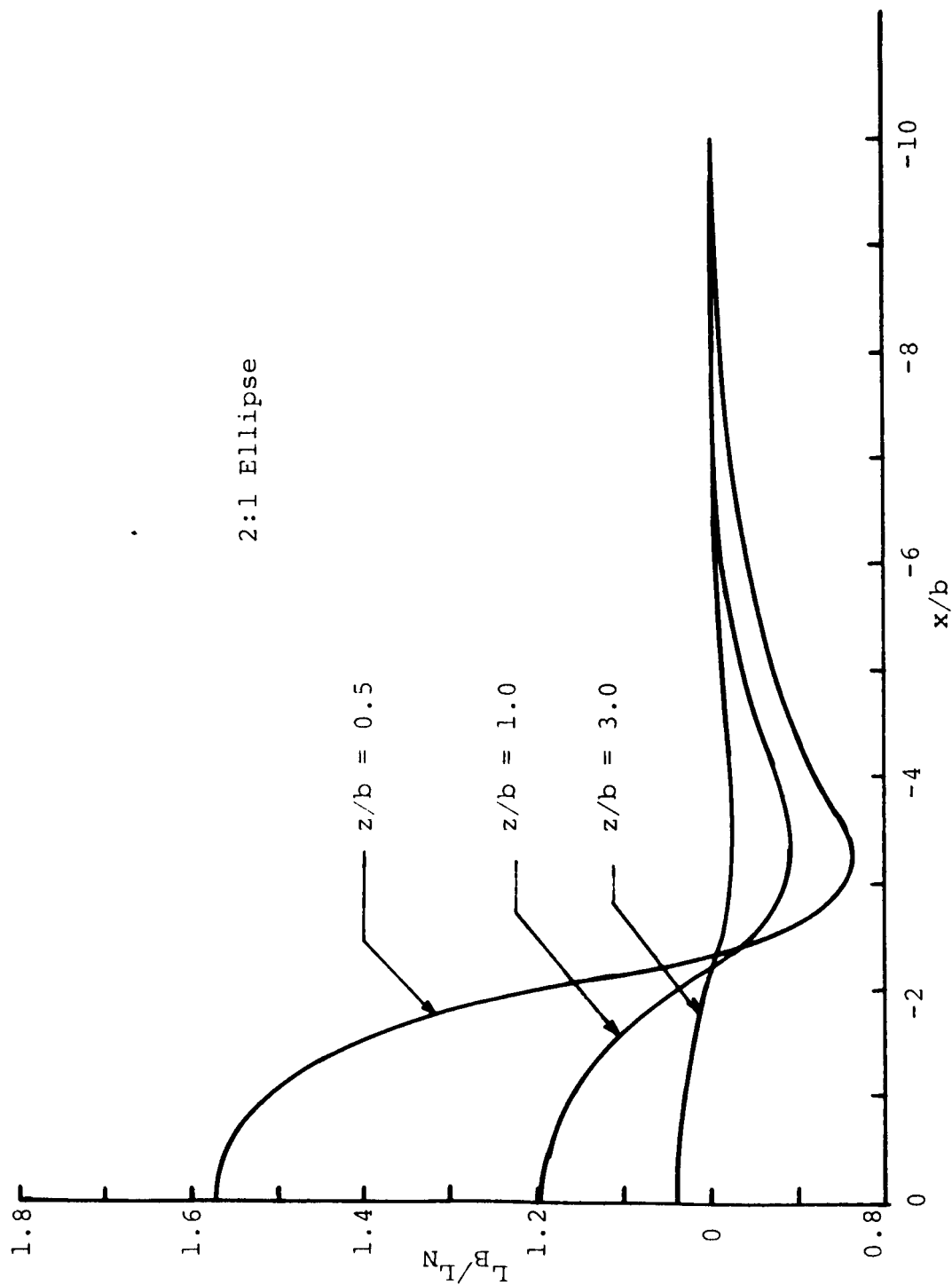
Figure 32. Horizontal variation of the ratio of lift over ellipse to lift
in natural wind.

from landing strips, at least, from the windward side. This is of particular significance to V/STOL ports in urban areas.

2. Analyzing existing airports to warn of possible unexpected wind patterns and to define optimum locations of measuring stations to detect these wind patterns.

3. Improving mathematical gust models employed in automatic landing systems. Present gust model generally assumed a power law variation of the mean wind, for example Skelton (34) uses:

$$U(z) = U(z_1)(z/z_1)^{P(z_0)}$$

A mathematical description for the flow patterns induced by surface obstruction is required to make these gust models more reliable.

The use of the present boundary layer analysis of wind profiles is of course limited to a two-dimensional elliptical geometry and subject to the assumptions regarding eddy viscosity and pressure gradient decay. Moreover, the numerical nature of the solutions make them difficult to incorporate into mathematical gust models and into computation of airplane characteristics.

In view of the promising applications the flow analysis over obstructions has, however, it is believed that additional effort to expand and improve the model is definitely desirable. The model should be:

1. Extended to other geometries,

2. Investigated using other eddy viscosity

correlations, for example, conservation of turbulence kinetic energy,

  3. Employed with other hypothesis regarding the pressure gradient surrounding the surface obstruction, and

  4. Compared to wind profile data from a simple experiment over an elliptical configuration.

CHAPTER VII

CONCLUSIONS AND SUMMARY

The boundary layer approach presented in this investigation provides a reasonable first order approximation of the atmospheric flow field which exists around buildings and other surface obstructions. This method has been applied to flow over elliptical cylinders, and, despite the lack of experimental data in this area, certain conclusions can be drawn about the relationship of the parameters involved in this problem.

1. An increase in the elliptical aspect ratio decreases the wind speed within the boundary layer at the top of the ellipse and returns it to the logarithmic distribution characteristic of undisturbed flow.

2. Increases in surface roughness affect the flow by decreasing the velocity in the boundary layer, with the most pronounced effect occurring near the surface of the smaller aspect ratio ellipse.

3. The initial friction velocity which enters the boundary layer equations through the Reynolds' number has a negligible effect on the overall flow for the range of Reynolds' numbers considered in this study.

4. A decrease in the elliptical aspect ratio and an
   increase in the surface roughness cause larger
   separation regions.

5. The decay of the streamwise pressure gradient in
   the vertical direction produces localized maxi-
   mums in wind speed at the top of a surface
   obstruction, which are expected in physically
   real flow situations.

6. The preliminary investigation of the simulation
   of separation regions with inviscid vortices
   indicates that this method appears to have only a
   small effect on the overall flow but does improve
   the approximation of the flow field near the
   stagnation regions.

In summary, the method developed in this study
utilizes the simplifying assumptions of boundary layer
theory in an effort to analyze the complex flow field which
exists in atmospheric motions over surface obstructions. It
has been shown that reasonable approximations of the physi-
cal conditions which exist in the atmospheric flow near the
ground can be made without sacrificing the simplicity and
savings in time and money realized with a boundary layer
solution as opposed to a solution of the complete equations
of motion. Finally, it is believed that, with additional
experimental and analytical work to verify some of the
proposed assumptions, flow fields over surface obstructions
can be predicted with sufficient accuracy to make the

boundary layer approach a valuable tool in the analysis of atmospheric shear flows.

BIBLIOGRAPHY

BIBLIOGRAPHY

1. Parker, H. M., J. N. Blanton, and K. J. Grunwald. "Some Aspects of the Aerodynamics of STOL Ports." Paper presented at NASA Conference on Aircraft Safety and Operational Problems, Hampton, Virginia, May, 1971.

2. Hunt, J. C. R. "The Effect of Single Buildings and Structures," Philosophical Transactions of the Royal Society of London, 269A:457-467, June, 1971.

3. Wise, A. F. E. "Effects Due to Groups of Buildings," Philosophical Transactions of the Royal Society of London, 269A:468-485, June, 1971.

4. Halitsky, J. "Gas Diffusion Near Buildings," Meteorology and Atomic Energy, D. H. Slade, editor. Silver Springs, Maryland: United States Atomic Energy Commission, 1968. Pp. 221-255.

5. Deardoff, J. W. "A Three Dimensional Numerical Investigation of the Idealized Planetary Boundary Layer," Geophysical Fluid Dynamics, 1:377-410, November, 1970.

6. Hotchkiss, R. S. "The Numerical Calculation of Three Dimensional Flows of Air and Particulates about Structures." Paper presented at the Symposium on Air Pollution, Turbulence and Diffusion, Albuquerque, New Mexico, December, 1971.

7. Lantz, R. B., and K. H. Coats. "A Three Dimensional Numerical Model for Calculating the Spread and Dilution of Air Pollutants." Paper presented at the Symposium on Air Pollution, Turbulence and Diffusion, Albuquerque, New Mexico, December, 1971.

8. Blackadar, A. K., et al. "Determination of the Effect of Roughness Change on the Wind Profile." Paper presented at the Symposium on Boundary Layers and Turbulence, Kyoto, Japan, September 19-24, 1966.

9. Blom, J., and L. Wartena. "The Influence of Changes in Roughness on the Development of the Turbulent Boundary Layer in the Lower Layers of the Atmosphere," Journal of Atmospheric Science, 26:255-265, July, 1969.

10. Bradley, E. F. "A Micrometeorological Study of the Velocity Profiles and Surface Drag in a Region Modified by a Change in Surface Roughness," Quarterly Journal of the Royal Meteorological Society, 94:361-379, 1968.

11. Arie, M., and H. Rouse. "Experiments on Two-Dimensional Flow over a Normal Wall," Journal of Fluid Mechanics, 1:24-141, November, 1956.

12. Good, M. C., and P. C. Joubert. "The Form Drag of Two-Dimensional Bluff-Plates Immersed in Turbulent Boundary Layers," Journal of Fluid Mechanics, 31:547-582, June, 1968.

13. Plate, E. J. Aerodynamic Characteristics of Atmospheric Boundary Layers. United States Atomic Energy Commission. Oak Ridge, Tennessee: Division of Technical Information Extension, 1971.

14. Schlichting, H. Boundary Layer Theory. New York: McGraw-Hill Book Company, Inc., 1968.

15. Tverskoi, P. N. Physics of the Atmosphere. United States Department of Commerce. Springfield Virginia: Clearinghouse for Federal Scientific and Technical Information, 1965.

16. Lumley, J. L., and H. A. Panofsky. The Structure of Atmospheric Turbulence. New York: Interscience Publishers, 1964.

17. Van Driest, J. R. "On the Turbulent Flow Near a Wall," Journal of Aeronautical Science, 23:1007-1017, November, 1956.

18. Cebeci, T., and A. M. O. Smith. "A Finite-Difference Solution of the Incompressible Turbulent Boundary Layer Equations by an Eddy-Viscosity Concept." Paper presented at AFOSR-IFP-Stanford Conference on the Computation of Turbulent Boundary Layers, Stanford, California, August 18-25, 1968.

19. Clauser, F. H. "The Turbulent Boundary Layer," Advances in Applied Mechanics. New York: Academic Press, 1956. Pp. 2051-2079.

20. Klebanoff, P. S. "Characteristics of Turbulence in a Boundary Layer with Zero Pressure Gradient," National Advisory Committee for Aeronautics TN 3178, Washington, D.C., July, 1954.

21. Nee, V. W., and L. S. G. Kovasznay. "Simple
        Phenomenological Theory of Turbulent Shear Flows,"
        The Physics of Fluids, 12:473-482, March, 1969.

22. Mayne, A. W., and J. C. Adams, Jr. "Streamline
        Swallowing by Laminar Boundary Layers in Hypersonic
        Flow," Arnold Engineering Development Center
        TR-71-32, Arnold Air Force Station, Tennessee,
        April, 1971.

23. Milne-Thomson, L. M. Theoretical Hydrodynamics. New
        York: The Macmillan Company, 1960.

24. Smith, G. D. Numerical Solution of Partial Differential
        Equations. New York: Oxford University Press,
        1965.

25. Wieghardt, K., and W. Tillmann. "On the Turbulent
        Friction Layer for Rising Pressure," National
        Advisory Committee for Aeronautics TM 1314,
        Washington, D.C., March, 1951.

26. Streeter, V. L. Fluid Dynamics. New York: McGraw-
        Hill Book Company, 1948.

27. Longley, R. W. Elements of Meteorology. New York:
        John Wiley and Sons, Inc., 1970.

28. Cole, F. W. Introduction to Meteorology. New York:
        John Wiley and Sons, Inc., 1970.

29. Blackadar, A. K. "The Vertical Distribution of Wind
        and Turbulent Exchange in a Neutral Atmosphere,"
        Journal of Geophysical Research, 67:3095-3102,
        April, 1962.

30. Lettau, H. H. "Wind Profile, Shear Stress and
        Geostrophic Drag Coefficients in the Atmospheric
        Surface Layer," Advances in Geophysics. New York:
        Academic Press, 1962. Pp. 241-257.

31. Donely, P. "Atmospheric Turbulence and the Air Trans-
        portation System," RAS International Conference on
        Atmospheric Turbulence, May, 1971.

32. McManus, R. M. P. "Development of an Approach and
        Landing System with Special Reference to the
        Effects of Turbulence," Ibid, Session IV, B.20.

33. Etkin, Bernard. "Effect of Wind Gradient on Glide and Climb," Journal of the Aeronautical Sciences, 14: No. 6, 365-367, November, 1947.

34. Skelton, G. B. "Gust Effects on V/STOL Aircraft," RAS International Conference on Atmospheric Turbulence, May 1971, Session IV, B22.

APPENDIXES

APPENDIX A

UNIFORM POTENTIAL FLOW PAST AN

ELLIPTICAL CYLINDER

The potential flow field around a two-dimensional elliptical cylinder can be obtained from the theory of complex variables. Consider a uniform, irrotational flow of an incompressible, inviscid fluid in the complex Z plane parallel to the X-axis with a velocity U. Defining the complex potential, w, as

$$w(Z) = \phi(X,Y) + i\psi(X,Y)$$

where $Z = X + iY$, the velocity field can be obtained by differentiating the potential with respect to a coordinate direction,

$$\frac{\partial w}{\partial X} = \frac{\partial \phi}{\partial X} + i\frac{\partial \psi}{\partial X} = \frac{dw}{dZ}\frac{\partial Z}{\partial X} = \frac{dw}{dZ}$$

Defining the complex velocity as the negative of this differential,

$$\nu = -\frac{dw}{dZ} = -\frac{\partial \phi}{\partial X} - i\frac{\partial \psi}{\partial X} = u - iv$$

where u and v are the velocities in the X and Y directions, respectively. For the case of uniform flow parallel to the X-axis,

118

$$v = U = -\frac{dw}{dZ}$$

or

$$w(Z) = -UZ$$

Consider a circular cylinder of radius R placed in an arbitrary flow field of complex potential $f(Z)$. From the circle theorem of Milne-Thomson (23), the complex potential of the flow around the cylinder becomes

$$w(Z) = f(Z) + \overline{f}\left(\frac{R^2}{Z}\right)$$

where $\overline{f}$ is the complex conjugate of f. For a circular cylinder in a uniform flow field, the complex potential is

$$w(Z) = U\left(Z + \frac{R^2}{Z}\right) \tag{36}$$

To transfer the region of flow in the Z plane outside the circular cylinder into a region outside an elliptical cylinder in the z plane, as shown in Figure A1, the Joukowski transformation (23) should be applied to the above equation. This transformation has the following form,
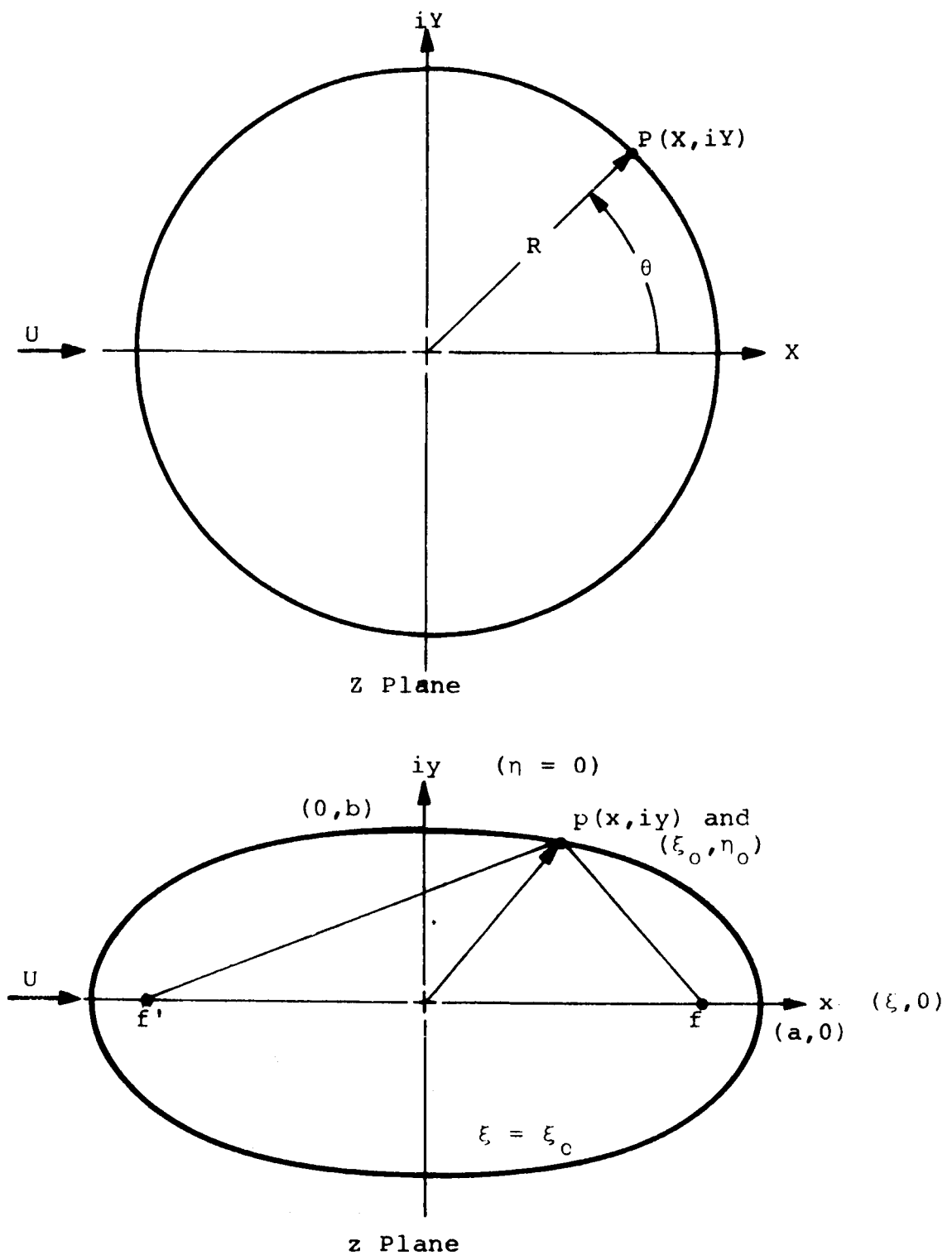
$$z = Z + \frac{c^2}{4Z}$$

where

119

Figure A1. Geometry for Joukowski transformation of flow over a circular cylinder to flow over an elliptical cylinder.

120

$$c^2 = a^2 - b^2$$

$$R = \frac{1}{2}(a + b)$$

Solving for the inverse transformation,

$$Z = \frac{1}{2}(z \pm \sqrt{z^2 - c^2}) \tag{37}$$

and applying to Equation 36, the flow field over the circular cylinder of radius R = (a + b)/2 is transformed into flow over an elliptical cylinder of major axis 2a aligned parallel to the x-axis and minor axis 2b aligned with the y-axis, as illustrated in Figure A1.

Using the positive root of Equation 37, the complex potential in the z plane becomes

$$w(z) = \frac{1}{2} U \left[(z + \sqrt{z^2 - c^2}) + \frac{(a + b)^2}{z + \sqrt{z^2 - c^2}} \right]$$

$$w(z) = \frac{1}{2} U(a + b) \left[\frac{z + \sqrt{z^2 - c^2}}{a + b} + \frac{z - \sqrt{z^2 - c^2}}{a - b} \right] \tag{38}$$

Defining an orthogonal, elliptical coordinate system, (ξ, η), the z plane can be transformed into a more useful form. This coordinate transformation from the (x,y) variables in the z plane to (ξ, η) in the elliptic plane is defined by

$$z = x + iy = c \cosh(\xi + i\eta)$$

or

121

$$z = c[\cosh \xi \cos \eta + \sinh \xi \sin \eta] \tag{39}$$

where the lines of constant ξ are cofocal ellipses with major axis parallel to the x-axis, and lines of constant η are orthogonal hyperbolas. In Figure A1, page 106, the line $\xi = \xi_0$ defines an ellipse with major axis of length $2 \cdot a$ and minor axis of length $2 \cdot b$. From Equation 39

$$x = c \cosh \xi \cos \eta \tag{40}$$

$$y = c \sinh \xi \sin \eta \tag{41}$$

therefore

$$a = c \cosh \xi_0 = \sqrt{a^2 - b^2} \cosh \xi_0 \tag{42}$$

$$b = c \sinh \xi_0 = \sqrt{a^2 - b^2} \sinh \xi_0 \tag{43}$$

From the definition of the hyperbolic functions, Equations 42 and 43 can be combined as

$$a + b = c(\cosh \xi_0 + \sinh \xi_0) = ce^{\xi_0} \tag{44}$$

$$a - b = c(\cosh \xi_0 - \sinh \xi_0) = ce^{-\xi_0} \tag{45}$$

Introducing Equations 39, 44, 45 and the hyperbolic identities into Equation 38, the complex potential for flow over an elliptical cylinder becomes

$$w(z) = \frac{1}{2}U(a + b)\left[\frac{c \cosh(\xi+i\eta) + \sqrt{c^2\cosh^2(\xi+i\eta) - c^2}}{ce^{\xi_0}} \right.$$
$$\left. + \frac{c \cosh(\xi+i\eta) - \sqrt{c^2\cosh^2(\xi+i\eta) - c^2}}{ce^{-\xi_0}} \right]$$

122

$$= U(a + b) \left[\frac{\exp(\xi + i\eta - \xi_0) + \exp(-\xi - i\eta - \xi_0)}{2} \right]$$

$$w(z) = U(a + b) \cosh(\xi + i\eta - \xi_0)$$

$$w(z) = \phi + i\psi = U(a + b) \cosh[(\xi - \xi_0) + i\eta] \qquad (46)$$

Expanding and equating the real and imaginary parts, the stream function will be defined as

$$\psi = U(a + b) \sinh(\xi - \xi_0) \sin \eta$$

$$\psi = U(a + b) [\sinh \xi \cosh \xi_0 - \cosh \xi \sinh \xi_0] \sin \eta \qquad (47)$$

Using Equations 42 and 43 and expanding $\cosh \xi_0$ as an exponential and hyperbolic sine term, the following relation is obtained for the stream function:

$$\psi = -Ub \sqrt{\frac{a + b}{a - b}} e^{-\xi} \sin \eta + U \sqrt{a^2 - b^2} \sinh \xi \sin \eta \qquad (48)$$

Nondimensionalizing this equation by U and b and defining an ellipse aspect ratio $k = a/b$, the stream function becomes

$$\frac{\psi}{Ub} = \sqrt{\frac{k + 1}{k - 1}} e^{-\xi} \sin \eta + (k^2 - 1) \sinh \xi \sin \eta \qquad (49)$$

This relationship defines the streamlines for uniform potential flow over an elliptical cylinder.

The velocity potential function, ϕ, is similarly derived and is given by the following equation:

$$\frac{\phi}{Ub} = \frac{k+1}{k-1} e^{-\xi} \cos \eta + k^2 - 1 \cosh \xi \cos \eta \qquad (50)$$

Since the velocity in any direction, s, is given by $-\frac{\partial \phi}{\partial s}$, the potential velocity can be obtained by differentiating Equation 50 with respect to the direction of the streamline. However, it is more convenient to calculate the velocity along the streamline in terms of the orthogonal elliptic coordinates (ξ, η).

Consider an incremental distance, ds, along the streamline as shown in Figure A2 in terms of the Cartesian coordinates (x, y).

$$(ds)^2 = (dx)^2 + (dy)^2 \qquad (51)$$

Since under the elliptic transformation,

$$x = x(\xi, \eta)$$
$$y = y(\xi, \eta)$$

Equation 51 becomes

$$(ds)^2 = \left(\frac{\partial x}{\partial \xi} d\xi + \frac{\partial x}{\partial \eta} d\eta \right)^2 + \left(\frac{\partial y}{\partial \xi} d\xi + \frac{\partial y}{\partial \eta} d\eta \right)^2$$

or

$$(ds)^2 = E(d\xi)^2 + F d\xi d\eta + G(d\eta)^2 \qquad (52)$$

where E, F and G are scaling factors defined by

$$E = \left(\frac{\partial x}{\partial \xi} \right)^2 + \left(\frac{\partial y}{\partial \xi} \right)^2 \qquad (53)$$
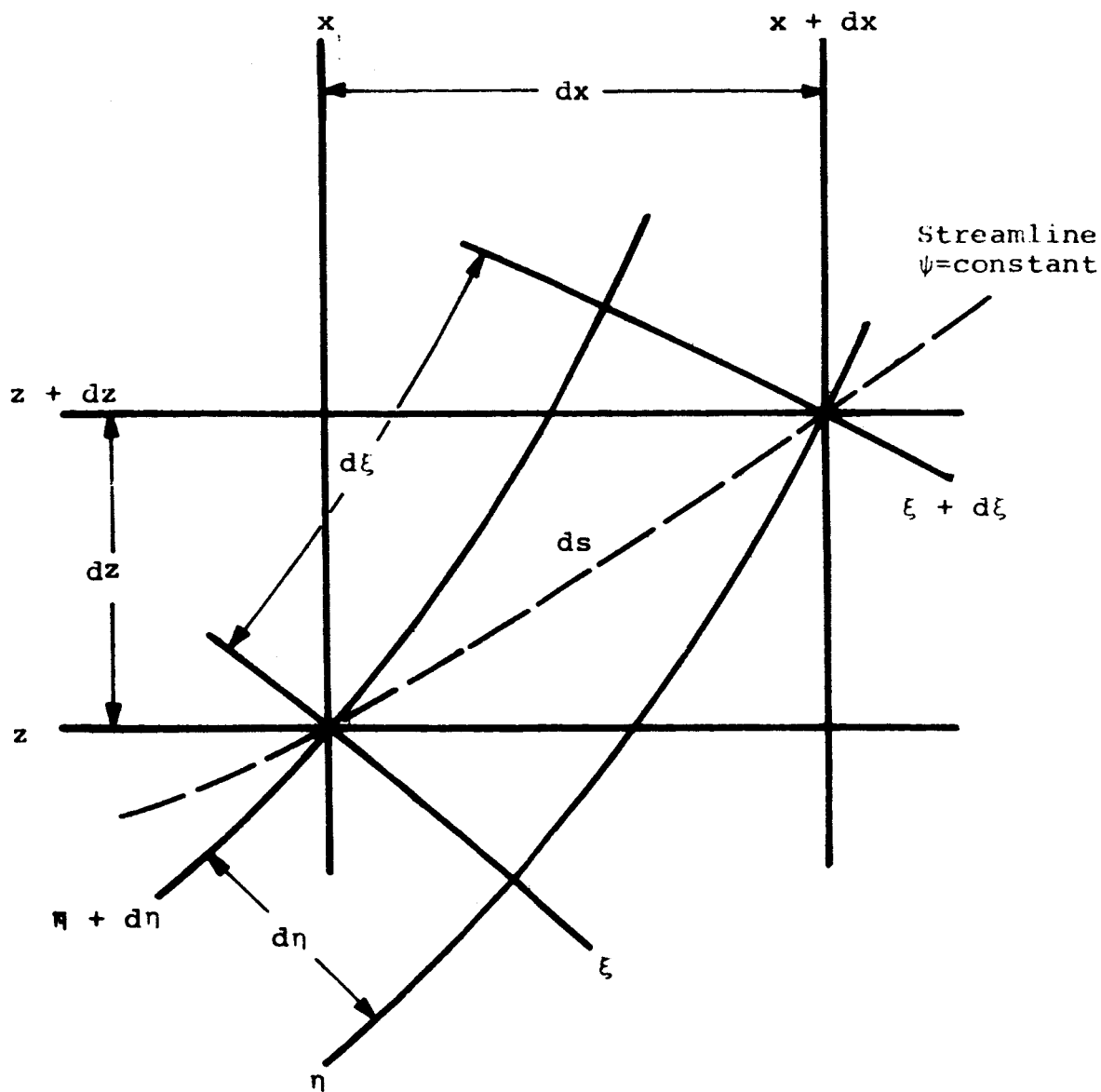
124

Figure A2. The relationship of differential distances in Cartesian and elliptic coordinates.

$$F = \frac{\partial x}{\partial \xi} \frac{\partial x}{\partial \eta} + \frac{\partial y}{\partial \xi} \frac{\partial y}{\partial \eta} \tag{54}$$

$$G = \left(\frac{\partial x}{\partial \eta}\right)^2 + \left(\frac{\partial y}{\partial \eta}\right)^2 \tag{55}$$

For an orthogonal system, $F = 0$; therefore,

$$(ds)^2 = E(d\xi)^2 + G(d\eta)^2$$

Along a curve, $\eta = \eta_o$, $d\eta = 0$.

$$ds = \sqrt{E} \, d\xi \qquad (\eta = \eta_o)$$

Similarly, along $\xi = \xi_o$, $d\xi = 0$

$$ds = \sqrt{G} \, d\eta \qquad (\xi = \xi_o)$$

For conformal transformations, the scaling at any point must be the same in all directions, consequently,

$$\sqrt{E} = \sqrt{G}$$

and

$$\left.\frac{\partial}{\partial s}\right)_{\xi=\xi_o} = \frac{1}{\sqrt{E}} \left.\frac{\partial}{\partial \eta}\right)_{\xi=\xi_o} \tag{56}$$

$$\left.\frac{\partial}{\partial s}\right)_{\eta=\eta_o} = \frac{1}{\sqrt{E}} \left.\frac{\partial}{\partial \xi}\right)_{\eta=\eta_o} \tag{57}$$

From Equations 56 and 57 the velocity components in the positive ξ and η directions as shown in Figure A3 are given by
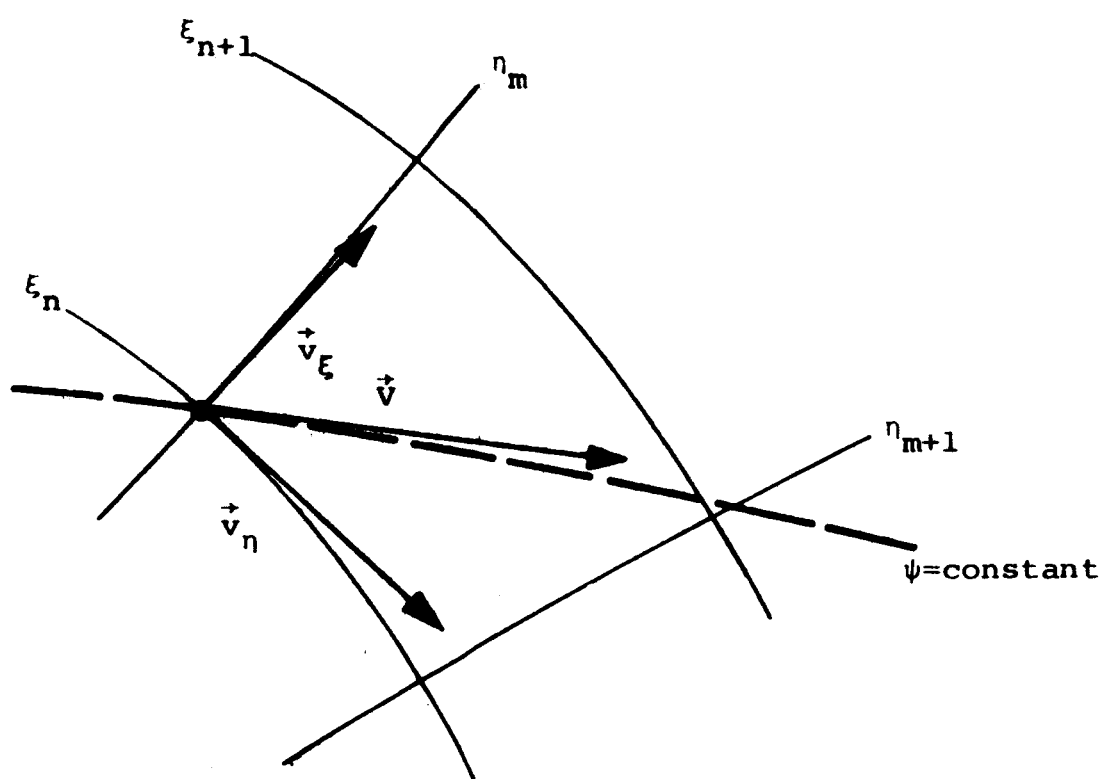
126

Figure A3. Potential velocity components in elliptical
      coordinates.

$$u_\xi = -\frac{\partial\phi(\xi,\eta)}{\sqrt{E}\ \partial\xi} \tag{58}$$

$$u_\eta = -\frac{1}{\sqrt{E}}\frac{\partial\phi(\xi,\eta)}{\partial\eta} \tag{59}$$

From Equations 50 and 53, these equations become

$$\frac{u_\xi}{U} = \frac{1}{\sqrt{\sinh^2\xi\ \cos^2\eta + \cosh^2\xi\ \sin^2\eta}}\left(\sqrt{\frac{k+1}{k-1}}\ e^{-\xi}\ \cos\eta \right.$$

$$\left. + \sqrt{k^2-1}\ \sinh\xi\ \cos\eta\right) \tag{60}$$

$$\frac{u_\eta}{U} = \frac{1}{\sqrt{\sinh^2\xi\ \cos^2\eta + \cosh^2\xi\ \sin^2\eta}}\left(\sqrt{\frac{k+1}{k-1}}\ e^{-\xi}\ \sin\eta \right.$$

$$\left. + \sqrt{k^2-1}\ \cosh\xi\ \sin\eta\right) \tag{61}$$

Equations 49, 59 and 61 determine the potential solution for flow over an elliptical cylinder.

128

APPENDIX B

UNIFORM POTENTIAL FLOW PAST AN ELLIPTICAL

CYLINDER WITH FIXED VORTICES

Consider a circular vortex of radius A rotating in a stationary, inviscid, irrotational, incompressible fluid. Locating circles concentric with the vortex of radius $r' < A$ and $r'' > A$, Stokes circulation theorem (23) can be applied to obtain the velocity of the fluid on these circles,

$$q = \frac{1}{2} \frac{\omega A^2}{r''} \qquad r'' > A$$

$$q = \frac{1}{2} r\omega \qquad r' < A$$

where ω is the vorticity of the fluid inside of the vortex. Therefore, the existence of a vortex in an inviscid fluid induces a velocity field in the region around it with the magnitude of the induced velocity inversely proportional to the radial distance from the center of the vortex and directed perpendicularly to this radius. The fluid within the vortex rotates as a rigid body with a velocity proportional to the radial distance. It is important to note that the vortex cannot induce motion at its center, implying that a circular vortex in an undisturbed fluid will remain fixed at its initial position.

Considering a circular vortex centered at the origin

in the complex Z plane, the velocity field induced to a stationary fluid is given by

$$\vec{q} = |\vec{q}|e^{i(\theta+\pi/2)}$$

which expressed in terms of a complex velocity is

$$v = -\frac{dw}{dZ} = U - iV = |\vec{q}|e^{-i(\theta+\pi/2)} = \frac{1}{2}\frac{A^2\omega^2}{r}e^{i(\theta+\pi/2)}$$

Integrating this equation results in the complex potential, w, for flow about a fixed vortex.

$$w(Z) = \frac{1}{2}i\omega A^2 \ln Z$$

Centering the vortex at an arbitrary point z_o and defining a circulation strength $\kappa = \frac{1}{2}A^2\omega$, being positive in the counter-clockwise direction, the complex potential becomes

$$w(Z) = i\kappa \ln(Z - Z_o) \tag{62}$$

The rotational core of the vortex can be reduced to a singularity at the center by considering the concept of a vortex filament. Taking the limit as the radius of the vortex decreases to zero and the vorticity approaches infinity, such that the product $A \cdot \omega$ remains constant, the circular vortex degenerates to a point with the external flow field still given by Equation 62.

Consider a pair of vortex filaments of equal strengths but opposite rotations as shown in Figure A4, located at
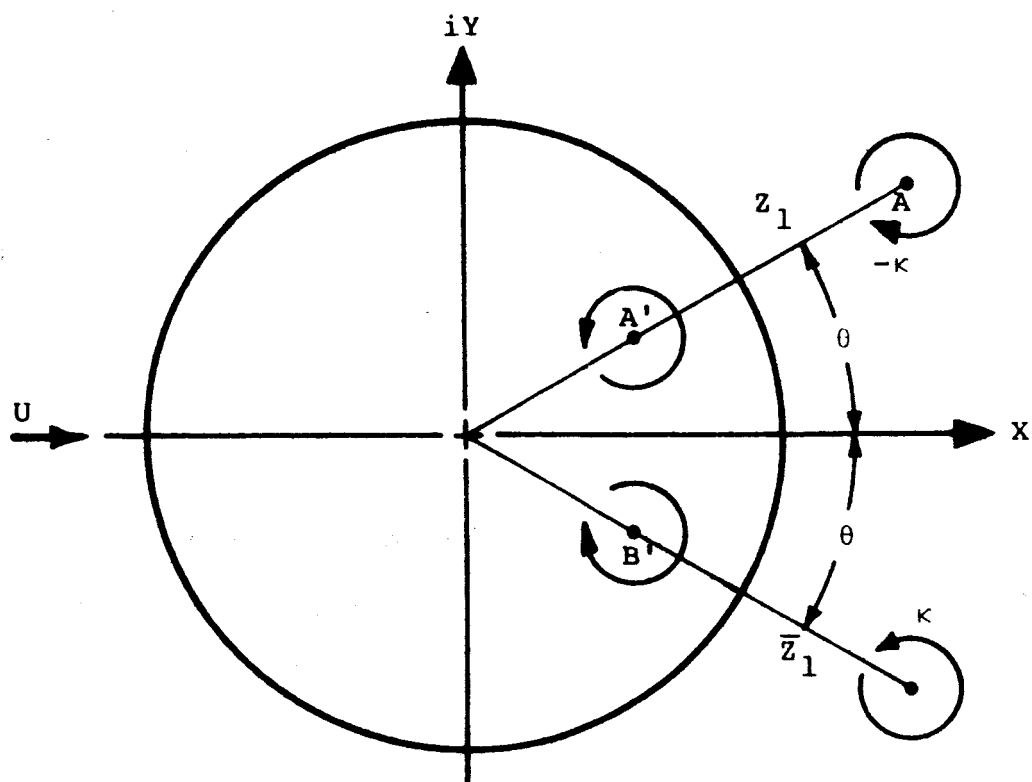
130

Figure A4. Stationary inviscid vortices behind a circular cylinder.

conjugate points Z_1 and $\bar{Z}_1$ outside a circular cylinder $|Z| = A$. The complex potential of the vortex combination in the absence of the cylinder is given by Equation 61 as the sum of the potentials due to each vortex rotating alone in an infinite, undisturbed fluid. If the motion of the fluid is due solely to the vortices, the circle theorem gives the potential for flow around the cylinder as

$$w(Z) = -i\kappa\ell n\left(\frac{Z - Z_1}{Z - \bar{Z}_1}\right) + i\kappa\ell n\left(\frac{\frac{A^2}{Z} - \bar{Z}_1}{\frac{A^2}{Z} - Z_1}\right) \qquad (63)$$

Expanding the logarithms of Equation 63, the potential becomes

$$w(Z) = i\kappa\ell n(Z - Z_1) + i\kappa\ell n(Z - \bar{Z}_1) + i\kappa\ell n\left(\frac{A^2}{Z} - \bar{Z}_1\right)$$

$$-i\kappa\ell n\left(\frac{A^2}{Z} - Z_1\right)$$

or

$$w(Z) = -i\kappa\ell n(Z - Z_1) + i\kappa\ell n(Z - \bar{Z}_1) - i\kappa\ell n\left(Z - \frac{A^2}{\bar{Z}_1}\right)$$

$$+ i\kappa\ell n\left(Z - \frac{A^2}{Z_1}\right) - i\kappa\ell n\left(\frac{\bar{Z}_1}{Z_1}\right) \qquad (64)$$

The terms of the above equation represent, respectively, the potential of the vortex filaments at A and B, the images of these vortices at the inverse points A' and B' inside the

132

cylinder, plus a constant term.

Since a vortex cannot induce velocity at its center, the motion of a vortex system is a function of the combined velocity fields of all sources, sinks, and other vortices in a fluid region. From Equation 63, the complex velocity of the vortex at A can be calculated by considering all contributions to the flow except from the vortex. Therefore, eliminating the first term of Equation 64 the complex potential of the vortex at A is given by

$$w_A(Z) = i\kappa\ln\left[\frac{(Z - \bar{Z}_1)\left(Z - \frac{A^2}{\bar{Z}_1}\right)}{\left(Z - \frac{A^2}{\bar{Z}_1}\right)}\right] \tag{65}$$

Adding a uniform velocity field, U, directed in the positive X-direction, to this flow field around the cylinder, the complex potential at A becomes

$$w_A(Z) = -U\left(Z + \frac{A^2}{Z}\right) + i\kappa\ln\left[\frac{(Z - \bar{Z}_1)\left(Z - \frac{A^2}{\bar{Z}_1}\right)}{\left(Z - \frac{A^2}{\bar{Z}_1}\right)}\right] \tag{66}$$

The complex velocity at A is then obtained from the above relation by differentiating with respect to Z and setting $Z = Z_1$.

To fix this vortex at point A, the velocity, v_A, must vanish. Applying these conditions to Equation 66 and

133

expanding

$$U\left(1 - \frac{A^2}{Z_1}\right) = i\kappa \frac{(Z_1 - A^2)(Z_1\overline{Z}_1 - A^2) + A^2(Z_1 - \overline{Z}_1)}{(Z_1\overline{Z}_1 - A^2)(Z_1 - \overline{Z}_1)(Z_1^2 - A)}$$

dividing both sides of this equation by the conjugate of Equation 65 and simplifying, the condition for a fixed vortex at A becomes

$$(Z_1\overline{Z}_1 - A^2)^2 + Z_1\overline{Z}_1(Z_1 - \overline{Z}_1)^2 = 0 \qquad (67)$$

Expressing Equation 67 in polar form, $Z_1 = re^{i\theta}$ it becomes

$$(r^2 - A^2)^2 + r^2(re^{i\theta} - re^{-i\theta})^2 = 0$$

$$(r^2 - A^2)^2 = -4r^4 \sinh^2(i\theta) = -4i^2r^4 \sin^2\theta$$

$$r^2 - A^2 = 2r^2 \sin\theta$$

$$r - \frac{A^2}{r} = 2r \sin\theta \qquad (68)$$

Referring to Figure A4, page 117, Equation 68 yields the following condition for a stationary vortex at A:

$$\overline{AA'} = \overline{AB} \qquad (69)$$

In addition, Equation 68 relates the strength of the vortex at A to its position by

$$\kappa_A = \frac{U(r^2 - A^2)^2(r^2 + A^2)}{r^5} \qquad (70)$$

134

Since the flow is symmetric to the X-axis, similar conditions apply to the vortex filament at B.

The complex potential for flow of the uniform stream U over a circular cylinder with fixed vortices behind is obtained by adding the term $-i\kappa \ln(Z - Z_1)$ for the vortex at A to Equation 66, resulting in

$$w(Z) = -U\left(Z + \frac{A^2}{Z}\right) + i\kappa \ln(Z - \overline{Z}_1) + i\kappa \ln\left(Z - \frac{A^2}{\overline{Z}_1}\right)$$

$$- i\kappa \ln(Z - Z_1) - i\kappa \ln\left(Z - \frac{A^2}{Z_1}\right) \tag{71}$$

To include vortices in the flow field upstream of the circular cylinder at positions Z_2 and $\overline{Z}_2$, similar logarithmic terms must be added to the above equation yielding a complex potential of the following form:

$$w(Z) = -U\left(Z + \frac{A^2}{Z}\right) + i\kappa\left[\ln(Z - \overline{Z}_1) + \ln\left(Z - \frac{A^2}{\overline{Z}_1}\right)\right.$$

$$- \ln(Z - Z_1) - \ln\left(Z - \frac{A^2}{Z_1}\right) + \ln(Z - \overline{Z}_2)$$

$$\left. + \ln\left(Z - \frac{A^2}{\overline{Z}_2}\right) - \ln(Z - Z_2) - \ln\left(Z - \frac{A^2}{\overline{Z}_2}\right)\right] \tag{71}$$

Introducing the complex coordinates, $Z = X + iY$, into the above equation and separating the real and imaginary parts results in the following relation for the nondimensional stream function:

$$\psi = \frac{\psi}{UA} = Y - \frac{Y}{X^2 + Y^2} + \frac{\kappa}{2}\left\{-\ell n[(X - X_1)^2 + (Y - Y_1)^2]\right.$$

$$+ \ell n\left[\left(\frac{X - X_1}{X_1^2 + Y_1^2}\right)^2 + \left(Y - \frac{Y_1}{X_1^2 + Y_1^2}\right)^2\right]$$

$$- \ell n[(X - X_1)^2 + (Y - Y_1)^2] - \ell n\left[\left(X + \frac{X_1}{X_1^2 + Y_1^2}\right)^2\right.$$

$$+ \left.\left(Y + \frac{Y_1}{X_1^2 + Y_1^2}\right)^2\right] + \ell n[(X - X_2)^2 + (Y + Y_2)^2]$$

$$- \ell n\left[\left(X - \frac{X_2}{X_2^2 + Y_2^2}\right)^2 + \left(Y - \frac{Y_2}{X_2^2 + Y_2^2}\right)^2\right]$$

$$+ \ell n[(X - X_2)^2 + (Y - Y_2)^2]$$

$$+ \left.\ell n\left[\left(X - \frac{X_2}{X_2^2 + Y_2^2}\right)^2 + \left(Y + \frac{Y_2}{X_2^2 + Y_2^2}\right)^2\right]\right\} \qquad (72)$$

Differentiating the stream function with respect to the X- and Y-directions provides the components of the velocity vector,

$$u = -\frac{\partial \psi}{\partial Y} \qquad (73)$$

$$v = \frac{\partial \psi}{\partial X} \qquad (74)$$

where

$$|\vec{U}| = \sqrt{u^2 + v^2}$$

These equations together with Equation 72 define the invis-
cid streamlines and velocities over the circular cylinder
with stationary vortices upstream and downstream in a
uniform flow field.

Applying the Joukowski transformation converts this
region of the flow outside the circular cylinder in the Z
plane to a region outside an elliptical cylinder in the z
plane,

$$z = Z + \frac{c^2}{4Z}$$

where

$$c^2 = a^2 - b^2$$

In terms of the coordinate direction,

$$x + iy = X + iY + \frac{a^2 - b^2}{4(X + iY)}$$

Nondimensionalizing by the length of the minor axis $2 \cdot b$
and defining an ellipse aspect ratio, $k = a/b$,

$$x = X + \frac{(k^2 - 1) \cdot X}{X^2 + Y^2} \tag{75}$$

$$y = Y - \frac{(k^2 - 1) \cdot Y}{X^2 + Y^2} \tag{76}$$

Applying the transformation given by Equations 75 and
76 to the expression for the stream function of Equation 72

137

and the equations for the potential velocity of Equations 73 and 74 gives the solution for inviscid flow over an elliptical cylinder with fixed vortices.

APPENDIX C

THE CONSERVATION OF EDDY VISCOSITY

A majority of the methods used for incorporating the effect of turbulence on the boundary layer have basically relied on the mixing length theory as an empirical relationship between the turbulent viscosity and the mean flow parameters. A more recent concept, proposed by Nee and Kovasznay in (21), is based to a greater extent on the physical mechanisms involved with turbulent interaction by considering the eddy viscosity as a property of the flow which is conserved during turbulent motion within the boundary layer.

In describing the distribution of the turbulent shear through the boundary layer, the momentum equation relates the Reynolds' stress to the processes associated with convection, diffusion, production and dissipation. Assuming that the eddy viscosity is conserved during the exchanges of momentum involved with these processes, the following transport equation has been proposed

$$\bar{u}\,\frac{\partial \bar{n}}{\partial \bar{x}} + \bar{w}\,\frac{\partial \bar{n}}{\partial \bar{z}} = \frac{\partial}{\partial \bar{z}}\left(\bar{n}\,\frac{\partial \bar{n}}{\partial \bar{z}}\right) + a(\bar{n}-\bar{\nu})\left|\frac{\partial \bar{u}}{\partial \bar{z}}\right| - b\,\frac{\bar{n}(\bar{n}-\bar{\nu})}{\bar{\ell}'^{2}}$$

$$- c\,\frac{\bar{n}(\bar{n}-\bar{\nu})}{\bar{U}_{\infty}^{2}}\,\frac{d\bar{U}_{\infty}}{d\bar{x}}\cdot\frac{d\bar{u}}{\partial \bar{z}} \tag{77}$$

where the bar indicates dimensional quantities. The

variable $\bar{n}$ is the sum of the molecular and eddy viscosities; a, b and c are empirically determined but universal constants; and $\bar{\ell}'$ is a length scale associated with the dissipation of turbulence which is equivalent to the normal distance from a solid boundary for turbulent shear flows.

Nondimensionalizing this equation results in the following nonlinear, partial differential equation for the eddy viscosity:

$$u \frac{\partial \varepsilon}{\partial x} + w \frac{\partial \varepsilon}{\partial z} = \frac{1}{Re}\left[(\varepsilon + 1)\frac{\partial^2 \varepsilon}{\partial z^2} + \left(\frac{\partial \varepsilon}{\partial z}\right)^2 \right] + a\varepsilon \left| \frac{\partial u}{\partial z} \right|$$

$$- \frac{b}{Re} \frac{\varepsilon(\varepsilon + 1)}{z^2} - \frac{c}{Re} \frac{\varepsilon(\varepsilon + 1)}{U_e^2} \frac{dU_e}{dx}\left| \frac{\partial u}{\partial z} \right| \quad (78)$$

The boundary conditions which apply to this equation will, of course, vary with the flow situation considered, but for the normal boundary layer problem with an inviscid, turbulence-free external flow, the following conditions apply at the boundaries:

$$\varepsilon(x,0) = 0$$

$$\lim_{y \to \infty} \varepsilon(x,z) = 0$$

The solution of this equation also requires an initial condition on the eddy viscosity. One possibility is to apply some type of mixing length model to an initial velocity profile.

Numerical solution. Since the eddy conservation

140

equation and the momentum equation are coupled through the convection and the dissipation terms, respectively, the two solutions must be obtained simultaneously through an iterative technique. Applying an implicit finite difference method similar to the solution of the boundary layer equation, results in a system of algebraic equations which can be solved by the inversion of the tridiagonal coefficient matrix.

The conservation equation is linearized by the velocity profiles calculated along the previous x-station. Applying the above numerical solution, the eddy profile is used to re-enter the momentum equation and solve for the velocity, iterating on this procedure until the solutions for the velocity and eddy viscosity converge.

An attempt has been made to incorporate the concept of conservation of eddy viscosity into the turbulent boundary layer model, but problems in obtaining a satisfactory initial eddy profile leading to convergence of the solution and insufficient time to investigate the possibilities of this method, have prevented any meaningful results or evaluations of this theory.